Study of x_{T} Scaling in Proton-Proton Collisions Measured by the ALICE Experiment

Esko Heikki Oskari Pohjoisaho

UNIVERSITY OF JYVÄSKYLÄ

Master's thesis

University of Jyväskylä

Department of Physics

Supervisor: Jan Rak

November 2012

Abstract

In this Master's Thesis an analysis of proton proton data measured by the ALICE (A Large Ion Collider Experiment) Collaboration [1] at center-of-mass energies 7 TeV and 2.76 TeV is presented. The ALICE detector is located at the LHC (Large Hadron Collider) at CERN, Switzerland. The goal of this thesis was to study whether the isolation requirement can increase the sensitivity of the x_{T} spectra ($x_{\mathrm{T}} = 2p_{\mathrm{T}}/\sqrt{s}$) to higher-twist (HT) processes. In HT processes the outgoing hadron is produced directly in the hard subprocess, rather than in the fragmentation process described by the leading-twist (LT) processes in the perturbative QCD picture [2]. Higher-twist processes are mainly low p_{T} phenomena, causing steeper fall-off of the cross section distributions with respect to x_{T}.

It has been suggested that the production of isolated particles would be enhanced by the HT processes [3]. An x_{T} analysis [4] was done for isolated particles to see whether a significant increase of the extracted exponent n can be observed. This also raised motivation to study the systematic effects caused by the isolation criteria such as the isolation cone size and background p_{T} cut in the cone. The results of the ALICE data analysis were compared to PYTHIA Monte Carlo (MC) event generator. It was observed that the isolation increased the n in both real data and PYTHIA.

A simple toy Monte Carlo fragmentation model was made to study the kinematic effects resulting from the isolation cut. The increase of n was observed also in the toy model, indicating a kinematic bias related to the isolation criteria. It was demonstrated that isolated particles had larger values of z, the momentum ratio of the hadron to its parent parton. The toy MC model suggested that the increase of n is due to the combination of the steepness of the parton momentum distribution and the magnitude of the mean z.

In order to study the higher-twist phenomena in real data, one would need to separate the trivial increase of n caused by the systematic effects from the HT signal. To disentangle the two, the magnitude of the Δn resulting from the isolation itself should be calculated with a more realistic model like the NLO pQCD.

Tiivistelmä

Tässä pro gradu-työssä esitellään data-analyysi CERNin ALICE-kollaboraation [1] mittaamasta protoni–protoni-datasta törmäysenergioilla $\sqrt{s}$ =7 TeV ja 2.76 TeV. Työn tärkein päämäärä oli tutkia, onko ns. "higher-twist" (HT)-prosessien läsnäolo korostunut datassa, joka on mitattu ainoastaan eristäytyneistä hadroneista inklusiivisten varattujen hadronien sijaan.

Häiriöteoreettisessa QCD-kuvassa hadronit muodostuvat, kun törmäyksestä ulostulevat partonit hadronisoituvat fragmentaation kautta. Hadronituoton todennäköisyyksiä voidaan laskea ns. kollineaarifaktorisaatiolla, jonka kuvaamia prosesseja kutsutaan "leading-twist" (LT)-prosesseiksi [2]. HT-prosesseissa törmäyksestä ulostuleva hadroni muodostuu kuitenkin suoraan kovassa kvarkkien tai gluonien vuorovaikutuksessa, jolloin on perusteltua odottaa että hadroninen aktiviteetti hiukkasen ympärillä on vähäisempää kuin LT-tapauksessa [3]. Koska LT-prosessit eivät yksistään riitä selittämään kokeellisesti mitattuja tuloksia, on HT-prosessien osuuden kokeellinen mittaaminen ja teoreettinen kuvaaminen eräs hiukkasfysiikan nykyisistä tutkimuskohteista.

Se, onko hiukkanen eristäytynyt vai ei, voidaan selvittää kuvittelemalla tutkittavan hiukkasen ympärille kartio ja laskemalla yhteen kartiossa olevien hiukkasten liikemäärät. Mikäli tämä summa ylittää ennalta asetetun eristämisrajan, voidaan hiukkanen julistaa eristäytyneeksi. Eristämisen odotetaan vaimentavan LT-prosesseista peräisin olevia hiukkasia, jolloin lopputuloksena HT-prosessien osuus olisi korostunut.

Higher-twist-prosessit ilmenevät pienen poikittaisliikemäärä p_{T}:n alueella, joten niiden läsnäolon odotetaan aiheuttavan vaikutusalaspektrien jyrkkenemistä, ja sen seurauksena spektrien muodolle suuremman potenssilain eksponentin n arvoja. Tässä työssä mitattiin n-eksponentti $x_{\mathrm{T}} = 2p_{\mathrm{T}}/\sqrt{s}$:n funktiona sekä ALICE-datalle että PYTHIA-törmäysgeneraattorin Monte Carlo-simuloidulle datalle. Molemmissa tapauksissa havaittiin että n oli suurempi eristäytyneillä hadroneilla kuin inklusiivisilla hadroneilla, kuten oli ennustettu.

Jotta saataisiin selville johtuiko eksponentin kasvu HT-prosesseista vai jostain muusta eristämiseen liittyneestä systemaattisesta ilmiöstä, analyysi toistettiin vielä yksinkertaiselle "lelumallille" hadronijakaumasta. Tässä mallissa oletettiin partonille liikemäärä

potenssilakijakaumasta, josta luotiin hadronijakauma käyttämällä eksponenttimuotoista fragmentaatiofunktiota. Tällä haluttiin simuloida mahdollisimman yksinkertaista hadronijakaumaa, joka kuitenkin olisi mahdollisimman lähellä häiriöteoreettista QCD-kuvaa. Etuna oli se, että mallin kaikki parametrit tunnettiin, ja että voitiin varmistua, ettei HT-prosesseja ollut läsnä mallissa. Eksponentti n kasvoi myös tässä mallissa, oleellisesti saman verran kuin oikean datan ja PYTHIA:n tapauksessakin.

Havaittiin, että eristäytyneet hiukkaset poimivat fragmentaatiofunktiosta systemaattisesti suurempia z-arvoja kuin kaikki hiukkaset keskimäärin. Muuttuja z kuvaa hadronin liikemäärän suhdetta siihen partoniin, josta kyseinen hadroni muodostui. Lisäksi todettiin, että eksponentin kasvu riippui myös partonijakauman muodosta, joka riippui mallinnettavasta törmäysenergiasta. Eksponentin n laskemiseen tarvitaan kahdella eri törmäysenergialla tuotettuja jakaumia, mutta eri energioista seurasi kuitenkin erilainen todennäköisyys tuottaa eristäytynyt hadroni, ja näiden todennäköisyyksien ero osaltaan aiheutti n:n kasvamista.

HT-prosesseja ei ole täysimääräisesti ohjelmoitu PYTHIA-simulaatioon, ja siitä huolimatta joillain x_{T}-alueilla eristäytyneiden hadronien n-eksponentti oli jopa suurempi PYTHIA-simulaatiossa kuin ALICE-datassa. Sekä tämän havainnon että yksinkertaisen lelumallin tuloksien nojalla työn päätulos on, että HT-prosesseja tutkiessa tulee ottaa huomioon eksponentin n kasvu, joka johtuu pelkästä eristämisehdosta ilman HT-prosessejakin. Tämän kinematiikan muutoksen aiheuttaman eksponentin kasvun suuruus tulisi laskea tarkemmin esimerkiksi NLO pQCD-teorian avulla, jotta voitaisiin erottaa varsinaisten HT-prosessien osuus tuloksissa.

Contents

1 Introduction

1.1 Quantum chromodynamics, a theory of the strong interaction

Quantum Chromodynamics (QCD) has been a well established theory of the strong interaction among quarks and gluons since the 1970s [5]. The agreement between next-to-leading-order calculations from the QCD and the measured experimental cross sections spans many orders of magnitude [6].

The way to the discovery of quarks as constituents of the proton began with the emergence of the parton model (to be discussed later) and with the electon-proton deep inelastic scattering (DIS) measurements done at the Stanford Linear Accelerator (SLAC) in 1969 [7]. If the proton had an internal structure, then the cross section for DIS should depend on structure functions describing the interaction between the scattered electron and the constituents. The measured structure functions agreed with the scaling laws predicted by Bjorken in [8], suggesting that the proton consists of pointlike particles that have no internal structure, and from which the electron scattered. From a theoretical perspective, the existence of such point-like constituents was also the key property of the parton model proposed by Feynman in [9], which succesfully described the experimental DIS results.

The cross section for hadron production at low transverse momentum p_{T} was known to decrease according to the Cocconi formula $e^{-6p_{\mathrm{T}}}$ [10, 11]. However, it was found out at SLAC and at the CERN-Columbia-Oxford-Rockefeller (CCOR) collaboration at CERN-ISR ([12], [13] and [14]) that at high p_{T} the exponential formula was violated, and the cross section followed a power-law form $1/p_{\mathrm{T}}^{n}$, which was the discovery of hard processes [15]. The exponential low-p_{T} part represents the particle production from soft processes, nowadays understood as to originate from the fragmentation of beam remnants, multiple parton interactions and initial- and final-state radiation (ISR and FSR) [16]. The power-law part comes from the hard scattering and the observed high-p_{T} hadrons are fragments of a jet. The violation of the Cocconi formula at high-p_{T} was interpreted as a strong interaction of the constituent partons, which was another key evidence of the internal structure of

hadrons [15, 17]. The cross section for inclusive high-p_{T} charged hadron production from proton-proton collisions at different experiments is shown on the left side of Fig. 1 from [15], and on the right side for pion production at PHENIX with an exponential fit to the low-p_{T} part from [18], to help differentiate between the soft and hard parts of the spectrum. The center-of-mass energy $\sqrt{s}$ is indicated in the legends in units of GeV.

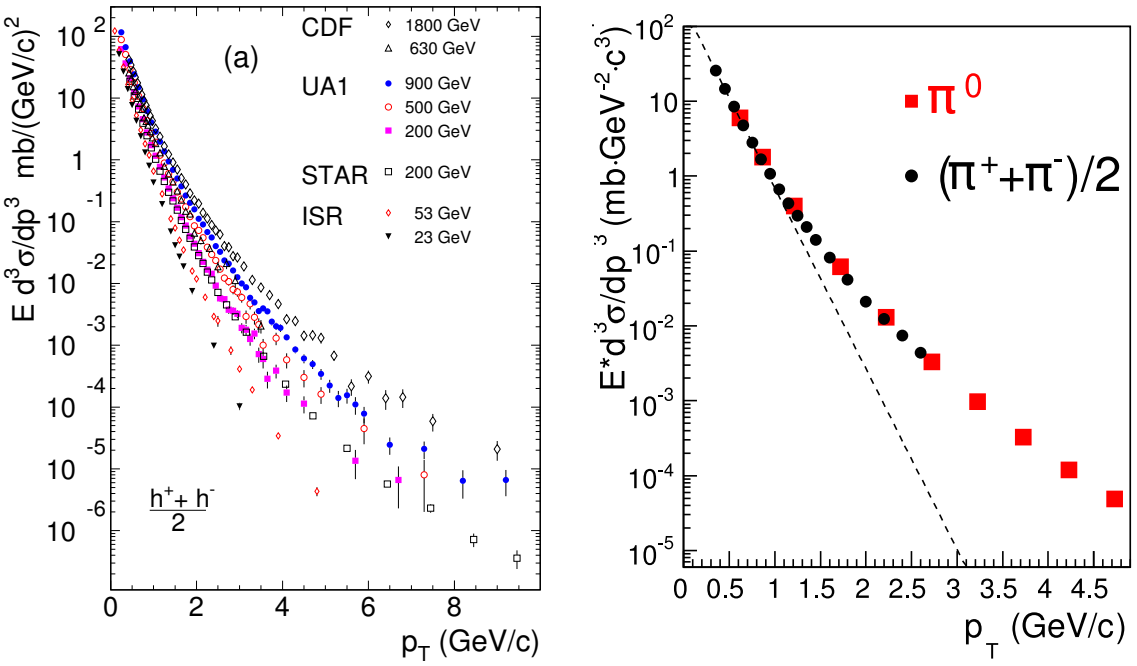

(a) (b)

Figure 1: Left: Invariant cross section vs. p_{T} for charged hadron production in different experiments, [15]. Right: Invariant cross section for pion production in pp collisions at the PHENIX experiment, with an exponential fit to the low-p_{T} part [18].

At approximately the same time with the parton model, the quark model was discovered [5]. By the late 1960s, several dozen of hadrons had been observed, and some unifying theoretical framework was needed to interpret this multitude of hadron states. It was proposed by Murray Gell-Mann and George Zweig (independently of each other, [19] and [20]) at CERN in 1964, that the new particles were were bound states of three "flavors" of fundamental spin-1/2 particles obeying SU(3) symmetry. Gell-Mann called these particles *quarks*, cited from the quotation "Three quarks for Muster Mark" in a book Finnegans Wake by James

Joyce [5].

Some concern regarding the quark model was raised by the discoveries of new particles, e.g. the Δ^{++} baryon [21]. The problem was that it consisted of three up quarks with parallel spins. Therefore, the wave function would not change if any of the two quarks were interchanged, which would violate the Pauli exclusion principle of fermions, the half-integer spin particles. A similar problem occurred with a baryon called Ω^-, which is a bound state of three s quarks with spins aligned so that the net spin is $3/2$, as was observed at the Brookhaven National Laboratory in 1964 [22].

Later in the same year, Oscar W. Greenberg proposed a new quantum number related to quarks to overcome the problem with Pauli principle [23]. This quantum number was later called the "color charge" by John Bardeen, Harald Fritsch and Gell-Mann in [24]. The color charge has analogies to the electric charge found in the quantum electrodynamics (QED), but a quark can take one of three colors and an antiquark one of three anticolors. The gluon carries both color and anticolor, making in total eight gluons with independent colored combinations in the QCD. In 1972, the color was interpreted as a gauge group, resulting in a gauge theory similar to QED. With this step, the theory got the name *quantum chromodynamics*, and an octet of gluons was introduced as gauge bosons [21].

On the way to the current Standard Model, the number of generations of elementary fermions was not known. In Figure 2 the ratio $R = \sigma(e^+e^- \to hadrons)/\sigma(e^+e^- \to \mu^+\mu^-)$ of hadronic cross section to muon cross section in electron-positron collisions with respect to the center-of-mass energy $\sqrt{s}$ is shown [25]. The first example is the step after the resoncance of the J/ψ meson, when $\sqrt{s} > 3$ GeV. This increase in cross section comes from the fact that the center-of-mass energy becomes sufficient to produce a charm quark. The next step comes after the Υ family at 10 GeV, when it becomes possible to produce a bottom quark [26].

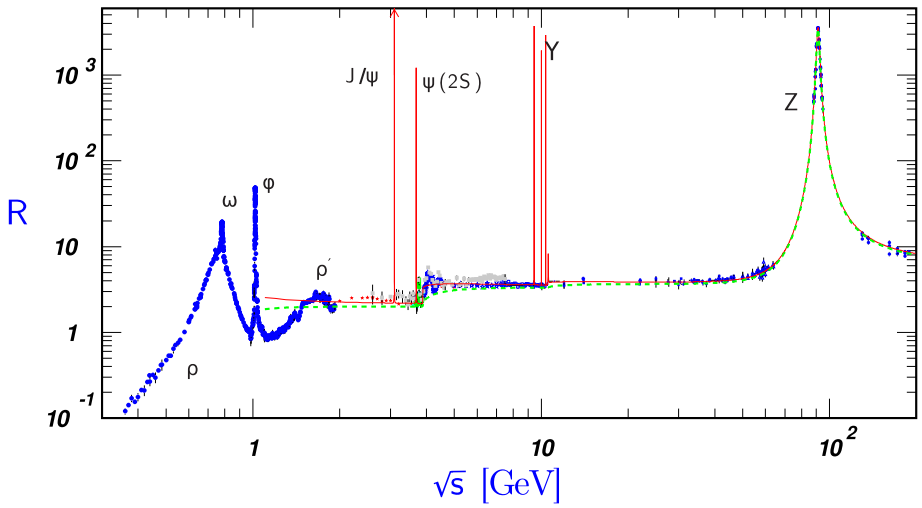

Figure 2: World data for ratio $R = \sigma(e^+e^- \to hadrons)/\sigma(e^+e^- \to \mu^+\mu^-)$ vs. $\sqrt{s}$. Figure from [25].

The distinct features of QCD can be seen in the Lagrangian density, which describes the dynamics of a system of quarks and gluons. For QCD, it can be written as ([27])

$$\mathcal{L}_{\text{QCD}} = \bar{\psi}(i\partial^\mu\gamma_\mu - m)\psi - g_s\bar{\psi}\gamma^\mu T_a\psi A^a_\mu - \tfrac{1}{4}F^{\mu\nu}_a F^a_{\mu\nu}, \tag{1}$$

where the γ are the Dirac γ-matrices, the ψ are the quark-field spinors and the A^a_μ correspond to the gluon fields with eight color indices a. The repeated indices are summed over. The mass of the quark is given by m in (1), and g_s is the QCD coupling constant. The SU(3) generator matrices T^a fulfill the commutation relation $[T^a, T^b] = if_{abc}T^c$, where the f_{abc} are the structure constants of the SU(3) color group. Because the generator matrices do not commute as in the QED, the theory is called "non-abelian", which has remarkable consequences for QCD. From the field tensor (1)

$$F^{\mu\nu}_a = \partial^\mu A^\nu_a - \partial^\nu A^\mu_a - g_s f_{abc}A^\mu_b A^\nu_c, \tag{2}$$

one can see that the last term describes the gluon-gluon interaction which makes the theory very different from, for example, the QED.

There still exist some unanswered aspects of QCD that could be studied by proton-proton collisions. For example, one of these is the origin of the spin of the proton. It was found first in 1988 by the European Muon Collaboration (EMC), that the spin of the constituent quarks comprised only one third of the total proton spin [28]. The question about the missing two thirds component of the proton spin has been called "the proton spin crisis". There are calculations suggesting that at least part of the problem could be explained by measuring the gluon spin, or the orbital angular momentum of quarks and gluons. To verify this explanation, one would need a measurement of the Generalized Parton Distributions, for which a specific machine would be needed, as it is not a part of the LHC program [28].

Another issue related to the QCD is the unitarity problem [29]. At the center-of-mass energies of the LHC and at momentum transfers of a few GeV/c, the calculated QCD partonic cross section becomes larger than the calculated total hadronic cross section. This is, obviously, in contradiction with the reality. This has been thought to be indicate that Multiple Partonic Interactions (MPI) occur in the regime [30]. In MPI several pairs of partons from the incoming hadrons collide with each other, instead of just one, thus increasing the partonic cross section. In Monte Carlo event generators, the MPI explain many features of the data.

Another possible rectification of the unitarity problem may come from the QCD coherence. In the limit of $x \to 0$ the number density of gluons starts to saturate. This will limit the partonic cross section, and one such model is called the Color Glass Condensate [31].

1.2 Asymptotic freedom and color confinement

In the QCD, the gluons interact also with themselves (self-coupling) in addition to quarks, and this is because of the non-abelian structure of the theory. As a consequence, the QCD possesses two remarkable features not found in the QED - asymptotic freedom and color confinement.

Asymptotic freedom was discovered by David Gross, Frank Wilczek and David Politzer in 1973 (Nobel prize awarded in 2004) [32, 33]. The term is used to describe the weakening, or "running", of the effective quark–gluon and gluon–gluon coupling strength $\alpha_s = \frac{g_s^2}{4\pi}$ at short

distances or, equivalently, large momentum transfer. This feature allows the application of perturbative QCD (pQCD) techniques to the problem of obtaining predictions for processes that are dominated by hard processes involving large momentum transfers. In contrast, the low-momentum-transfer processes are called "soft", and cannot be resolved with perturbative methods [5].

Contrary to asymptotic freedom, in the QED there is an effect called "screening", meaning that the effective electric charge decreases as the distance between test particles increases. This is explained by the presence of virtual charged particle-antiparticle dipole fluctuations in the vacuum, which are polarized by the electric field. The dipoles align to oppose the field, effectively acting as an insulator. As the distance increases, the test charge interacts more and more with the vacuum dipoles, and it "sees" less and less of the original charge [5].

In the QCD, the vacuum also contains dipoles of quark-antiquark pairs that produce screening similarily as in the QED. However, the neutral photons in the abelian QED do not self-interact, but in the non-abelian QCD the self-coupling and colored virtual gluons play a significant role in the vacuum, causing antiscreening of the color charge [34]. The spin-1 gluons behave in the vacuum as permanent magnetic dipoles in a medium, aligning themselves parallel to an applied external color field, which causes antiscreening by reinforcing the color field. The gluon-induced antiscreening eventually overcomes the screening effect caused by particle-antiparticle dipoles, because the number of gluons is larger than the number of quarks. The asymptotic freedom in the end is the net effect of these two opposing phenomena [35].

Asymptotic freedom led also to predictions of strongly coupled, deconfined and thermally equilibrated QCD phase of matter called "the quark gluon plasma" (QGP), comprised of quarks and gluons [36]. Lattice QCD calculations predict that the critical temperature for the phase transition from hadronic matter to QGP occurs at around $T \approx 170\,\mathrm{MeV} \approx 10^{12}$ K, which corresponds to energy density $\epsilon \approx 1$ GeV/fm^3 [37]. These kind of conditions are believed to have existed in the very early universe, and can now be created in heavy ion (HI) collisions. There is a lot of experimental evidence for the presence of QGP phase in HI

collisions at RHIC and the LHC. However, it is believed that this QGP is rather a strongly coupled "ideal liquid" [37, 38] than asymptotically free gas of quarks and gluons.

The second distinct feature of the QCD is color confinement, meaning that the observed states must have zero color charges, implying that one cannot observe isolated gluons or quarks that have nonzero values of the color charge [5]. It is often explained that when the non-perturbative "gluon string" or the "flux tube" (a strong color field between the quarks) is streched enough by pulling the quarks apart, it breaks producing new $q\bar{q}$ pairs to form hadrons subsequently. But if one considers, for example, the production of a quark q and an antiquark $\bar{q}$ in the hard annihilation process $e^+e^- \to q\bar{q}$, the high momentum of the quarks, with the asymptotic freedom, allows time for the quarks to fly freely away from each other. The exact mechanism of how the two colored quarks color-neutralize each other at long distance is not known [39].

1.3 Hadronic cross section in perturbative QCD (pQCD)

An important comparison between experimental data and theory in this thesis is done for hadronic cross sections. In the theoretical pQCD picture, the hadronic cross section calculation is divided into short distance and long distance phenomena. QCD can be used to calculate cross section for hard processes between two partons, where the momentum transfer is large. This partonic cross section is used when one wants to calculate perturbatively the cross section of the hard scattering of hadrons in e.g. a proton proton collision. To move from partonic to hadronic level, one needs (long distance) information about the momentum distribution of partons inside the parent hadron, which is given by parton distribution functions (PDF). For example, a PDF $G_{a/A}(x)$ gives the propability of obtaining parton a from a hadron A with a momentum fraction between x and $x + dx$.

Up to now the PDFs cannot be calculated from first principles in QCD, and therefore experimental data is needed to obtain the distributions. Collaborations such as CTEQ evaluate the PDFs by carrying out global fits to a collection of experimental data from many present and past experiments. Since the momentum scale Q^2 differs between experiments,

so-called DGLAP evolution equations have to be used to describe the evolution of the momentum transfer scale Q^2. When the experimental results and DGLAP equation are combined , the result is a parton distribution function that can be used by different scales and is universal, i.e same for any hard process.

Due to the color confinement property of the QCD, the outgoing final-state color-charged partons form hadrons that are finally observed. A fragmentation function (FF) $D_{C/c}(z)$ represents the probability for a parton c to end up in a hadron C carrying a certain fraction $[z\ ,\ z+dz]$ of the parton's energy. Similarly to PDFs, FFs represent the long distance part of the calculation and cannot be calculated from QCD perturbatively, and thus have to be estimated based on experimental data. A schematic pQCD model picture of a hard scattering reaction with PDFs, hard subprocess and FFs is shown in Fig. 3.

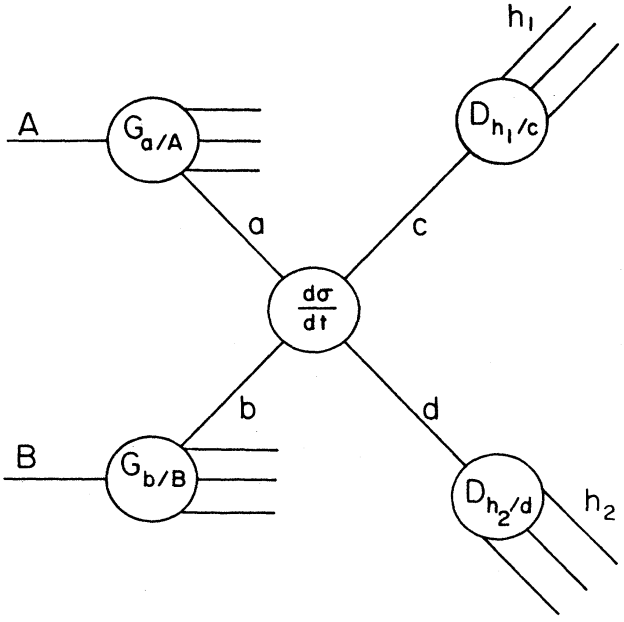

Figure 3: Perturbative QCD model description of a hard scattering process. The reaction is factorized into parton distribution functions G, a hard subprocess $d\sigma/dt$ and fragmentation functions D. Partons a and b from the incoming hadrons A and B interact through a hard subprocess, and the outgoing partons c and d fragment into hadrons h_1 and h_2.

In the pQCD picture the cross section for a hard scattering process between two hadrons is built up by a summation over all possible constituent scatterings weighted by the appropriate

PDFs and FFs with the hard subprocess being described in lowest order by two body scattering. For a process $A + B \rightarrow C + X$ shown in the Fig. 3, the invariant cross section is [2]

$$E_C \frac{\mathrm{d}^3\sigma}{\mathrm{d}p_C^3}(AB \rightarrow C+X) = \sum_{abcd} \int \mathrm{d}x_a \mathrm{d}x_b \mathrm{d}z_c G_{a/A}(x_a) G_{b/B}(x_b) D_{C/c}(z_c) \frac{\hat{s}}{z_c^2 \pi} \frac{d\sigma}{d\hat{t}}(ab \rightarrow cd) \delta(\hat{s}+\hat{t}+\hat{u}), \tag{3}$$

where A and B are the incoming hadrons, X=anything, C=high-p_{T} particle and $\hat{s}$, $\hat{t}$ and $\hat{u}$ are so-called Mandelstam variables of the hard subprocess that contain information about the energy, momentum and angles of the particles in the scattering process. For a $2 \rightarrow 2$ process of massless partons, $\hat{s} + \hat{t} + \hat{u} = m_1^2 + m_2^2 + m_3^2 + m_4^2 = 0$, where m_1 is the mass of particle 1, and likewise for particles 2, 3 and 4.

This depiction of pQCD was done in lowest order leading-twist framework. Nowadays the next-to-leading order (NLO) QCD is used for the cross section calculation, as in [3]. It takes into account more complicated interactions than lowest order (LO), but one must in turn use the appropriate parton distribution functions and fragmentation functions with the NLO hard cross sections.

In addition to collinear fragmentation of quarks and gluons illustrated in Fig. 3, there has been evidence of so-called higher-twist (HT) processes in experimental hadronic data. In HT processes, the outgoing hadron is produced directly in the hard subprocess. These kind of hadrons, unlike the leading-twist ones, would be accompanied by no activity in their vicinity due to the lack of fragmentation. Studying whether the so-called isolation cut can increase the sensitivity to HT processes is the main goal of this thesis.

The HT processes have also attracted attention in the field of heavy ion collisions. One example is the so-called "Baryon Anomaly", found in measurements of high-p_{T} baryon production in heavy ion collisions [40]. It was shown at RHIC (Relativistic Heavy Ion Collider) in 2008 that as the collisions became more central, i.e., the overlapping interaction region of the nuclei increased, three effects were observed. The first was the increase in the proton-to-pion ratio at $2 < p_{\mathrm{T}} < 6$ GeV/c, which was inconsistent with the leading-twist

pQCD picture of hard scattering followed by fragmentation. The second was the increased power-law fall-off at fixed $x_{\rm T}$, i.e., large scaling index n of the charged particle (p and $\bar{p}$) production cross section in central collisions. In peripheral collisions (small overlap between nuclei), the scaling exponent was in agreement with NLO leading-twist QCD, but was rising above the predictions when centrality was increased. In Fig. 4 the exponents for π^0 (left) and charged hadron (right) production are shown. The Figure is from [41]. Finally, a decrease of the number of same-side hadrons correlated with a baryon (proton) trigger was observed as the centrality was increased. In contrast, the number of particles associated with a meson ($\pi^{\pm}$, $K^{\pm}$) was shown to increase with centrality. This difference between the nuclear dependence of pion and proton production is inconsistent with the pQCD picture of hard scattering followed by fragmentation. In [40], these results were interpreted as a consequence of HT processes in the heavy ion data.

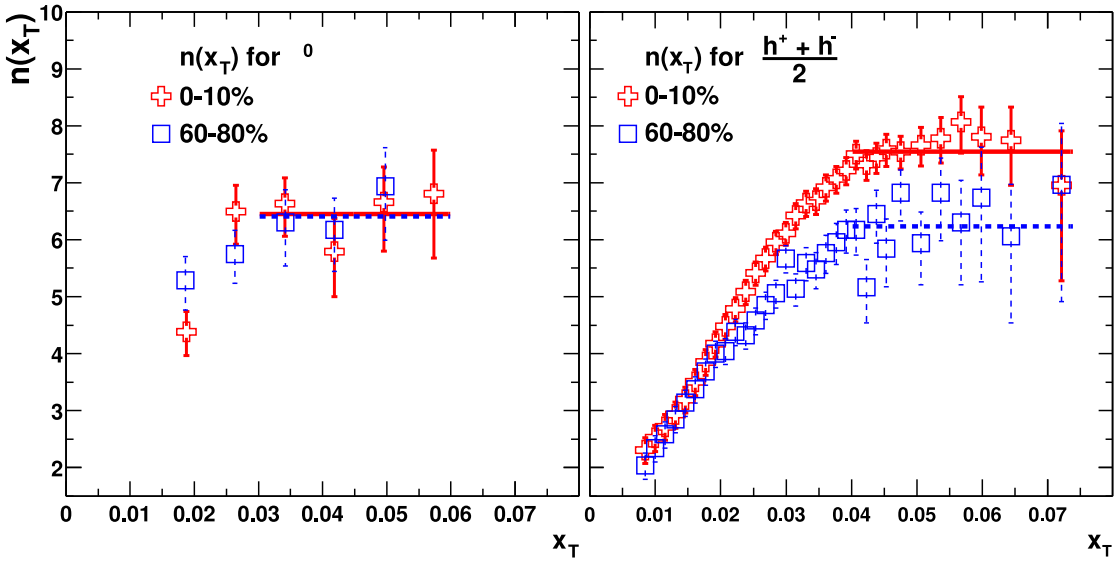

Figure 4: Effective power-law fall-off of the inclusive cross section for π^0 and charged particle hadroproduction at fixed $x_{\rm T}$ and fixed θ_{cm} at RHIC energies. The power law increases as a function of $x_{\rm T}$ and is different for central and peripheral collisions in the case of charged particle production. The charged hadrons include protons and anti-protons. From Ref. [41]

2 Historical background

2.1 History of x_{T} scaling & Higher-Twist (HT) processes

One of the basic distributions measured in proton-proton physics is the transverse momentum (p_{T}) spectrum of inclusive particles. Theoretically p_{T} can range from 0 to half of the center-of-mass energy, $\sqrt{s}/2$ of the collision. The distribution can also be presented as a function of dimensionless variable $x_{\mathrm{T}} = \frac{2p_{\mathrm{T}}}{\sqrt{s}}$, which varies between 0 and 1.

The history of x_{T} scaling began when S.M. Berman, J.D. Bjorken and J.B. Kogut (BBK) [42] in 1971 calculated the cross section for high momentum particle production in proton-proton collision $p + p \rightarrow C + X$, where particle C had $p_{\mathrm{T}} \gg 1$ GeV/c. BBK stated that the charged partons of deep inelastic scattering (DIS) must scatter electromagnetically which may be viewed as a lower bound for the cross section at large p_{T}. At the time of BBK the QCD as it is known today didn't exist yet. Therefore, the asymptotic behaviour of the cross section was studied by electromagnetic processes as the QED was well known and tested at the time. They proposed a general form for cross sections with electromagnetic scattering at high p_{T}, which was

$$\sigma^{\mathrm{inv}} \equiv E\,\frac{\mathrm{d}^3\sigma}{\mathrm{d}p^3}(p + p \rightarrow C\ + \mathrm{X}) = \frac{4\pi\alpha^2}{p_{\mathrm{T}}^4} F(\frac{-\hat{u}}{\hat{s}}, \frac{-\hat{t}}{\hat{s}}). \tag{4}$$

Two main factors of eq. (4) are the $1/p_{\mathrm{T}}^4$, characteristic of single photon exchange, and the form factor F which scales, i.e is only a function of the ratio of Mandelstam variables. The work with x_{T} scaling continued at the CERN-ISR by Blankenbecler, Brodsky and Gunion (BBG) [43] who studied $p + p \rightarrow \pi^0 + X$ collisions. They noticed that for $p_{\mathrm{T}} < 8$ GeV/c the Fermilab and CERN-ISR π meson data the inclusive cross section was in fact proportional to p_{T}^{-8} and the BBK's p_{T}^{-4} behaviour was not present. To explain these results, the constituent interchange model (CIM) [43] was introduced, which contained production mechanisms of composite objects like mesons (object of one quark and one antiquark), baryons (three quarks or antiquarks) and diquarks that obeyed different scaling laws than the simple two-body

subprocesses. CIM contained also phenomenological couplings that carried dimensions, and therefore resulted in subprocesses that obeyed scaling laws that resulted in exponents larger than 4. This was the inspiration for a new general scaling form

$$\sigma^{\text{inv}} = \frac{1}{p_{\text{T}}^n} F\left(\frac{p_{\text{T}}}{\sqrt{s}}\right) = \frac{1}{\sqrt{s}^n} \frac{2^n}{x_{\text{T}}^n} F(x_{\text{T}}) = \frac{1}{\sqrt{s}^n} G(x_{\text{T}}) \tag{5}$$

where n gives the form of the force-law between constituents, $F\left(\frac{p_{\text{T}}}{\sqrt{s}}\right)$ and $G(x_{\text{T}})$ are dimensionless scaling functions, and where the substitution $x_{\text{T}} = 2p_{\text{T}}/\sqrt{s}$ was used. For the lowest order vector boson exchange processes $n = 4$ but for quark-meson scattering by the exchange of a quark, the exponent was found to be $n = 8$, as predicted by the CIM.

Another way to rationalize the scaling law (5) is to use dimensional analysis. A common feature for all two-body subprocess invariant cross sections is that their dimension is GeV^{-4} and that this dimension is brought by some combination of Mandelstam variables $\hat{s}$, $\hat{t}$ and $\hat{u}$. The kinematics of the process is completely fixed by two dimensional quantities $\hat{s}$ and p_{T} and two angles ϕ and θ. Any combination of p_{T}, $\hat{s}$ or x_{T} that preserve the dimensions, will end up in

$$\sigma^{\text{inv}} = \frac{p_{\text{T}}^4}{\hat{s}^4} G(x_{\text{T}}, \theta) = \frac{p_{\text{T}}^4}{256} \frac{x_{\text{T}}^8}{p_{\text{T}}^8} G(x_{\text{T}}, \theta) = \frac{1}{p_{\text{T}}^4} G(x_{\text{T}}, \theta), \tag{6}$$

which is the same as (5) with $n = 4$ [2]. All the dimensionless variables in the equation (6) are absorbed into the scaling function $G(x_{\text{T}}, \theta)$.

Later in 1975 R.F. Cahalan, K.A. Geer, J.Kogut and L. Susskind generalized the scaling law further by introducing the effective index $n(x_{\text{T}}, \sqrt{s})$, when it was discovered that the previously introduced exponent n depended on x_{T} and $\sqrt{s}$ [44]. To explicitly study the behaviour of the effective index, one can choose invariant cross sections from two data sets with different $\sqrt{s}$ with the same values of x_{T}. This allows one to cancel out the dimensionless scaling functions to get

$$n(x_{\text{T}}, \sqrt{s}_1, \sqrt{s}_2) = \frac{\ln(\sigma^{\text{inv}}(x_{\text{T}}, \sqrt{s}_2)/\sigma^{\text{inv}}(x_{\text{T}}, \sqrt{s}_1))}{\ln(\sqrt{s}_1/\sqrt{s}_2)}. \tag{7}$$

A demonstration of x_{T} scaling of charged hadron production in proton-proton collisions measured by the CMS collaboration at CERN and CDF collaboration in Fermilab [45], along with a global power law-fit, is presented in the upper panel of Figure 5. Cross section values have been scaled by $\sqrt{s}^{4.9}$ and one can see how curves with different center of mass energies collapse on top of each other in high x_{T} range. The black points are for 7 TeV in CMS, red circles for 0.9 TeV in CMS, orange stars for 1.96 TeV in CDF, green crosses for 1.8 TeV CDF and yellow diamonds for 0.63 TeV CDF data. In lower panel, ratios of data to NLO predictions is shown for different center-of-mass energies [45].

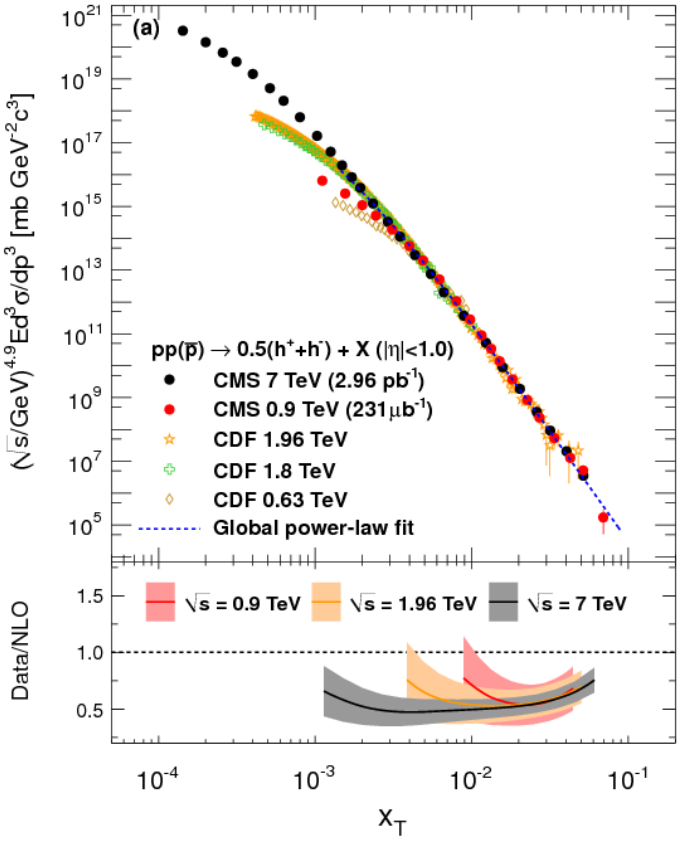

Figure 5: Cross section–x_{T}-distributions scaled by $(\sqrt{s})^{4.9}$ of inclusive charged particles (upper panel) to demonstrate x_{T} scaling of charged particles with different center of mass energies ($\sqrt{s}$ in TeV). In lower panel, a ratio between data and NLO QCD calculation is shown. The Figure is from [45].

The term "higher-twist" (HT) refers to contributions that are suppressed by powers of large momenta, and therefore have large values of the effective index $n(x_{\rm T}, \sqrt{s}_1, \sqrt{s}_2)$. The term "twist" is historically related to operator product expansion, which was a tool used in the time of the CIM to obtain perturbative predictions for deep-inelastic scattering [2]. With leading-twist (LT) one means the standard processes of perturbative quantum chromodynamics (pQCD) within the collinear factorization [46].

The first calculations to estimate the size of the higher-twist contributions were carried out by Bagger & Gunion (1982). They found that the presence of the pion form factor in the $\gamma q \to \pi q$ process resulted in an extra factor of $1/\hat{s}$ in the cross section causing a $p_{\rm T}^{-6}$ scaling form in the sense of (5). The Mandelstam variable $\hat{s}$ is the square of the center-of-mass energy of the subprocess. As J.F Owens calculated in [2], at $\sqrt{s} = 31\,\text{GeV}$, scattering angle $\theta = 90°$ and $p_{\rm T}$ below 7 GeV/c the HT contribution suppressed by about 2 orders of magnitude relative to the LT predictions because of the pion form factor. When the edge of phase space is approached, the LT contribution steepens and the HT terms flattens leading to an eventual crossover. That happens in a region near $x_{\rm T} = 1$ where cross section is extremely small.

There are also other factors that cause deviations from LT such as color factors in $q\bar{q} \to \gamma M$ (M=meson), second structure function in the initial state, diquarks or $k_{\rm T}$ smearing [2]. If the colliding partons had some initial transverse momentum k_T, it would give rise to a smearing out of the $p_{\rm T}$ spectrum. Since the invariant cross section falls at the rate of an order of magnitude per GeV of $p_{\rm T}$ in this region, it would not take a large amount of smearing to make a significant effect. It is now known that the explanation for $n > 4$ scaling is due to the finite value of $k_{\rm T}$, the running coupling constant and the scaling violation in the PDF and the FF [3, 15]. There could also be additional smearing due to the j_T, the transverse component associated with the fragmentation in the final state. For photons, the exponent is predicted to be roughly one unit smaller, because of relative absence of fragmentation processes and one less power in α_s [3].

2.2 Higher-Twist prediction for isolated particles

A study of HT processes is presented by Arleo, Brodsky, Hwang and Sickles in [3]. They report a significant deviation of effective index n between hadronic data and leading-twist pQCD predictions at next-to-leading order (NLO). The discrepancy is largest at high values of x_{T}. However, for prompt photons and jets the difference is clearly smaller and they exhibit a scaling behaviour closer to NLO calculations. This discrepancy between theory and experiment brings evidence for a non-negligible contribution of higher-twist processes in hadronic collisions.

Arleo et al. approach the problem with the effective index by calculating the number of fields contributing in the subprocess with dimensional counting rules. It is stated that apart from scaling violations due to the QCD running coupling and evolution of parton distribution functions and fragmentation functions, the invariant cross section is expected to scale quite generally as ([47], [3] and [40])

$$\sigma^{\mathrm{inv}}(A\ B \to C\ \mathrm{X}) \propto \frac{(1-x_{\mathrm{T}})^{2n_{\mathrm{spectator}}-1}}{p_{\mathrm{T}}^{2n_{\mathrm{active}}-4}}, \tag{8}$$

where $n_{\mathrm{spectator}}$ is the number of constituent fields of A, B, and C not participating in the subprocess and n_{active} is the number of active fields participating in the hard subprocess. The denominator in (8) indicates that HT processes would result in larger exponents n of the $1/p_{\mathrm{T}}^{n}$ scaling form. On the other hand, the fall-off with x_{T} in the numerator would be slower, due to the lesser number of spectator fields. Therefore, one would expect HT processes to exist mainly in the region of large x_{T}, but not too large p_{T}.

For higher-twist processes there are more active fields and less spectator fields, and for leading twist processes the spectator fields dominate, as can be seen in an example Figure 6, [46]. In the LT picture (left side of Fig. 6) the number of active fields is 4 resulting in an exponent of $n = 2{\cdot}4 - 4 = 4$. On the right side of Fig. 6 there are 5 active fields participating in the process, which gives the value $n = 2{\cdot}5 - 4 = 6$ for the exponent.

The effective exponent n is then extracted from a NLO QCD calculation. They also obtain n

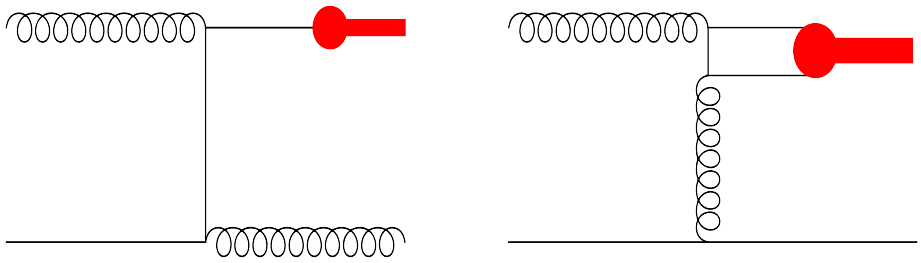

Figure 6: Left: An example of a conventional leading twist pQCD picture, a $2 \to 2$ process followed by fragmentation into a pion. Right: Direct higher-twist picture, the pion is produced directly in the hard process. Figure from [46].

from ten experimental data sets and compare the results with the NLO predictions. Effective exponents from the experiments are plotted in the left panel of Figure 7, [3]. The difference between experimental and NLO exponent $\Delta \equiv n^{exp} - n^{\mathrm{NLO}}$ was then calculated and plotted with the compilation of exponents in the right panel of Figure 7.

There is a significant difference between experimental data and QCD calculation for hadrons seen on the right side of Fig. 7. In contrast, jet and photon data are in excellent agreement with NLO prediction. This would lead to a natural explanation for the hadron data, the presence of important HT contributions from processes in which the detected hadron appears in the hard subprocess.

The exponent extracted from prompt photon data is closer to the $n = 4$ limit than the exponent obtained from hadron measurements, especially at large values of x_{T}. The difference between photons and hadrons is roughly one unit for n.

Another indication for HT effects is the larger exponent observed for protons than for pions. According to (8) the p_{T} exponent for pions ($n_{\mathrm{active}} = 5$) should be $2 \cdot 5 - 4 = 6$ and for protons ($n_{\mathrm{active}} = 6$) it should be $2 \cdot 6 - 4 = 8$, resulting in difference of 2 instead of 0 as the LT calculation predicts [3]. However, the data from ISR experiment gives a difference of 1, which reflects the mixture of LT and HT contributions to the cross section.

Also, predictions for HT contributions in pp collisions at RHIC and the LHC were given in [3]. The prediction was carried out by calculating the difference Δ between the exponent of the

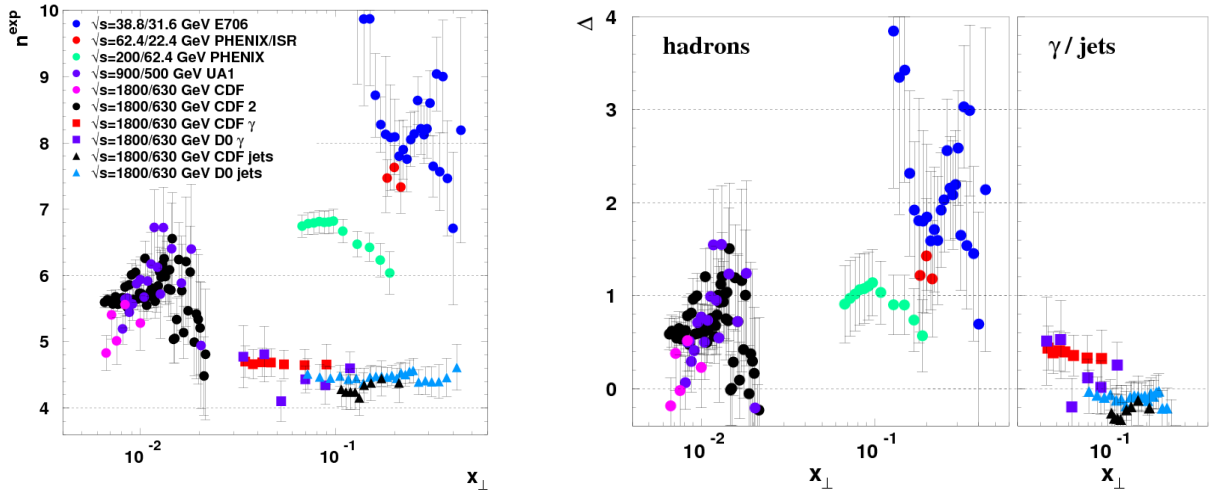

Figure 7: Left: Values of n^{exp} as a function of x_{T} for $h^{\pm}/\pi^0$ (circles), γ (squares) and jets (triangles). Right: $\Delta \equiv n^{exp} - n^{\mathrm{NLO}}$ as a function of x_{T}. Figure by Arleo et al. from [3].

leading-twist NLO prediction and the experimental parametrization of a 2-component model

$$\sigma^{\mathrm{model}}(pp \to \pi\ \mathrm{X}) \propto \frac{A(x_{\mathrm{T}})}{p_{\mathrm{T}}^4} + \frac{B(x_{\mathrm{T}})}{p_{\mathrm{T}}^6} \tag{9}$$

for the cross section, where A represents the LT and B the HT contribution. The prediction for RHIC (blue area on Fig. 8) is made by choosing $\sqrt{s} = 200, 500\,\mathrm{GeV}$ and for LHC (red area on Fig. 8) by choosing $\sqrt{s} = 7\,\mathrm{TeV}$ compared to the $\sqrt{s} = 1.8\,\mathrm{TeV}$ at Fermilab's Tevatron. Preliminary data points from PHENIX measurements, obtained from [48] are plotted on top of the predictions in Figure 8 [46]. The data points seem to agree with the prediction within the error bars.

It is seen from Figure 8 that at LHC, smaller deviations with NLO expectations are expected because of the large values of $\langle p_{\mathrm{T}} \rangle$ probed at high energy. One could also reason that pQCD should agree better with experiments in LHC because of the higher momentum transfers and asymptotic freedom.

Arleo et al. also discuss the use of isolation cuts in the analysis [3]. The outgoing particle with the largest momentum in the event is called the "leading" particle. One typically chooses leading hadrons as triggers, and calls the rest of the particles as "associated" particles.

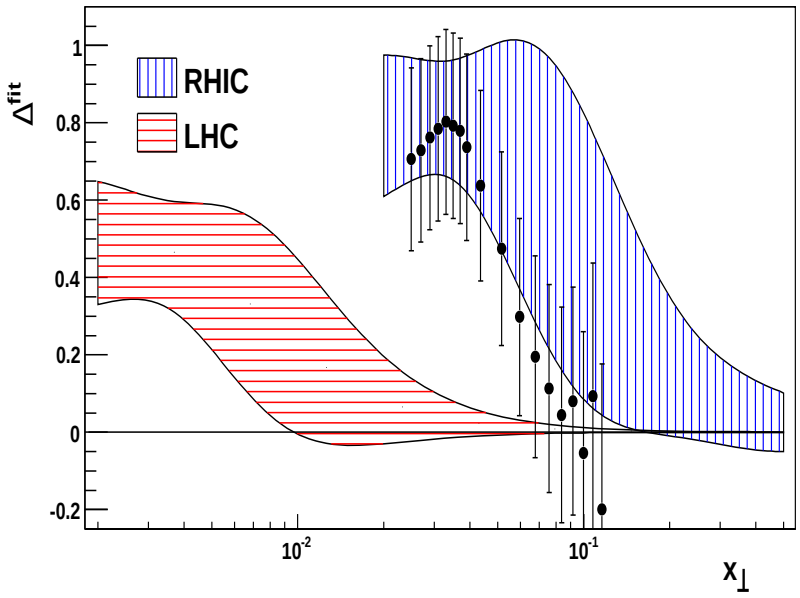

Figure 8: Predicted difference between the experimental and NLO scaling exponent at RHIC $\sqrt{s} = 200, 500$ GeV and the LHC ($\sqrt{s} = 7$ TeV as compared to $\sqrt{s} = 1.8$ TeV) based on a global fit of existing RHIC and Tevatron data, compared to PHENIX preliminary measurements. Figure by Arleo et al. from [3] for predictions only, and from [46] with data points gotten from [48].

A trigger hadron is called "isolated" when a jet cone around the trigger hadron of radius $R = \sqrt{\Delta\eta^2 + \Delta\phi^2}$, where $\Delta\eta$ is the pseudorapidity range and $\Delta\phi$ is the azimuthal angle coverage of the cone, is almost empty of other (hadronic) activity. This is checked by summing the p_{T} of every associated hadron in the cone, and declaring the trigger as "isolated" if the p_{T} sum is smaller than some limit defined by user, for example 10 % of the trigger hadron p_{T} or some fixed momentum limit in GeV/c. If the background is larger than the limit, the trigger hadron is called "non-isolated" .

It has been suggested that implementing an isolation cut , i.e. triggering on isolated hadrons, would enhance the HT contributions to hadron production by suppressing the leading twist (LT) processes. Hadrons originating from HT processes are produced directly in the hard process, which leads to less hadronic activity around the HT hadrons than those originating from leading twist processes that are accompanied by fragmentation. Isolation cuts should therefore suppress the LT processes efficiently thus enhancing the HT processes, which would

be observed as larger scaling exponents than in the inclusive channel.

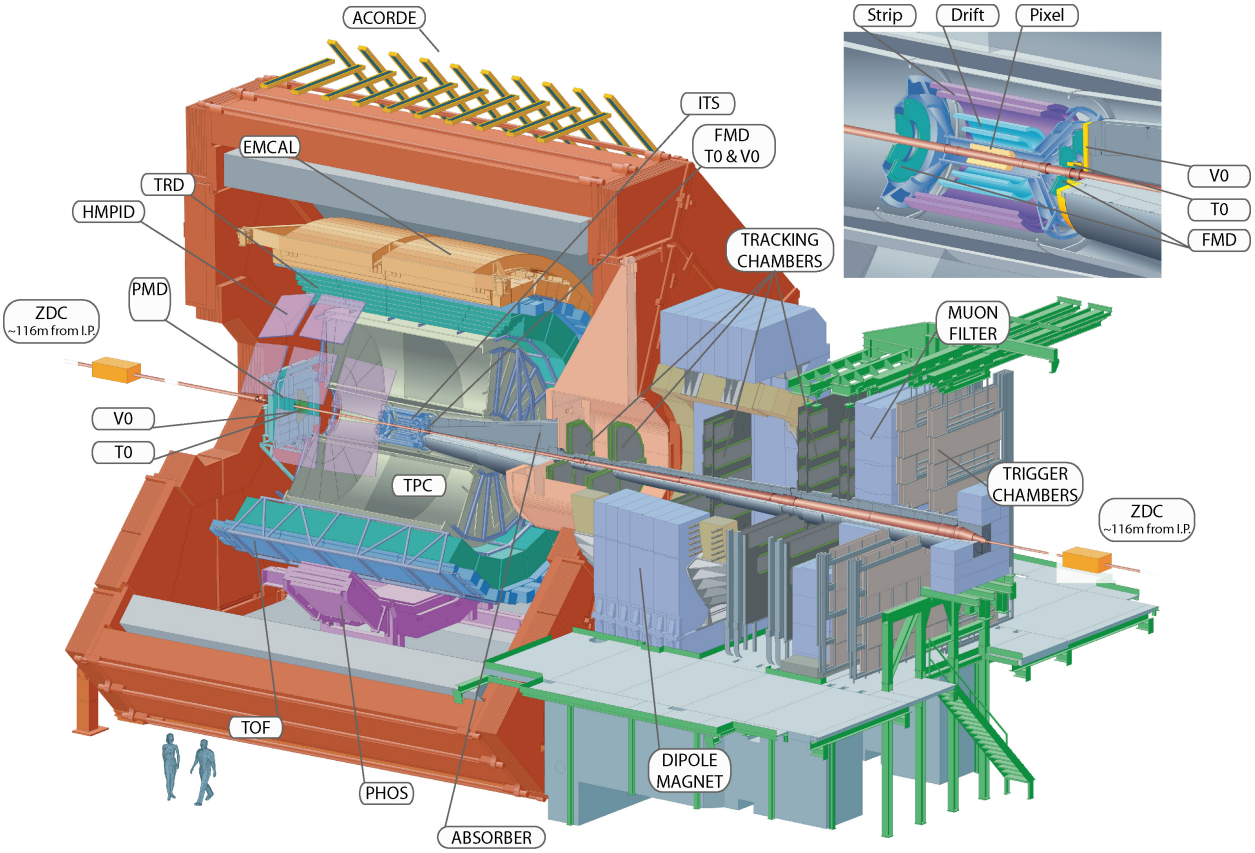

Figure 9: Schematic picture showing the ALICE detector with a zoom-in to the central part of the barrel. Figure is from the ALICE Figure Repository.

3 The ALICE experiment

3.1 The ALICE detector

The ALICE Collaboration, consisting of 36 countries, 132 institutes and 1200 members, is carrying out a dedicated heavy-ion detector experiment to explore the unique physics potential of nucleus-nucleus interactions at the LHC [1]. The aim of the ALICE experiment is to study the physics of quark-gluon plasma formed in heavy ion collisions. Practically all known techniques for particle identification are used within the ALICE detector, and it has an excellent identification and vertexing cabability down to almost 100 MeV/c. ALICE is also studying proton-proton and proton-lead collisions both as a comparison with lead-lead collisions and in physics areas where the detector is competitive with other LHC experiments. A schematic figure of the ALICE detector can be seen in Fig. 9.

ALICE consists of a central barrel part and a forward muon spectrometer [1]. The central part is embedded in a large solenoid magnet. The four detectors covering the central regions ($|\eta| < 0.9$) of ALICE are, outwards from the center, the Inner Tracking System (ITS), the Time-Projection Chamber (TPC), the Transition-Radiation Detector (TRD) and the Time-Of-Flight (TOF). The task of these detectors is to track and identify the particles and their interaction points. Other detectors that are also central but cover a smaller section of phase space, are the Photon Spectrometer (PHOS), the Electromagnetic Calorimeter (EMCal), the High-Momentum Particle Identification Detector (HMPID) and the ALICE Cosmic Ray Detector (ACORDE) [49]. The first two of the detectors mentioned have been the most important regarding this work. In addition, smaller detectors (ZDC, PMD, FMD, T0, V0) for global event characterization and triggering are located at small angles. A selection of performance plots (of particle identification) for ALICE subdetectors can be seen in Figure 10.

The innermost of the subdetectors, the ITS, spans the radii from 3.9 cm to 43 cm and consists of six layers of silicon detectors. The purposes of the ITS are the reconstruction of the vertices and contributions to particle tracking and identification via the measurement of the energy loss ($\mathrm{d}E/\mathrm{d}x$). The first two layers of ITS are called the Silicon Pixel Detector (SPD), which itself is sufficient to measure the charged particle multiplicity, but not for particle identification via energy loss. The third and fourth layer, called Silicon Drift Detector (SDD), provide the energy-loss information and particle identification with analog readout in contrast to binary readout of SPD. The outermost two layers, called Silicon Strip Detector (SSD) are arranged to provide a two-dimensional measurement of the track position together with an energy-loss measurement for identification.

The main tracking device of the ALICE detector is the TPC, which spans the radii from 0.85 to 2.5 meters. Combined with other central barrel detectors, it provides measurements of charged particle momentum, identification and the production vertex (point where the particle is coming from) in range of $|\eta| < 0.9$ for full radial length from particle momentum 200 MeV/c up to 100 GeV/c. The TPC is a gas detector with a volume of 88 m^3, a drift field

of 100 kV that stretches between the central electrode at $z = 0$ (z is the coordinate along the beam line) and the two readout planes at $z = \pm 2.5\,\mathrm{m}$ from the center of the barrel. It can measure a maximum of 160 clusters for a track, and can identify and reconstruct up to 20 000 tracks in one event.

A detector called the V0 plays an important role in the trigger system of the ALICE detector. The V0 consists of two arrays of scintillator counters which are placed on each side of the interaction region at $z \approx -0.9\,\mathrm{m}$ called V0A, and at $z \approx 3.3\,\mathrm{m}$ (V0C), covering the pseudorapidity ranges $-3.7 < \eta < -1.7$ and $2.8 < \eta < 5.1$, respectively [16].

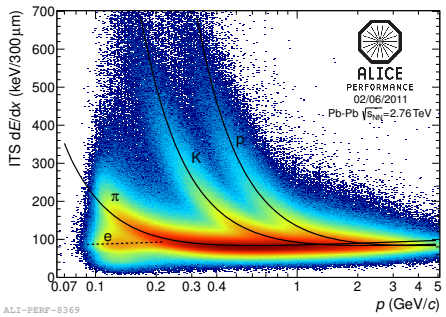

(a) ITS energy loss $\mathrm{d}E/\mathrm{d}x$ vs. p

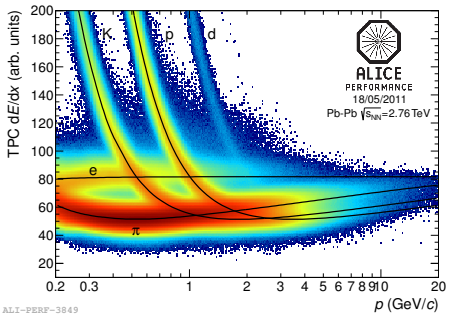

(b) TPC energy loss $\mathrm{d}E/\mathrm{d}x$ vs. p

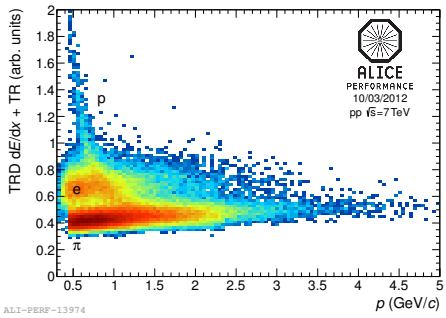

(c) TRD energy loss $\mathrm{d}E/\mathrm{d}x$

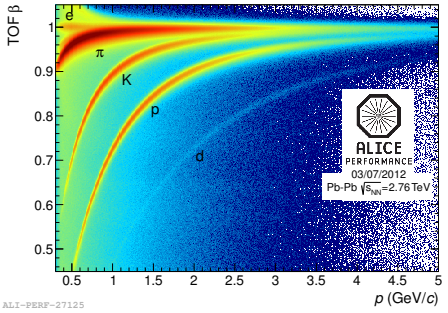

(d) TOF β vs. p

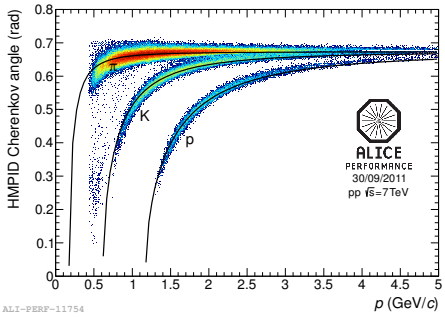

(e) HMPID Cherenkov angle vs p

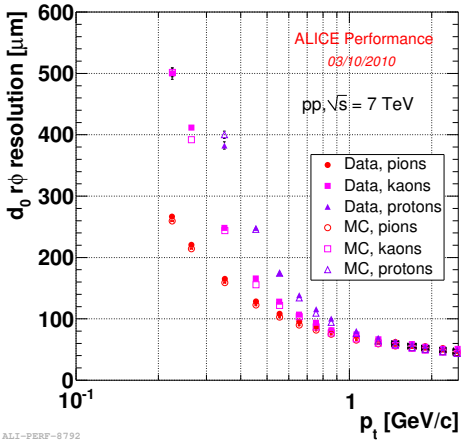

(f) Transverse impact parameter resolution. Convolution of the track-position and the primary-vertex resolutions

Figure 10: A collection of performance plots of the ALICE detector. Particle identification is done via energy loss for subdetectors ITS 10(a), TPC 10(b), TRD 10(c), via velocity for time-of-flight detector TOF 10(d) and via Cherenkov radiation angle in HMPID 10(e) with respect to momentum p. The transverse impact parameter resolution is shown in 10(f). Figures from the ALICE Figure Repository.

3.2 Track cuts and efficiency corrections

The goal of the track cuts is to select the so called primary charged particles and filter out any non-primaries, which are called secondary particles. In primary particles one includes all particles produced in the collision that originate from strong and electromagnetic decays and also from weak decays of charmed and beauty particles (e.g. hadrons containing c and b quarks). Particles that are feed-down products from strange weak decays or other secondary particles originating, for example, from hadronic interactions with the detector material, are suppressed by the cut [49]. In a simulation, such as PYTHIA [50], these kind of primary particles are known as final-state particles. The interaction of a particle with the detector material and response as a measured signal is described using GEANT simulator [51].

High quality primary tracks have to pass numerous criteria called track selection cuts. Track selection cut parameters used in this work can be seen in Table 1 [52]. A track was required to have a hit measured in any of the two SPD layers or in the first SDD layer. In addition, the track was required to be inside a region of $|\eta| < 0.8$ and to have a reconstructed vertex closer than 10 cm from the center of the detector. The track was required to have at least 70 clusters in the TPC with $\chi^2 < 4$, the maximum number of clusters being 160.

The tracking algorithm used in ALICE first tracked the clusters in the outer radii of the TPC, where the reconstruction of the track began. It continued inwards to the ITS adding new clusters to the track candidate whenever possible. The ITS tried to prolong the TPC tracks as close as possible to the primary vertex. Then, the track reconstruction was done in outward direction through all detectors starting from the ITS. Finally, to improve track parameters at the vertex, all tracks were refitted inwards from the TPC and the ITS, [53].

After the track was reconstructed, the distance of closest approach (DCA) of the track to the vertex must be smaller than the values given in Table 1. Kink daughters were removed from the event. An example of a kink daughter would be a Σ^- baryon decaying into a neutron and π^- by weak decay. The neutron would not be measured, but it would cause a kink in the trajectory at the decay point.

Accepted z vertex range	$\lvert z_{\mathrm{vertex}}\rvert < 10\,\mathrm{cm}$
Accepted pseudorapidity range	$\lvert\eta\rvert < 0.8$
Minimal Number of TPC Clusters	70
Maximal Chi2 Per one TPC Cluster	4
Maximal DCA To Vertex XY	$0.0182{+}0.0350\ p_{\mathrm{T}}^{1.01}$ [GeV/c]
Maximal DCA To VertexZ	2
Maximal χ^2 TPC Constrained Global	36
Maximal χ^2 Per Cluster in ITS	36
Hit in Any SPD layer or a hit in the first SDD layer	
Apply the XY and Z Distance of Closest Approach as rectangular cut	
Do not accept Kink Daughters	
Require TPC Refit	
Require ITS Refit	

Table 1: Track selection cut parameters

Since the detector was not ideal, it sometimes failed to reconstruct a particle or falsely declared a non-primary tracks as primaries (contamination) which are called fake tracks, despite the track cuts. To obtain the size of these effects, a Monte Carlo event generator, PYTHIA in this case, embedded in full detector simulation (GEANT3), was used [52]. By comparing the input MC sample to the output sample reconstructed with the detector response, one could get an overall reconstruction correction factor as a function of p_{T},

$$C(p_{\mathrm{T}}) = \frac{G_{\mathrm{trigvtx}}(p_{\mathrm{T}})}{M_{\mathrm{trigvtx}}(p_{\mathrm{T}}) + B(p_{\mathrm{T}})}, \tag{10}$$

where the subscript trigvtx indicates that the quantity was obtained in an event which triggered and where the vertex was reconstructed, G_{trigvtx} is the number of true charged physical primaries emitted in an inelastic event where a vertex was reconstructed (the initial MC sample), M_{trigvtx} is the number of reconstructed primary tracks and B is the number

of fakes and secondaries. M_{trigvtx} and B together form the output sample of reconstructed tracks. In Fig 11 (a) one can see an example of the track reconstruction efficiency function and in (b) the fraction of fake tracks in the reconstructed tracks , and in (c) the overall correction $1/C(p_{\text{T}})$, as a function of p_{T} for 7 TeV $p+p$ data.

In a study of underlying event in ALICE data [16], additional corrections are also introduced. Because of the tracking inefficiency, the leading track can sometimes escape detection and some sub-leading track will be selected as the leading one (leading-track misidentification). The sub-leading particle will have a different p_{T} and orientation, which leads to different orientation of the perpendicular cone which is measuring the UE activity. In the worst case the new perpendicular cone points to the direction of the real leading particle in the event, which will lead to the measuring of the hard process instead of underlying event.

Sometimes it can happen that two particles are azimuthally so close together that they will be measured as a single particle due to the finite two-track resolution of the detector. Correcting for these effects might be feasible regarding this isolation study, but the effects are small and these corrections are beyond the scope of this work.

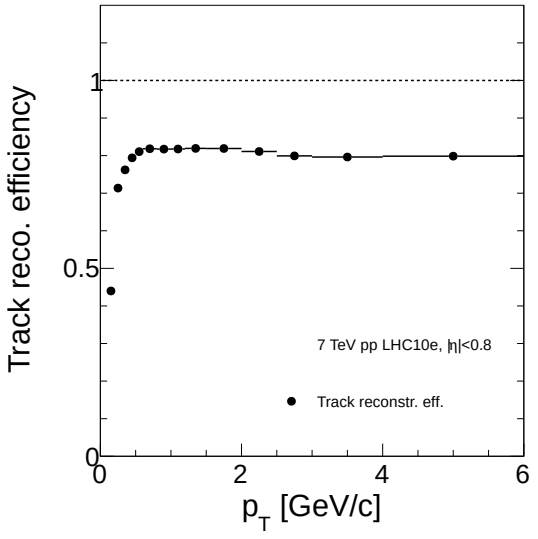

(a) Track reconstruction efficiency

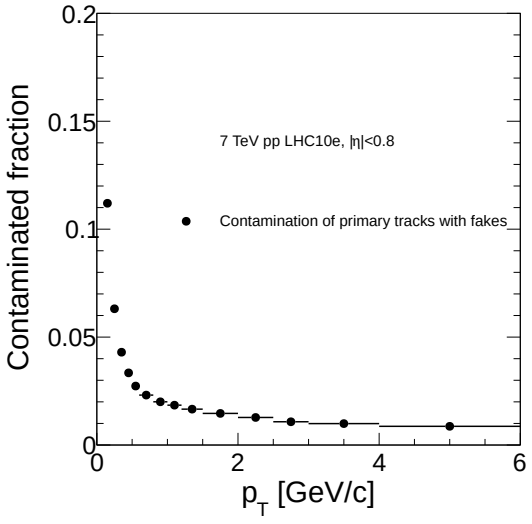

(b) Contamination of the reconstructed primaries with fake tracks

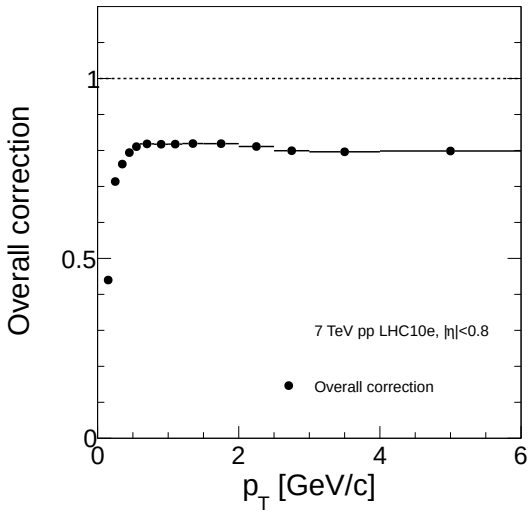

(c) Overall correction

Figure 11: Track reconstruction efficiency (a), contamination (b) and overall correction (c) as a function of p_{T} for $\sqrt{s} = 7$ TeV data [52].

3.3 Cross section measurement & van der Meer scan

To determine the inelastic cross section σ_{inel}, one has to measure the luminosity $\mathcal{L}$, which is a factor that relates the measured rate of events $\mathrm{d}N/\mathrm{d}t$ [Hz] to the cross section and

contains information about the densities and geometries of the beams and their interactions. It describes the ability of the collider to produce the required number of interactions or events. In electron-positron colliders, the luminosity could be measured as a rate of Bhabha scatterings ($e^+e^- \rightarrow e^+e^-$), because these processes were well known and their cross sections could be accurately calculated. For the proton-proton collisions in the LHC, there are no processes that have sufficiently well known cross sections and high enough production rate to be used directly for the luminosity calibration, and therefore the luminosity is determined from the machine parameters [54].

In the LHC proton beams, the protons are squeezed in bunches, each of which holds at design values approximately 1.15×10^{11} protons, and there are up to 2808 bunches in each proton beam. The design values have not been reached yet. The RF system focuses particle bunches in longitudinal regions called RF buckets. The nominal bunch spacing is 25 ns, while the separation of buckets is 2.5 ns, so there are 9 radio frequency (RF) buckets between the bunches. The particles that are located inside buckets that do not correspond to nominal bunch positions, are called satellite bunches [55]. The design luminosity of the LHC is $\mathcal{L} = 10^{34}$ cm^{-2}s^{-1}, which is delivered to the two high-luminosity experiments ATLAS and CMS. Other experiments, such as ALICE, are provided reduced luminosity due to their specific requirements.

The luminosity measurement in the LHC is done by sweeping the beams in transverse direction across each other and measuring the rate with respect to beam displacement in a so called van der Meer (vdM) scan. Using the beam sizes obtained by these sweeps and the measured number of charges per beam, one can calculate the luminosity. The method was proposed by S. van der Meer in 1968 at CERN ISR [56].

For minimum-bias triggering in ALICE, one can choose to trigger for example when one hit is recorded in the SPD or in either of the V0 arrays ($\mathrm{MB_{OR}}$). This kind of triggering should influence the event selection as little as possible. For the cross section measurement (van der Meer scan) in [57], a time coincidence between the two V0 scintillator arrays was used as a

trigger ($\mathrm{MB_{AND}}$). The rate for this trigger is

$$\frac{\mathrm{d}N}{\mathrm{d}t} = A \times \sigma_{\mathrm{inel}} \times \mathcal{L}, \tag{11}$$

where A takes into account the acceptance and efficiency of the trigger requirement in question. Therefore, if one first determines the factor A using Monte Carlo event generator together with the ALICE detector simulation and then measures simultaneously the rate and the luminosity, the cross section can be determined.

The current of the proton bunches is measured with coils that are arranged around the beam pipe, and van der Meer scans are used to study the geometry of the beam interaction region. For a single proton bunch pair head-to-head collision without crossing angles or beam offsets, the luminosity is given by

$$\mathcal{L} = f\frac{N_1 N_2}{h_x h_y}, \tag{12}$$

where f is the revolution frequency of the bunches in the accelerator, N_1 and N_2 the number of protons in bunches 1 and 2, and h_x, h_y are the effective transverse widths of the interaction regions. The effective transverse width, or "beam height", as called in [56], is defined as

$$h_{\mathrm{eff}} = \frac{\int S_1(k)\mathrm{d}k \cdot \int S_2(k)\mathrm{d}k}{\int S_1(k) \cdot S_2(k)\mathrm{d}k}, \tag{13}$$

where $S_1(k)$ and $S_2(k)$ are the beam densities as a function of transverse coordinate k. If the beam 2 has a displacement d, the rate $R(d)$ is equal to

$$R(d) = C\int S_1(k) \cdot S_2(k-d)\mathrm{d}k, \tag{14}$$

where C is an unknown factor. Now the objective is to prove that the beam height can be expressed as a function of the rates. This can be done by first writing the following equality

$$\frac{\int \left(C\int S_1(k) \cdot S_2(k-d)\mathrm{d}k\right)\mathrm{d}d}{C\int S_1(k) \cdot S_2(k)\mathrm{d}k} = \frac{\int \left(\int S_1(k) \cdot S_2(k-d)\mathrm{d}d\right)\mathrm{d}k}{\int S_1(k) \cdot S_2(k)\mathrm{d}k}, \tag{15}$$

where A has been cancelled out and the integration variables have been swapped. Because the integrals are calculated over the entire region where the integrands are non-zero,

$$\int S_2(k-d)\mathrm{d}d = \int S_2(k)\mathrm{d}k. \tag{16}$$

Finally, it is shown that using (15) and (16)

$$\frac{\int \left(S_1(k)\cdot\int S_2(k-d)\mathrm{d}d\right)\mathrm{d}k}{\int S_1(k)\cdot S_2(k)\mathrm{d}k} = \frac{\int S_1(k)\mathrm{d}k\cdot\int S_2(k)\mathrm{d}k}{\int S_1(k)\cdot S_2(k)\mathrm{d}k} = h_{\mathrm{eff}}, \tag{17}$$

which demonstrates that the scan will give the beam width for all beam shapes S. The width can also be expressed in terms of rates as

$$h_{\mathrm{eff}} = \frac{\int R(d)\mathrm{d}d}{R(0)}. \tag{18}$$

Therefore, the parameters h_x and h_y in (12) are obtained by first measuring the rate at V0 versus the displacement of the beams in horizontal and vertical directions, and then calculating the ratio of the area under the rate-vs.-displacement curve to the height at zero beam displacement. As an example, the horizontal and vertical displacement curves for vdM scan II performed at 7 TeV in ALICE can be seen in Fig. 12.

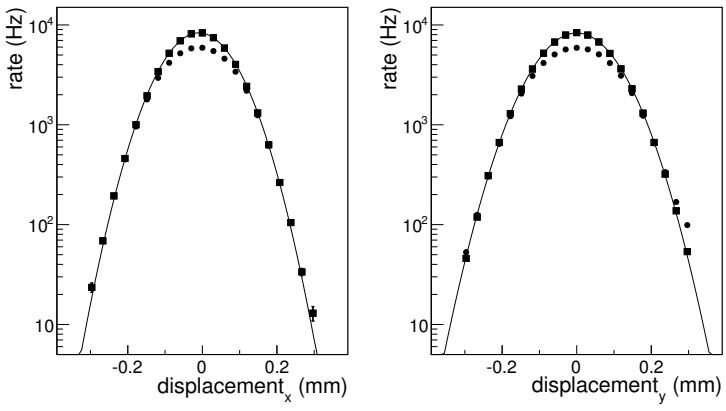

Figure 12: Trigger rates for horizontal (left) and vertical (right) displacements of the proton beams for van der Meer scan II performed at 7 TeV by the ALICE collaboration in [57]. Dots are raw trigger rates without corrections and squares are the rates with corrections. The purpose of the lines is to guide the eye.

The van der Meer method can be used for arbitrary beam shapes, but for Gaussian beam profiles the parameters can be calculated as

$$h_x = \sqrt{2\pi(\sigma_{1x}^2 + \sigma_{2x}^2)}, \tag{19}$$

$$h_y = \sqrt{2\pi(\sigma_{1y}^2 + \sigma_{2y}^2)},$$

where the σ_{ix} and σ_{iy} (beam index $i = 1, 2$) are the root-mean-squares of the beam sizes in the horizontal and vertical directions. The maximum beam displacement in case of ALICE was 0.4 mm, and the distance from the interaction point to the nearest V0 array was 0.9 m. To measure the vertex displacement with respect to beam displacement, both beams were moved in the same direction and the corresponding vertex positions were measured with the SPD, which gave a contribution to uncertainty in $A \times \sigma_{\text{inel}}$.

Several corrections had to be applied to the measurements to obtain the final inelastic cross section. It was taken into account that there can, for example, be protons circulating in the beam pipe that are outside bunches (ghost charges), background from beam-halo and beam-gas collisions, multiple collisions in a single bunch-crossing (pileup), accidental

triggers from noise, trigger from two separate collisions, imperfect centering of beams, satellite collisions at large displacements, and luminosity decay during the scan [57].

3.4 Absolute normalization

To normalize the real data p_{T} and x_{T} distributions per one inelastic event, a procedure called absolute normalization was used like in [49]. This procedure separates the total number of inelastic events into those where the vertex was reconstructed and to those where the vertex was not reconstructed, in which case a MC based correction had to be used to retrieve the vertex distribution.

The total number of inelastic events is

$$N_{evt} = \sum_{n=0}^{\infty} \int \mathrm{d}z I(z,n), \tag{20}$$

where $I(z,n)$ gives the number of inelastic events having n contributors to the reconstructed vertex in position range $[z, z+\mathrm{d}z]$. If the vertex was not reconstructed, then the number of contributors $n = 0$.

The first part of the number of inelastic events are those with a reconstructed vertex (having $n > 0$)

$$I(z,n) = E^{*}_{\mathrm{trigvtx}}(z,n)\tilde{C}_{\mathrm{vtx}}(z,n)\tilde{C}_{\mathrm{trig}}(z,n), \tag{21}$$

where E^{*}_{trigvtx} is the measured number of events that had a reconstructed vertex, and $\tilde{C}_{\mathrm{vtx}}$ and $\tilde{C}_{\mathrm{trig}}$ are correction factors for the vertex reconstruction efficiency and the trigger efficiency, respectively. These correction factors can be calculated using a MC event generator with a detector simulation, as

$$\tilde{C}_{\mathrm{vtx}} = \frac{E_{\mathrm{trig}}(z,n)}{E_{\mathrm{trigvtx}}(z,n)} \tag{22}$$

and

$$\tilde{C}_{\mathrm{trig}} = \frac{E_{\mathrm{all}}(z,n)}{E_{\mathrm{trig}}(z,n)}, \tag{23}$$

where E_{trigvtx} is the number of triggered inelastic events from the simulation that had a

reconstructed vertex, E_{trig} the number of inelastic events that triggered, and E_{all} the number of all inelastic events without any constraints. The factor $\tilde{C}_{\mathrm{trig}}$ connects the number of inelastic events to those that triggered with a certain minimum-bias trigger, ensuring that one can get correct cross section distributions by using the inelastic cross section instead of cross section for that specific trigger.

If a vertex was not reconstructed in the event, the correction was a little bit more complicated. The number of inelastic events without a reconstructed vertex ($n = 0$) is

$$I(z,0) = E^*_{\mathrm{trig}}(0)\alpha^*_{\mathrm{trig}}(z)F(z)\tilde{C}_{\mathrm{trig}}(z,0)f_{\mathrm{in}}, \tag{24}$$

where $E^*_{\mathrm{trig}}(0)$ is the measured number of triggered events without a vertex, f_{in} is a fraction of vertices reconstructed within $|z_{\mathrm{vertex}}| < 10$ cm and $\alpha^*_{\mathrm{trig}}(z)$ is the measured average distribution of vertex positions

$$\alpha^*_{\mathrm{trig}}(z) = \frac{\sum_{n=1}^{\infty} E^*_{\mathrm{trigvtx}}(z,n)}{\sum_{n=1}^{\infty}\int \mathrm{d}z E^*_{\mathrm{trigvtx}}(z,n)}. \tag{25}$$

In (24), the factor $F(z)$ is a ratio based on MC, in which the shape of the vertex distribution of events without reconstructed vertices are divided by the vertex distribution of events that had a reconstructed vertex as

$$F(z) = \frac{E_{\mathrm{trig}}(z,0)/\int \mathrm{d}z E_{\mathrm{trig}}(z,0)}{\sum_{n=1}^{\infty} E_{\mathrm{trigvtx}}(z,n)/\sum_{n=1}^{\infty}\int \mathrm{d}z E_{\mathrm{trigvtx}}(z,n)}. \tag{26}$$

In other words, MC data is used to help recovering the vertex distribution of the measured events where vertex was not reconstructed. Done in this way, the corrected number of inelastic events in case of $\sqrt{s} = 2.76$ TeV pp was for one period 2.84×10^7 while the raw number was 2.71×10^7, which is roughly a 5% difference.

4 Analysis

4.1 Analysis procedure

4.1.1 Particle selection and classification

The analysis of an event began by inspecting all the particles one by one in an event. Only charged final state charged hadrons were selected from the outgoing particles. The low p_{T} limit in the ALICE experiment is of the order of 150 MeV/c, so hadrons with $p_{\mathrm{T}} < 0.2$ MeV/c were rejected from the study. The overall correction as a function of p_{T} used in the study for pp at $\sqrt{s} = 7$ TeV can be seen in Fig. 11 (c). The inverse of this correction was used as a weight when storing the p_{T} information of a track. By checking every particle in the event, the hadron with the highest p_{T} was flagged as the leading hadron, or leading particle (LP), while the others were called associated particles.

The pseudorapidity acceptance was $|\eta| < 0.8$ in ALICE with a fiducial cut of 0.6, which means that trigger particles outside $|\eta| < (0.8 - 0.6) = 0.2$ were disregarded. This was necessary, because parts of the analysis also involved the measurement of particles inside a cone around the trigger. The fiducial cut ensured that the whole cone was inside the η acceptance in all cases. Trigger p_{T} bin borders were $3, 4, 5, 6, 8, 15, 45$ and 500 GeV/c. The last bin was chosen very high to ensure that all high p_{T} trigger particles would be considered in the analysis.

The isolation condition was checked for every particle by adding up the p_{T} of every associated final charged particle around it inside a cone that had radius $R = \sqrt{\Delta\eta^2 + \Delta\phi^2} = 0.4$, (see "Isol. cone" in Fig. 13). To declare a particle as isolated, the p_{T} sum in the cone was required to be less than 0.5 GeV/c. This choice of isolation was called the "absolute isolation". Additionally, it was studied how the results change if the isolation criteria was changed to "relative isolation", where it was required that the sum was less than 10 % of the trigger p_{T}.

When the type of a particle (charged in fiducial acceptance, charged in full acceptance, leading, isolated, and isolated leading) had been determined, it's p_{T} was filled in corresponding

histograms with the inverse of the correction as a weight to compensate for the particles the detector has missed. The low-p_{T} cutoff for leading particles was $p_{\mathrm{T}} > 3$ GeV/c.
The $1/p_{\mathrm{T}}$ weighted distributions were transformed to invariant cross sections by

$$E\frac{\mathrm{d}^3\sigma}{\mathrm{d}p^3} = \frac{\sigma_{\mathrm{inel}}}{N_{\mathrm{inel}}}\frac{1}{2\pi\Delta y}\frac{1}{p_{\mathrm{T}}}\frac{\mathrm{d}N}{\mathrm{d}p_{\mathrm{T}}}, \tag{27}$$

where σ_{inel} is the inelastic cross section[1] from [57], N_{inel} is the corrected number of inelastic events from absolute normalization and Δy is the rapidity interval. In this study, as an approximation, $\Delta\eta$ was used instead of Δy.

4.1.2 Underlying Event - activities in cones

One goal of the analysis was to find out if the isolation cut had any effect on mean Underlying Event (UE) activity, defined as the sum of all the processes causing the final hadronic state in a collision event excluding the hardest partonic interaction. These processes include fragmentation of beam remnants, multiple parton interactions, initial- and final-state radiation (ISR and FSR) [16]. Understanding the UE can also help in tuning the Monte Carlo event generators to produce the bulk background of the events as accurately as possible.
To measure the Underlying Event one should try to study the direction most sensitive to the UE and least sensitive to the hard scattering. This was assumed to be in the direction perpendicular to the leading hadron, as its high p_{T} suggests that is originating from a hard scattering. The activity of the UE was measured by constructing a cone ('signal cone') around the leading particle, and also a cone perpendicular to this trigger, the 'perpendicular cone', see Fig. 13. Then, the p_{T} sum of hadrons inside these cones were calculated and saved to corresponding histograms.
To get the perpendicular direction for the perpendicular cone, the trigger particle momentum vector was rotated by randomly adding or subtracting 90° to the azimuthal angle ϕ. The

[1] In PYTHIA, σ_{inel} is given by parameter sigmaGen in mb. The total number of accepted events is given by the parameter nAccepted. Because PYTHIA updates these parameters continuously during the run, the values must be extracted after all the events are generated [50].

direction obtained this way was perpendicular to the trigger particle only at mid-rapidity, but not perfectly so elsewhere in 3D space [2].

Finally, one could then compare the p_{T} activity in the signal cone (radius 0.4) around the trigger and in the perpendicular cone (radius 0.4), thus roughly differentiating the underlying event activity from the hard process.

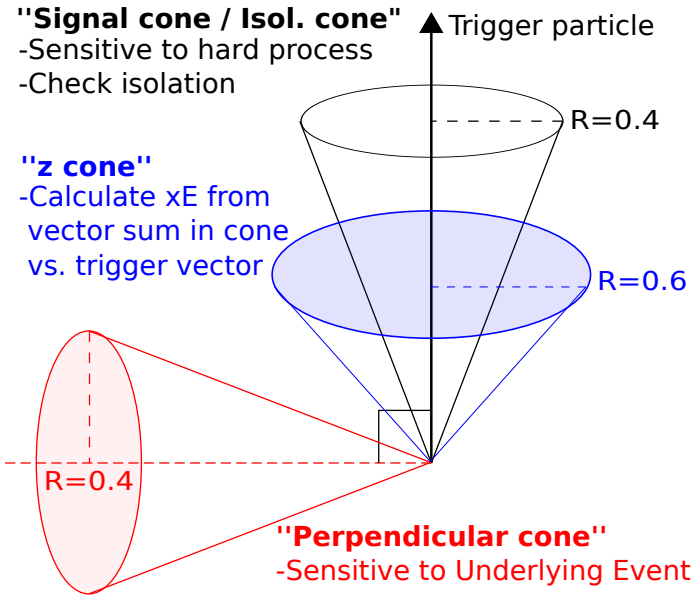

Figure 13: A visualization of cones and the corresponding radii used in the analysis. The isolation cone is needed for determining if the particle is isolated. Calculating an approximation for z requires the vector sum inside 'z cone'. The p_{T} sum in 'Signal cone' and 'Perpendicular cone' are used for analysing the underlying event and hard process activity in the event. The direction of the cones is always determined by the trigger particle.

4.1.3 Calculation of x_{E} as an approximation of z

The isolation cut is expected to bias the mean trigger z to larger values. The z is defined as $z = p_{\mathrm{Th}}/p_{\mathrm{Tq}}$, where p_{Th} is the p_{T} of the measured hadron and p_{Tq} the p_{T} of the parent parton that fragments into a jet, a collimated collection of hadrons and other particles.

The isolation cut restricts the amount of background activity in the jet to some p_{T} limit,

[2]Within the fiducial cut of 0.6 used in this work, the deviation from perfect perpendicularity was largest at $\eta = 0.2$. In that case, the angle between the two vectors was less than 3 degrees away from perpendicular.

whereas the trigger hadron can have large momentum. Therefore, the ratio of the trigger momentum divided by the jet momentum is expected to be larger for isolated particles than in the inclusive case where the background is not limited.

There are sophisticated jet reconstruction algorithms such as anti-k_{T} ([58]), but they were outside the scope of this work. Instead, a more straightforward approximation for a jet was made. It was assumed that at high p_{T} the leading charged particle in the event goes in the direction of the jet, and the jet was approximated by summing the momentum vectors of particles inside a cone of radius $R = 0.6$, "z cone" in Fig. 13. The leading particle was included in the sum. The mean UE activity background was not removed from the sum in this study.

A variable used in two-particle correlation analysis, called x_{E}, for a charged momentum sum in a cone around the leading particle, was used in [59] to approximate z. The two-particle $x_{\mathrm{E,2-particle}}$ is defined for away-side in [59] as

$$x_{\mathrm{E,2-particle}} = -\frac{\mathbf{p}_{\mathrm{Tt}} \cdot \mathbf{p}_{\mathrm{Ta}}}{\mathbf{p}_{\mathrm{Tt}}^2} = -\frac{p_{\mathrm{Ta}}}{p_{\mathrm{Tt}}} \cos(\Delta\phi), \tag{28}$$

where $\mathbf{p}_{\mathrm{Tt}}$ is the transverse momentum vector of the trigger and similarily $\mathbf{p}_{\mathrm{Ta}}$ for the associated particle, p_{Tt} and p_{Ta} are the p_{T} of the trigger and the associated particle, and where $\Delta\phi$ is the azimuthal angle between the two particles.

A slightly different version of (28) was defined in this study, however. The x_{E} was

$$x_{\mathrm{E}} = \frac{\mathbf{p}_{\mathrm{sum}} \cdot \mathbf{p}_{\mathrm{particle}}}{\mathbf{p}_{\mathrm{sum}}^2}. \tag{29}$$

where $\mathbf{p}_{\mathrm{sum}}$ is the momentum vector sum of the z cone directed to charged leading particle in the event, and $\mathbf{p}_{\mathrm{particle}}$ is the momentum vector of a particle inside the cone. The minus sign of (28) is omitted in (29), because in the near side $\cos(\Delta\phi) > 0$. The longitudinal projection between the trigger and the charged sum was calculated and divided by the norm of sum squared. In inclusive case, the x_{E} was calculated for all particles inside the cone centered by the leading particle. The mean x_{E}, or $\langle x_{\mathrm{E}} \rangle$, was then calculated for each cone p_{T} sum $p_{\mathrm{T,sum}}$

bin.

The estimate for the real fragmentation variable in this study was done with PYTHIA, because all final state particles, including the neutral ones, could be included in it. The charged x_{E} distributions were done mainly for a consistency check, as they could be compared and verified with real data. For two particle correlations the $\langle x_{\mathrm{E}} \rangle$ is insensitive to $\langle z \rangle$ [59]. However, using the momentum sum in cone instead of two particle correlations might recover the sensitivity to z, and at least the effects of isolation on x_{E} should be clearly visible.

4.2 Isolation criteria and PYTHIA parameter tuning

The isolation cut criteria used in this thesis were studied on Monte Carlo simulated PYTHIA (version 8, default tune) data in [60] without taking into account the finite tracking efficiency of a real experiment. Studying the data generated by PYTHIA event generator provided information on how different parameters and processes affected the data, as user can switch on and off different physical processes in the simulation. The simulation also helped evaluating the most feasible radius of the isolation cone. A larger cone is known to lead to a stricter isolation but with the expense of statistics, and PYTHIA helped finding the most useful compromise between isolation and statistics loss.

In [60] it was observed, using relative isolation cut 10 % of trigger p_{T}, that increasing the isolation radius from 0.2 to 0.4 and finally to 0.6, the fraction of isolated leading particles at high p_{T} decreased from (roughly) 30 % to 15 % and finally to 9 %. Also the ratio of isolated particles to inclusive particles approached 1 with decreasing p_{T}, especially when the isolation radius was 0.2. One possible explanation for this might be that as p_{T} gets smaller, particles are less likely to belong to a jet, and are distributed more evenly in the event. If the average density inside proton-proton events is small enough, it follows that it is likely for a cone of radius 0.2 around a low p_{T} particle to be almost empty, i.e. isolated. This ratio was quite strongly dependent on the size of the isolation radius, as the ratio got smaller while radius was increased. Therefore, using radius as small as 0.2 seems not sufficient when declaring if a particle is isolated or not. The mean value of x_{E} for $\sqrt{s} = 7\,\mathrm{TeV}$ was also seen to increase as

a function of isolation radius. This indicated that it makes sense to use as tight a criteria as possible as long as enough statistics is available for the analysis.

In this work, also the tracking efficiency was taken into account also in PYTHIA for a comparison to data. After the generation of an event, some particles were rejected from the event according to probability given by the track reconstruction efficiency curve, seen in 11 (a) at $\sqrt{s} = 7$ TeV. Then, this efficiency was used again as a weight when the trigger p_{T} distributions were saved. As an example of this effect, in Fig. 14 one can see ratios of data to PYTHIA vs. p_{T} before (a) and after (b) the efficiency-driven particle removal at $\sqrt{s}$ =2.76 TeV. The data to PYTHIA consistency of the p_{T} distributions was better than 20 % for $0.2 < p_{\mathrm{T}} < 12$ GeV/c.

Most notably, the deviation of p_{T} spectra of isolated particles between real data and PYTHIA became smaller. This helped to make data and simulation more comparable to each other, since measuring the low p_{T} background of particles was very important in this kind of isolation study. Of course, a full detector simulation together with PYTHIA events would have provided more accurate estimate of the low p_{T} physics than rejecting out particles with efficiency probability, but it was beyond the scope of this work. Also, the agreement is a sign that PYTHIA predicts the minimum bias processes quite accurately in this case. In the configuration of PYTHIA, minimum bias processes in addition to single- and double diffractive processes were turned on. To obtain physical primaries, particles with $c\tau > 10\,\mathrm{mm}$, where τ is the nominal lifetime of particles, were declared stable. This ensured that non-primary charged hadrons originating from, for example, weak decays of K mesons or Ξ baryons were not taken into account in the analysis.

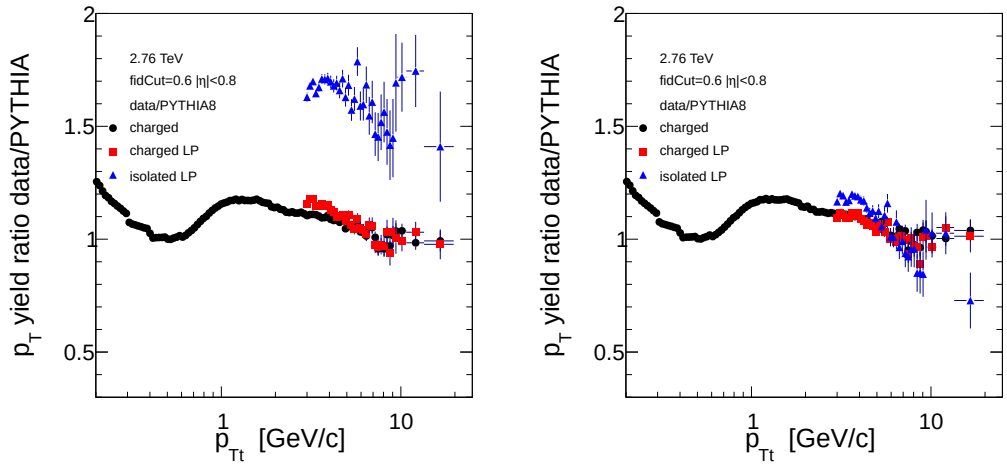

(a) Before efficiency correction applied in PYTHIA

(b) After efficiency correction applied in PYTHIA

Figure 14: Ratios of ALICE data/PYTHIA of $\frac{1}{p_{\mathrm{T}}}\frac{\mathrm{d}N}{\mathrm{d}p_{\mathrm{T}}}$ for charged hadrons before (a) and after (b) taking the efficiency in account for pp at $\sqrt{s} = 2.76$ TeV. Absolute isolation cut of 0.5 GeV/c with cone radius 0.4 was used.

In addition to charged hadrons, a PYTHIA run was made which took into account also the neutral particles, which were not accessible in the real data sample, even though they are present in the real-life events. This was done to estimate what is the effect of isolation on z to the whole sample instead of only the charged subset of it. The x_{E} distributions of charged hadrons and this special PYTHIA run at $\sqrt{s} = 7$ TeV can be seen in Fig. 15, where the black filled circles are for ALICE charged hadrons, hollow black circles for PYTHIA charged hadrons and red stars for PYTHIA with neutrals taken into account in the cone. In the case of charged hadrons, the estimate of z, in this work x_{E}, were observed to be very similar between ALICE and PYTHIA, which gave confidence that PYTHIA provides a fair description of the full result with neutrals included. Also, the distributions of charged and those with neutrals was more similar to each other in the case of isolated leading particles, than in the case of leading particles. The difference of charged and charged including neutrals was largest with the inclusive particles.

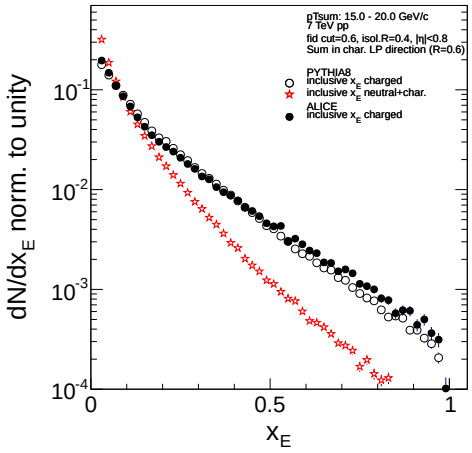

(a) x_{E} inclusive

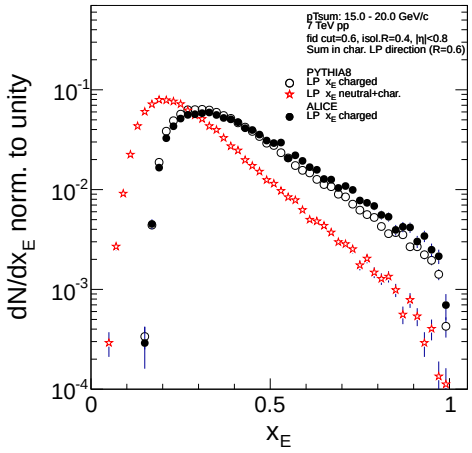

(b) x_{E} LP

(dN/dx_{E} for particles inside jet cone)

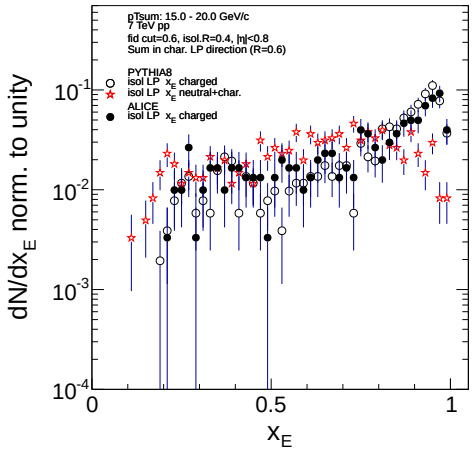

(c) x_{E} Isolated LP

Figure 15: Distributions of x_{E} for $15 < p_{\mathrm{T,sum}} < 20$ GeV/c inclusive (a), leading (b) and isolated leading (c) hadrons for pp at $\sqrt{s} = 7$ TeV. Hollow markers are for PYTHIA and filled markers for ALICE data. Absolute isolation cut with 0.5 GeV/c and radius 0.4 was used.

The mean x_{E} vs. $p_{\mathrm{T,sum}}$ at $\sqrt{s} = 7$ TeV is plotted in Figure 16, where (a) is for inclusive hadrons, (b) for leading hadrons and (c) for isolated leading hadrons. Markers are the same as in 15. The values of mean x_{E} were higher for isolated (absolute isolation) hadrons in both charged and neutral+charged cases in data and in PYTHIA. Also, PYTHIA provided similar values of mean x_{E} for leading hadrons and isolated hadrons as measured from real data. The

values of $\langle x_{\mathrm{E}} \rangle$ were systematically smaller in the case where neutrals were taken into account. In the case of charged and neutral isolated leading particles, there were not enough statistics to describe the $p_{\mathrm{T,sum}} > 50$ GeV/c part of the spectrum.

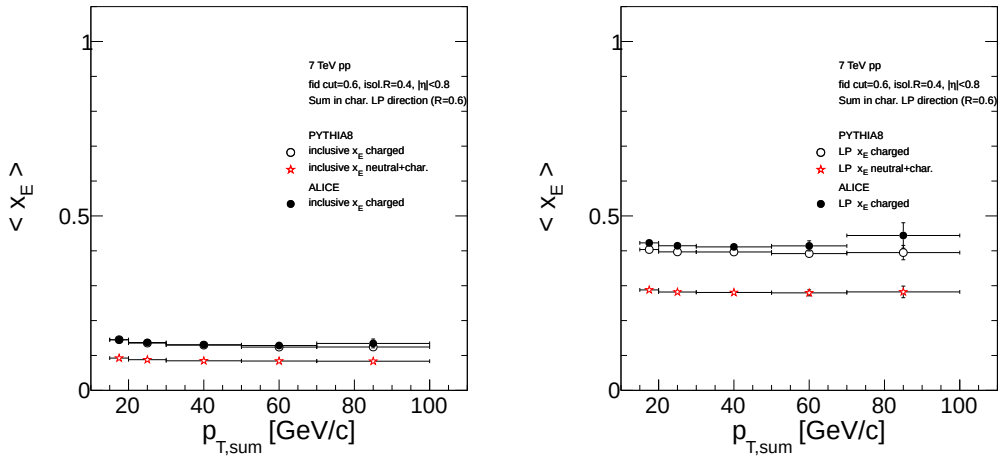

(a) $\langle x_{\mathrm{E}} \rangle$ inclusive

(b) $\langle x_{\mathrm{E}} \rangle$ leading

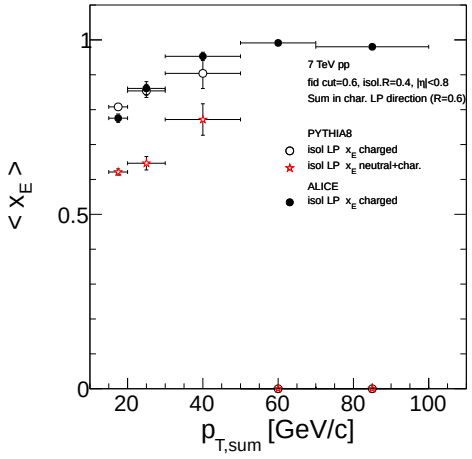

(c) $\langle x_{\mathrm{E}} \rangle$ isolated leading

Figure 16: $\langle x_{\mathrm{E}} \rangle$ for inclusive (a), leading (b) and isolated leading (c) hadrons for pp at $\sqrt{s} = 7$ TeV. Hollow markers are for PYTHIA and filled markers for ALICE data. Absolute isolation cut with 0.5 GeV/c and radius 0.4 was used.

4.3 Comparison of ALICE data to simulated data

4.3.1 p_{T} spectra

The study of isolated particles began by comparing the p_{T} spectra of isolated particles to all charged particles. In Figure 17, the invariant charged hadron p_{T} spectra for data and PYTHIA (left) and their data/PYTHIA ratios (right) of charged, leading and isolated leading particles with $\sqrt{s} = 2.76\,\mathrm{TeV}$ (upper plots) and 7 TeV (lower plots) are presented with isolation radius 0.4. In the p_{T} plots left side of Fig. 17 one can see the distribution of charged hadrons with fiducial cut (black circles), leading particles ('LP', red squares), isolated leading hadrons with absolute isolation ('IsolatedLP (Abs.)', blue diamonds) and isolated leading hadrons with relative isolation ('IsolatedLP (Rel.)', magenta crosses) with hollow markers for PYTHIA and filled markers for ALICE data. The p_{T} distributions were normalized with the corrected number of inelastic events.

The distributions between real data and PYTHIA agree within 20 %, as can be seen from the ratio plots in Fig. 17. This is consistent with preliminary *pp* results measured by ALICE at $\sqrt{s}$ =7 TeV (Fig. 18).

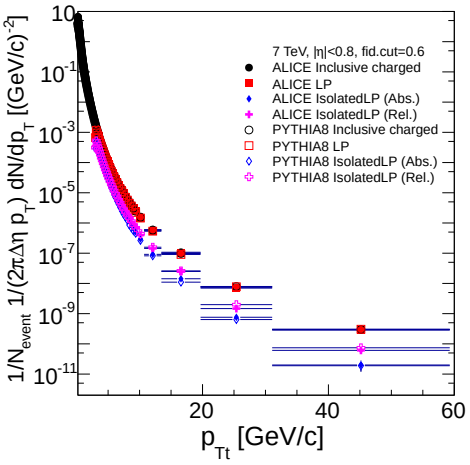

(a) Invariant yield vs. p_{T} at $\sqrt{s} = 7$ TeV

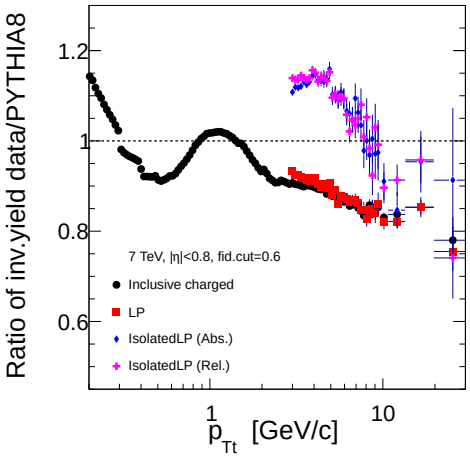

(b) Ratio of yields vs. p_{T} at $\sqrt{s} = 7$ TeV

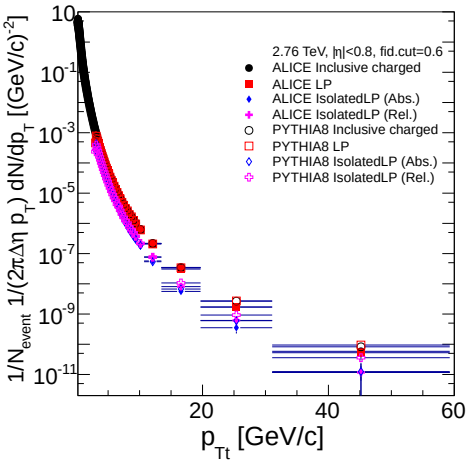

(c) Invariant yield vs. p_{T} at $\sqrt{s} = 2.76$ TeV

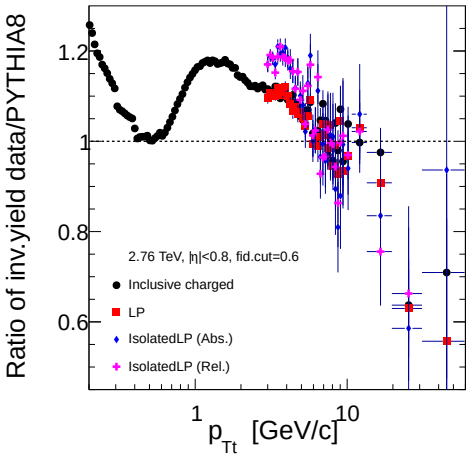

(d) Ratio of yields vs. p_{T} at $\sqrt{s} = 2.76$ TeV

Figure 17: Charged hadron invariant p_{T} yields (left) and ratios of yields (right) for trigger types charged, leading and isolated leading with isolation radius 0.4 for pp data at $\sqrt{s} = 7$ TeV (upper plots) and 2.76 TeV (lower plots). For p_{T} yield plots, hollow markers are for PYTHIA and filled markers for ALICE data.

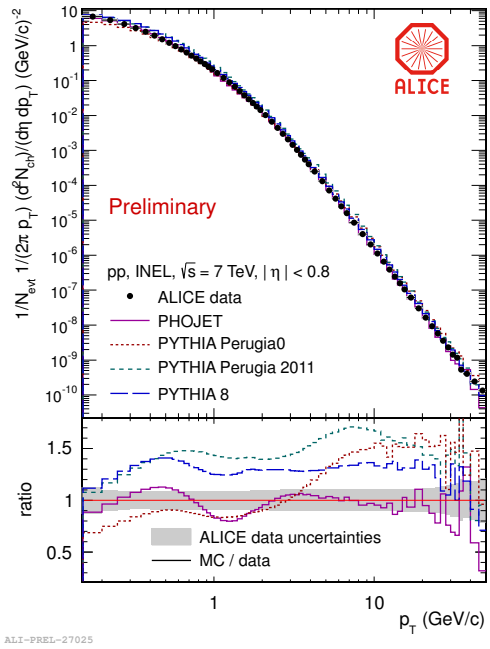

Figure 18: ALICE preliminary results of charged hadron invariant p_{T} yields (upper panel) measured by the ALICE collaboration in addition to predictions from MC generators PHOJET, PYTHIA6 with two different Perugia tunings, and PYTHIA8. In lower panel, the ratio of MC to data is shown.

In Figure 19, the ratios of invariant yields of leading to inclusive hadrons (left) and ratios of isolated to inclusive hadrons (right) with isolation radius 0.4 for pp at $\sqrt{s} = 2.76$ TeV (upper plots) and 7 TeV (lower plots) are presented for ALICE data (filled black circles) and PYTHIA data (red hollow squares). In both cases of leading/inclusive ratios, the fraction of leading particles is approaching 1 with increasing p_{T}, indicating that it is very probable for a high p_{T} hadron to be the leading one in the event. The fraction of isolated hadrons to inclusive hadrons drops from approximately 50 % to 10 %. This means that as the p_{T} is increased, it is less and less probable for the particle to be isolated. The ratio of isolated to inclusive hadrons for absolute and relative isolation cut cross each other at $p_{\mathrm{T}} = 5$ GeV/c, since after that the absolute criteria (0.5 GeV/c) becomes stricter than the relative (10 % of $p_{\mathrm{T}} > 5$ GeV/c), and vice versa for $p_{\mathrm{T}} < 5$ GeV/c.

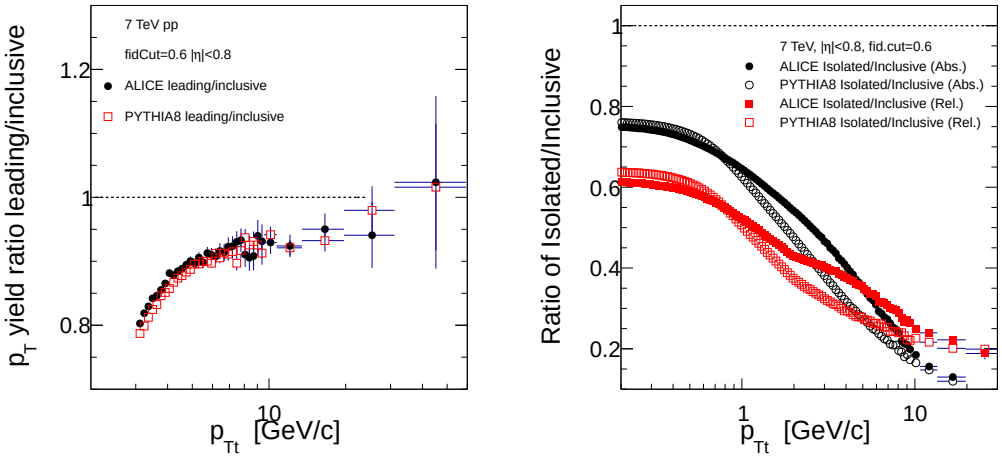

(a) Ratio of leading to inclusive hadrons vs. p_{T} at $\sqrt{s} = 7$ TeV

(b) Ratio of isolated to inclusive hadrons vs. p_{T} at $\sqrt{s} = 7$ TeV, $R_{isol} = 0.4$

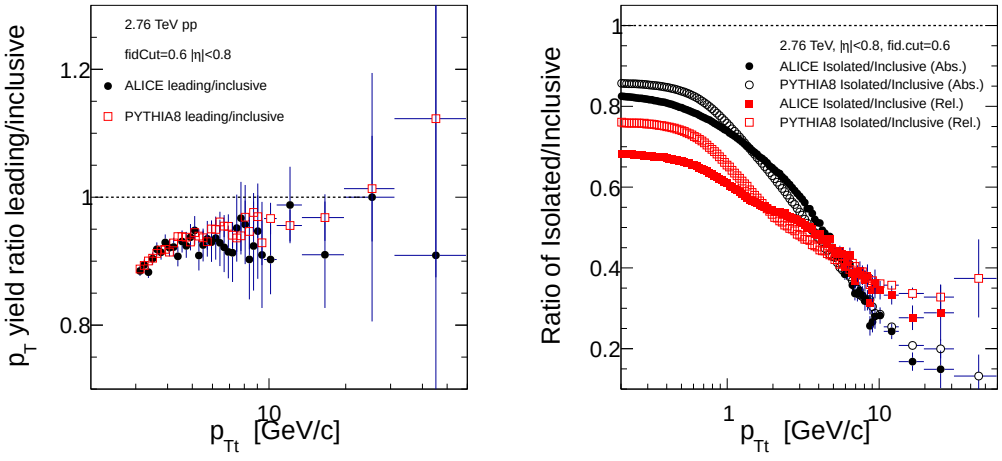

(c) Ratio of leading to inclusive hadrons vs. p_{T} at $\sqrt{s} = 2.76$ TeV

(d) Ratio of isolated to inclusive hadrons vs. p_{T} at $\sqrt{s} = 2.76$ TeV, $R_{isol} = 0.4$

Figure 19: Ratios of invariant p_{T} yields of leading to inclusive hadrons (left) and of isolated to inclusive hadrons (right) with isolation radius 0.4 for pp at $\sqrt{s} = 7$ TeV (upper plots) and 2.76 TeV (lower plots).

4.3.2 Underlying Event results

In Figure 20 plots of mean hadronic activity (p_{T} sum) with respect to trigger p_{T} are shown inside signal cone around the trigger particle (left) and inside a cone perpendicular to the leading trigger (right) with $\sqrt{s} = 2.76\,\mathrm{TeV}$ (upper plots) and 7 TeV (lower plots). The mean

p_{T} sum in perpendicular cone represents the underlying event (UE) activity. The trigger types are leading hadrons (red squares) and isolated (absolute isolation) leading hadrons (blue diamonds) with hollow markers for PYTHIA and filled markers for ALICE data. The radii of the signal cone, perpendicular cone and isolation cone were 0.4. In signal cone, the p_{T} activity increases as a function of p_{Tt} for the leading particles, but stays constant in case of isolated leading particles. By definition, the p_{T} sum inside a cone of R=0.4 must be smaller than 0.5 GeV/c for isolated particles. The signal cone thus displays the mean p_{T} sum inside the isolation cone, as the radius and the direction of the cones are the same in this case. Data and PYTHIA agree well with each other in signal cone activity. In the perpendicular cone, PYTHIA slightly underestimates the Underlying Event activity. One can also observe that the perpendicular cone activity is p_{Tt}-dependent, as it slowly increases as a function of p_{Tt}. Similar observations were presented in [16].

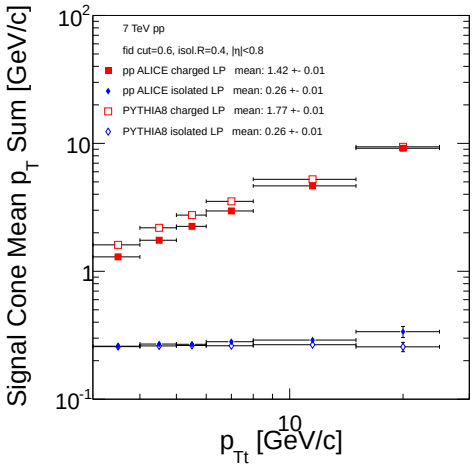

(a) Signal cone, 7 TeV

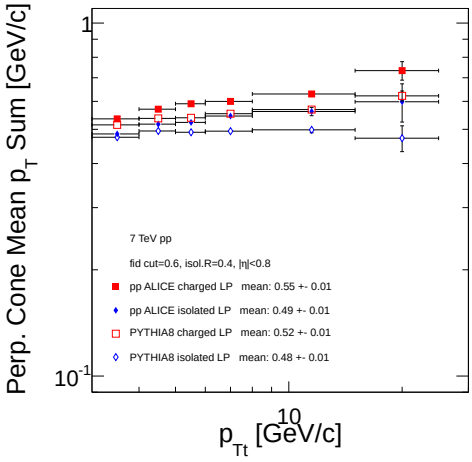

(b) Perp. cone, 7 TeV

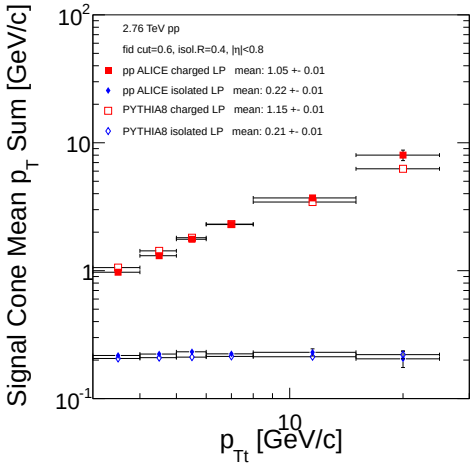

(c) Signal cone, 2.76 TeV

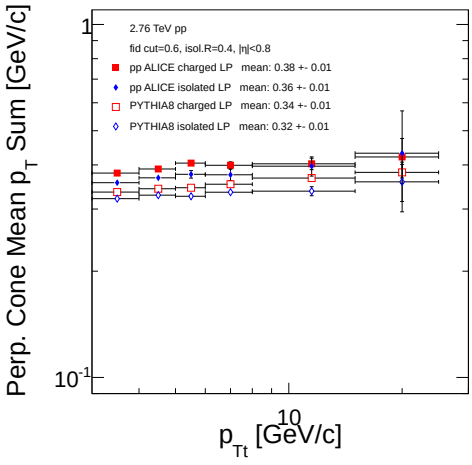

(d) Perp. cone, 2.76 TeV

Figure 20: Mean p_{T} sum of signal cone (left) and perpendicular cone (right) for trigger types leading and isolated leading with isolation radius 0.4 and absolute isolation limit 0.5 GeV/c for pp at $\sqrt{s} = 7$ TeV (upper plots) and 2.76 TeV (lower plots). Hollow markers are for PYTHIA and filled markers for ALICE data.

For a comparison between data and PYTHIA, in Fig. 21 data/PYTHIA ratios of p_{T} sums in signal cone (left) and in perpendicular cone (right) with isolation radius 0.4 for pp at $\sqrt{s} =$ 2.76 TeV (upper plots) and 7 TeV (lower plots) are presented. The markers are for inclusive hadrons (black circles), leading hadrons (red squares) and isolated (absolute isolation) leading hadrons (blue triangles). The deviation stays approximately inside 20 % for the whole p_{T}

range.

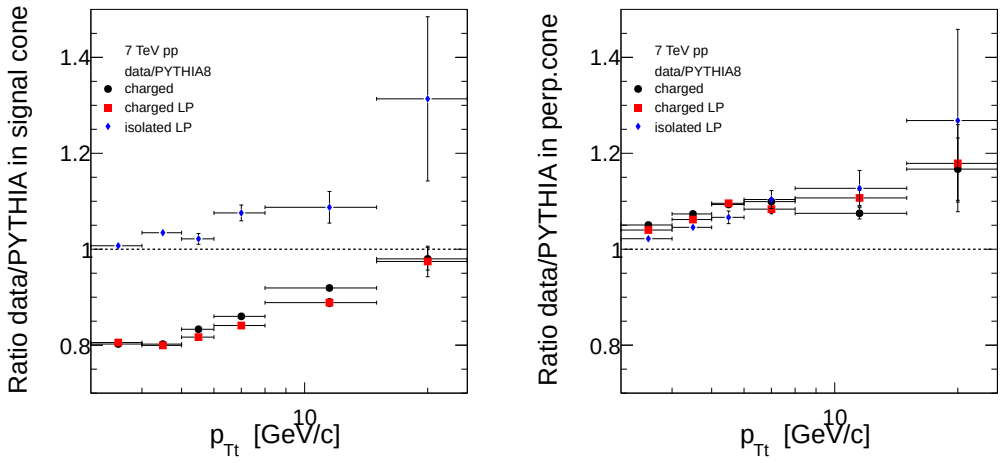

(a) Data/PYTHIA ratio in signal cone 7 TeV (b) Data/PYTHIA ratio in perp. cone 7 TeV

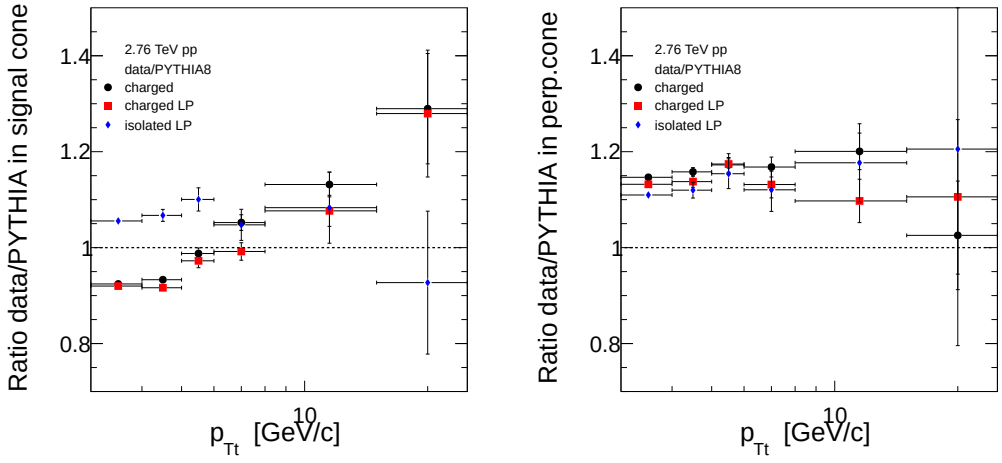

(c) Data/PYTHIA ratio in signal cone 2.76 TeV (d) Data/PYTHIA ratio in perp. cone 2.76 TeV

Figure 21: Ratio of data/PYTHIA of p_{T} sums in signal cone (left) and in perpendicular cone (right) with isolation radius 0.4 and absolute isolation limit 0.5 GeV/c for pp at $\sqrt{s} = 7$ TeV (upper plots) and 2.76 TeV (lower plots). Hollow markers are for PYTHIA and filled markers for ALICE data.

In Figure 22 (a) p_{T} distributions inside the signal cone around the trigger particle are shown at $\sqrt{s} = 7\,\mathrm{TeV}$. One can see that in case of isolated particles there cannot, by the choice of isolation criteria, be particles with $p_{\mathrm{T}} > 0.5$ GeV/c in the signal cone distribution, as the

sum must be under 0.5 GeV/c. In 22 (b), the p_{T} distribution is shown in the perpendicular cone, where it can be seen that the distribution is not very different for leading and isolated leading particles. Finally in 22 (c), the distribution is shown when the perpendicular cone distribution has been subtracted from the signal cone, when there is very small number, or none, of isolated particles left after subtraction.

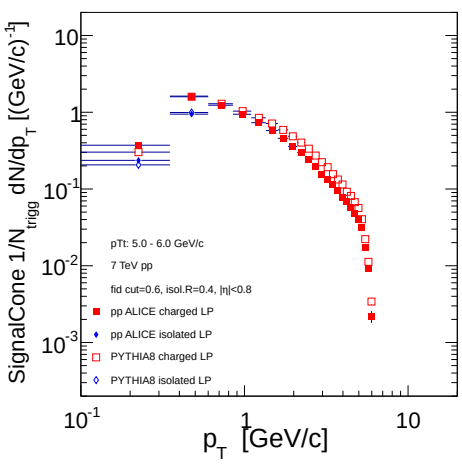

(a) Signal cone, 7 TeV

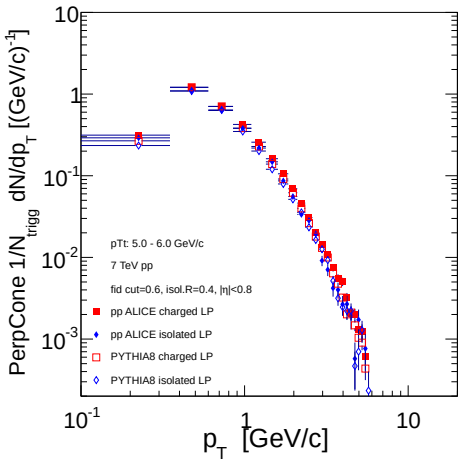

(b) Perp. cone, 7 TeV

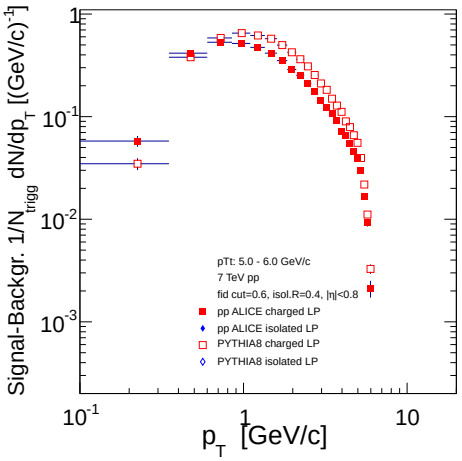

(c) Signal cone with perp. cone subtracted, 7 TeV

Figure 22: p_{T} distribution in signal cone (a), perpendicular cone (b), and signal cone with perp. cone subtracted (c). The isolation radius is 0.4, the absolute isolation limit 0.5 GeV/c, and the trigger has $5 < p_{\mathrm{Tt}} < 6$ GeV/c, from pp at $\sqrt{s} = 7\,\mathrm{TeV}$. Hollow markers are for PYTHIA and filled markers for ALICE data.

5 Results

5.1 x_{T} - cross section spectra and n

In left panel of Figure 23 one can see the x_{T} spectra scaled by $\sqrt{s}^{\langle n \rangle}$ and on the right panel the n as a function of x_{T}. The mean value of n, or $\langle n \rangle$, was calculated in the range of $6 \cdot 10^{-3} < x_{\mathrm{T}} < 3 \cdot 10^{-2}$ for every trigger type with the inverse of the cross section error as weight. Upper panels are for ALICE data and lower panels for PYTHIA at $\sqrt{s} = 7$ TeV and 2.76 TeV. In the scaled x_{T} spectra plots left side of Fig. 23, the markers are for 7 TeV: charged (violet triangles), leading hadrons (green stars), isolated leading hadrons (light blue circles) and at $\sqrt{s} = 2.76$ TeV: charged (black circles), leading hadrons (red squares) and isolated (abs.isolation) leading hadrons (blue triangles). The distributions for the same particle types with different $\sqrt{s}$ values collapse on top of each other in high x_{T}, demonstrating the x_{T} scaling.

Trigger particle types in n plots on right side of Fig. 23 are inclusive charged (black circles), leading (red squares), isolated leading (blue triangles), charged without fiducial cut (violet triangles) and isolated all including the non-leading ones (green stars).

The mean values of n are very similar in both PYTHIA and ALICE data. The increase of n can be seen for isolated particles, also in a non-leading case, when compared to inclusive and leading types where isolation was not implemented. The n curves become almost constant at high x_{T}, until one runs out of statistics, after which the values start to scatter and the error bars become large.

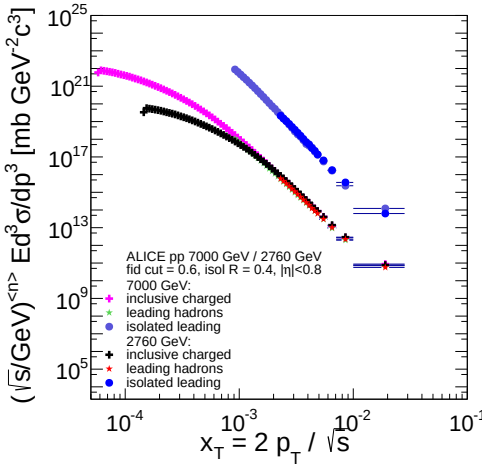

(a) ALICE x_{T}

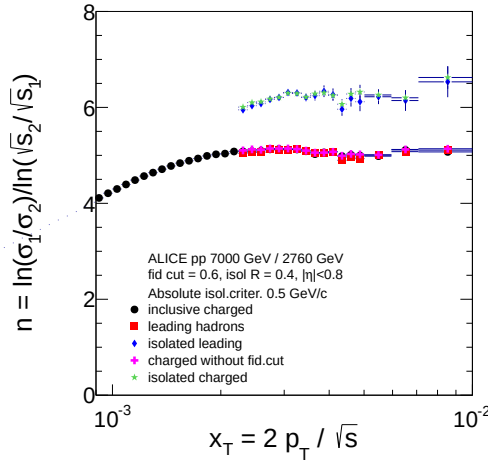

(b) ALICE n

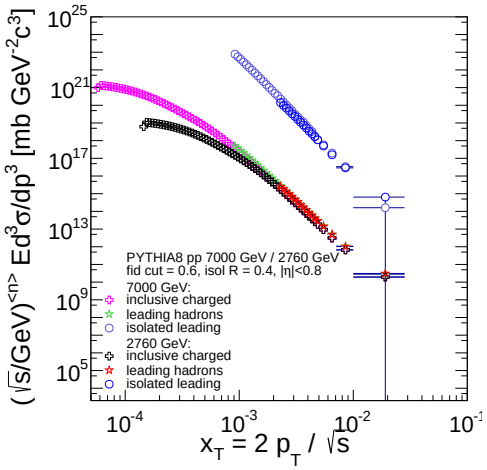

(c) PYTHIA x_{T}

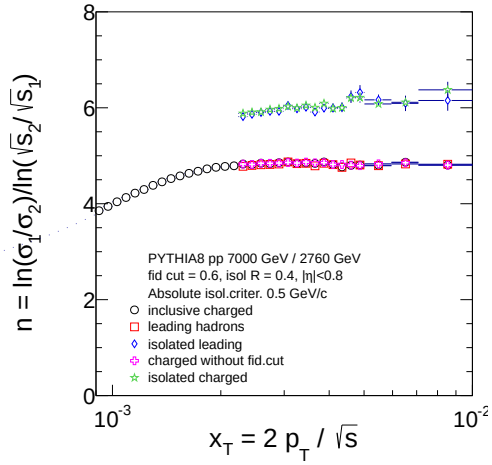

(d) PYTHIA n

Figure 23: Scaled x_{T} spectra and n at $\sqrt{s} = 7$ TeV / 2.76 TeV. Upper plots are for ALICE and lower for PYTHIA data. The scaling exponent n grows when isolation is applied, both in real data and in PYTHIA.

For comparison, the n of ALICE and PYTHIA8 are plotted on top of each other in Figure 24 (a), whereas the difference between n for isolated LP and LP is plotted on subfigure (b). In the plots, both the absolute (red squares) and the relative isolation (blue diamonds) criteria are visible. Filled markers are for ALICE, hollow markers for PYTHIA.

In Fig. 24 (a) and (b), the exponents of relatively isolated leading particles (blue markers) are in overall closer to leading particles (black markers) than those with absolute isolation

(red markers). PYTHIA estimates smaller values of n than measured from real data. Also, one can see that the Δn between isolated leading particles and all leading particles is larger in PYTHIA (hollow markers) at small x_{T} than in real data (filled markers), but similar at larger x_{T}.

There seems to be a small difference that stays almost constant between the n results of real data and PYTHIA. No systematical errors were taken into account in this analysis, but the difference might be explained by, e.g. errors in the cross sections, or in the absolute normalization process. This would be supported by the fact that the deviation between real data and PYTHIA got smaller once the Δn was studied instead of n.

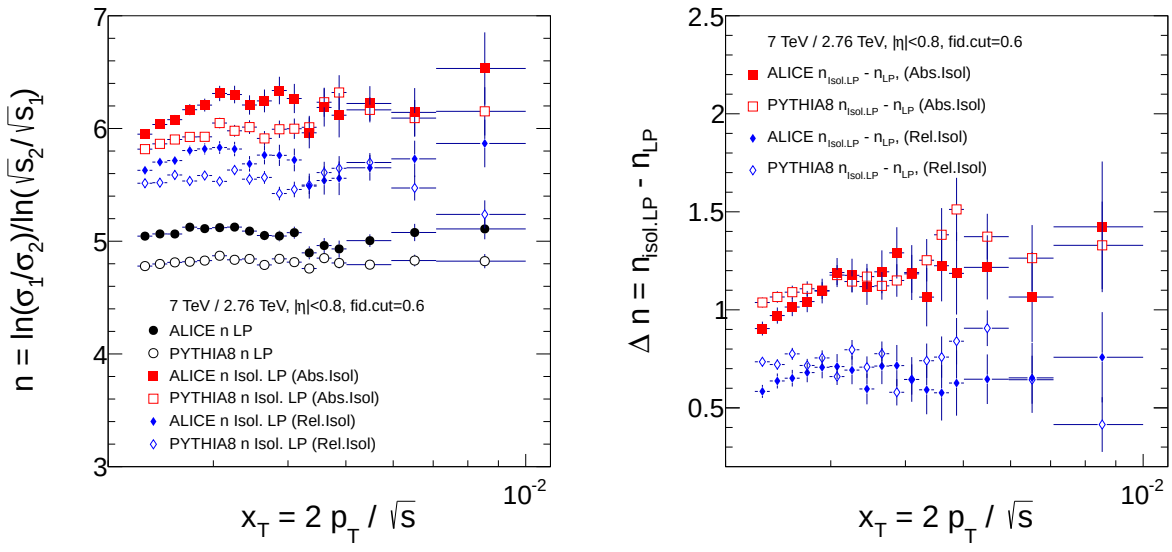

(a) Exponent n compilation

(b) $\Delta n = n_{\mathrm{isol.LP}} - n_{\mathrm{LP}}$

Figure 24: Scaling exponent n (left) and the difference between n for isolated LP and LP (right) for ALICE and PYTHIA8 7 TeV / 2.76 TeV with absolute and relative isolation.

5.2 Toy Monte Carlo model of parton cascade

It is perhaps surprising that the isolation increased $\langle n \rangle$ also in the case of PYTHIA. Since the HT processes are not fully implemented in PYTHIA [50], one would have expected the exponent of isolated particles to be similar as in the inclusive case. Furthermore, the result in a PYTHIA study [60] was that the increase became larger when the isolation criteria was

tightened.

One way to gain further understanding of these effects was to study a toy Monte Carlo simulation of parton cascade. The goal was to see if the rise of n was caused just by the kinematics followed by the isolation requirement even without any higher twist processes. The idea of the cascade process is that hadron momenta are sampled from an initial parton p_{T} using a "fragmentation function", until the parton p_{T} becomes smaller than some user-defined threshold. One cannot produce "real" inclusive spectra with this method, but this provides a simple framework to study kinematics via Monte Carlo.

The cascade process began when the initial parton momentum was sampled from a power distribution

$$\frac{1}{p_{\mathrm{Tq}}}\frac{\mathrm{d}N}{\mathrm{d}p_{\mathrm{Tq}}} \sim \frac{1}{p_{\mathrm{Tq}}^{n}}, \tag{30}$$

where $p_{\mathrm{Tq}} \in [1.5, 100]\,\mathrm{GeV/c}$ and $n = n_1 = 5$ and $n = n_2 = 6$ to mimick the behaviour of pp data at $\sqrt{s}_1 = 7$ TeV and $\sqrt{s}_2 =$2.76 TeV, respectively. Then, the fragmentation variable z was repeatedly sampled from a fragmentation function

$$D(z) \sim e^{-8.2\cdot z}, \tag{31}$$

where $z \in [0, 1]$, and used to calculate the p_{T} of the hadron, p_{Th}, as

$$p_{\mathrm{Th}} = z \cdot p_{\mathrm{Tq}}. \tag{32}$$

The hadron p_{T} (and x_{T}) was filled into a histogram, and the hadron p_{T} was subtracted from the parton p_{T}. Hadron momenta were calculated and subtracted from the parton momentum by sampling new values of z, until the parton momentum became smaller than a pre-defined threshold, which was set to 0.5 GeV/c. After the cascade, the leading hadron could be found and checked whether it is isolated or not by calculating the p_{T} sum of all the other hadrons created in the cascade event.

The ratio of p_{T} yields for isolated leading particles divided by leading particles can be seen

in Fig 25. The absolute isolation was used for black points ($\sqrt{s} = 7$ TeV) and red points ($\sqrt{s} = 2.76$ TeV), and relative isolation for green squares ($\sqrt{s} = 7$ TeV) and blue squares ($\sqrt{s} = 2.76$ TeV).

One can see that the fraction of isolated particles is larger for the absolute cut at $p_{\mathrm{T}} < 5$ GeV/c, as in that region it allows larger background activity than the relative case (10% of p_{Tt}). At $p_{\mathrm{T}} > 5$ GeV/c, there are more isolated particles with relative than with the absolute criterion. With the relative isolation criterion, the ratio stays approximately constant over the whole p_{T} range, as the criterion scales linearly with p_{T}.

Since the ratio of isolated leading particles to all leading particles is a constant with the relative cut, it follows that isolation did not change the steepness of the p_{T} distribution. However, from the constant ratios one can estimate what is the difference of n for isolated leading particles to all leading particles, using (7). It is now assumed that if σ_1 is the invariant cross section for leading particles at $\sqrt{s}_1 = 2.76$ TeV, then for isolated leading particles with relative cut it is $c_1\sigma_1$, where $c_1 = 0.04777 \pm 0.00009$, the fraction obtained by fitting a constant to blue points in Fig. (25). The same can be done for 7 TeV by fitting the green points, where the constant is $c_2 = 0.02568 \pm 0.00004$. Now the difference in n would be

$$\begin{aligned} \Delta n_{\mathrm{toyMC,rel.}} &= n_{\mathrm{isol.LP}} - n_{\mathrm{LP}} \\ &= \frac{\ln(c_1\sigma_1/c_2\sigma_2)}{\ln(\sqrt{s}_2/\sqrt{s}_1)} - \frac{\ln(\sigma_1/\sigma_2)}{\ln(\sqrt{s}_2/\sqrt{s}_1)} \\ &= \frac{\ln(c_1/c_2)}{\ln(\sqrt{s}_2/\sqrt{s}_1)} \\ &= 0.662, \end{aligned} \tag{33}$$

which means that there can be a non-zero Δn coming just from the different fractions of isolated particles with different $\sqrt{s}$, even though the slopes were unchanged. Of course the constants c can be generalized to functions depending on x_{T}, as $c_1(x_{\mathrm{T}})$ and $c_2(x_{\mathrm{T}})$, if the slopes are not constant.

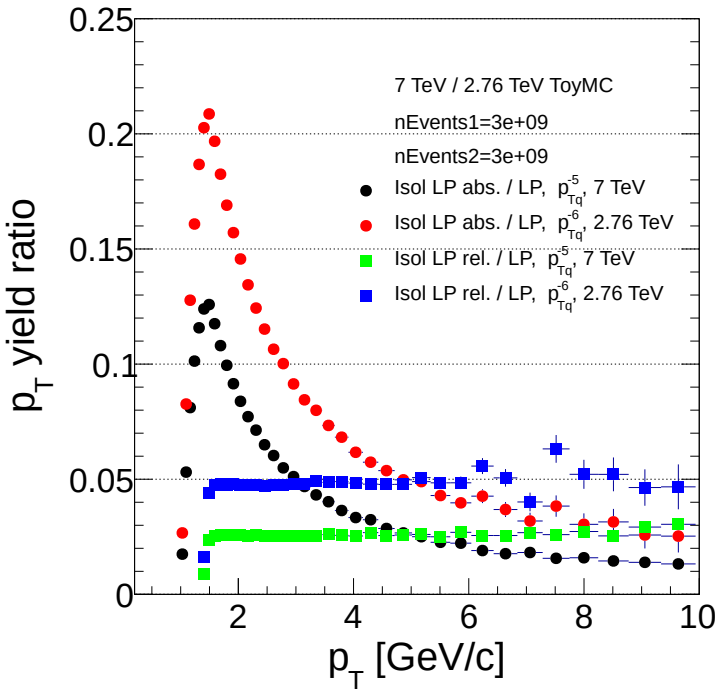

Figure 25: The ratio of p_{T} yields of isolated leading particles to all leading particles in toy MC model for absolute isolation criteria and relative isolation criteria at $\sqrt{s} = 7$ TeV (p_{Tq}^{-5}) and 2.76 TeV (p_{Tq}^{-6}).

To gain further understanding of how the steepness of the parton momentum distribution affects the isolation probability, an additional study of parton p_{T} spectra was carried out. Specifically, it was studied how the parent parton p_{T} distributions for a leading hadron between 7 and 8 GeV/c, with and without the isolation condition, depended on $\sqrt{s}$. In Fig. 26, one can see the parton distributions for all leading hadrons (green circles), for isolated leading hadrons with absolute criteria (blue circles) and for isolated leading hadrons with relative criteria (magenta circles). The left panel is for $\sqrt{s} = 2.76$ TeV or p_{Tq}^{-6} and the right panel for $\sqrt{s} = 7$ TeV or p_{Tq}^{-5}.

For 7 TeV, the ratio of integrals of parton p_{T} distribution of isolated hadrons with relative cut (magenta circles) to all leading partons (green circles) is 0.041 ± 0.002, whereas for 2.76 TeV the ratio is 0.070 ± 0.004. This indicates that the relative difference between parton distributions for isolated leading particles to all leading particles depends on $\sqrt{s}$. Therefore,

the probability to produce an isolated leading particle varies with $\sqrt{s}$, as could be seen in the ratio plots in Fig. 25.

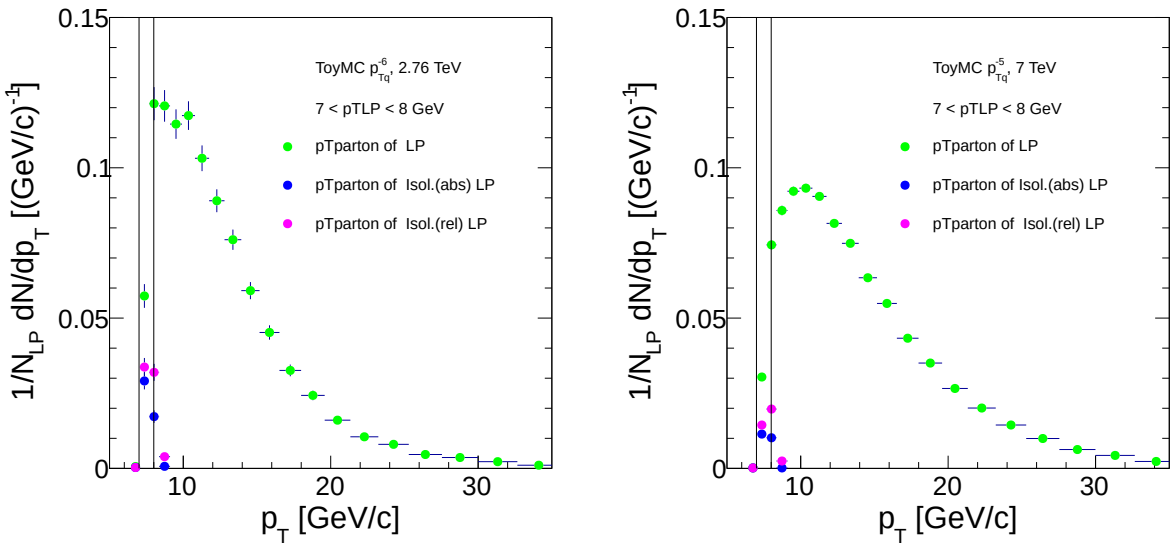

(a) $\sqrt{s} = 2.76$ TeV or p_{Tq}^{-6} (b) $\sqrt{s} = 7$ TeV or p_{Tq}^{-5}

Figure 26: Toy MC result for p_{Tq} distribution of partons that fragmented into a leading particle with $7 < p_{\mathrm{T}} < 8$ GeV/c, at $\sqrt{s} = 2.76$ TeV or p_{Tq}^{-6} (left) and at $\sqrt{s} = 7$ TeV or p_{Tq}^{-5} (right). Absolute isolation criteria 0.5 GeV/c and relative isolation criteria 10% of p_{T} were used. The vertical lines are indicating the borders of the studied p_{T} bin.

The mean z distributions as a function of p_{T} from toy MC can be seen in Fig. 27 for leading hadrons (green circles), isolated leading hadrons with absolute criteria (blue circles) and isolated leading hadrons with relative isolation criteria (magenta circles). The left plot is for $\sqrt{s} = 2.76$ TeV or p_{Tq}^{-6} and the right plot for $\sqrt{s} = 7$ TeV or p_{Tq}^{-5}. Isolated leading particles clearly have larger $\langle z \rangle$ than all leading particles. It can be seen that the $\langle z \rangle$ for all leading particles is slightly higher for $\sqrt{s} = 2.76$, for which the parton momentum distribution is steeper, than for the less steep $\sqrt{s} = 7$. For isolated leading particles, the $\langle z \rangle$ curves are very similar in height and shape. The crossover at $p_{\mathrm{T}} = 5$ GeV/c, where the two isolation criteria are equally strict, is clearly visible in Fig. 27.

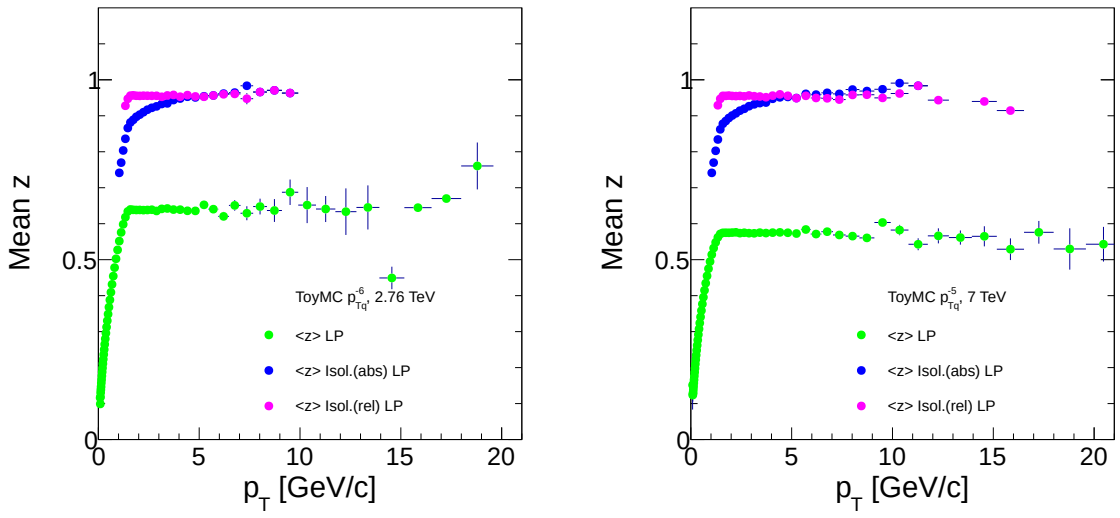

(a) $\sqrt{s} = 2.76$ TeV or p_{Tq}^{-6} (b) $\sqrt{s} = 7$ TeV or p_{Tq}^{-5}

Figure 27: Toy MC result for $\langle z \rangle$ as a function of p_{T} at $\sqrt{s} = 2.76$ TeV or p_{Tq}^{-6} (left) and $\sqrt{s} = 7$ TeV or p_{Tq}^{-5} (right). Absolute isolation criteria 0.5 GeV/c and relative isolation criteria 10% of p_{T} were used. The parton p_{Tq} was between 1.5 and 100 GeV/c.

In addition to p_{T}, also the x_{T} of hadrons were saved from the events. The x_{T} spectra were normalized to invariant cross sections the same way as real data, even though in the toy model case the normalization should not be taken too literally. However, when one studies Δn, the normalization should not matter. Now the exponent n could be calculated with (7) as before.

In Fig. 28 (a) the "invariant cross section from toy MC calculation" scaled by $\sqrt{s}^{\langle n \rangle}$ is shown. The markers are red circles for leading particles at $\sqrt{s}$ =7 TeV and green squares for leading particles at $\sqrt{s} = 2.76$ TeV. For isolated leading particles at $\sqrt{s} = 7$ TeV with the absolute isolation cut, the markers are blue triangles, and at $\sqrt{s}$ =2.76 TeV violet triangles . Similarily for the relative isolation cut, the markers are red hollow circles at $\sqrt{s}$ =7 TeV and black hollow circles at $\sqrt{s}$ =2.76 TeV. The x_{T} scaling seems not to be present in this toy model, because the slopes are different for spectra with different "$\sqrt{s}$".

In Fig 28 (b) the exponent n calculated from the toy MC data is presented. Markers are for inclusive hadrons (blue triangles), hadrons without cascade i.e. only the first hadrons

in event (violet triangles), leading particles (black circles), isolated leading particles with absolute cut (red circles) and isolated leading particles with relative cut (green circles). One can see that the values for the absolute isolation cut are larger than for the relative cut.

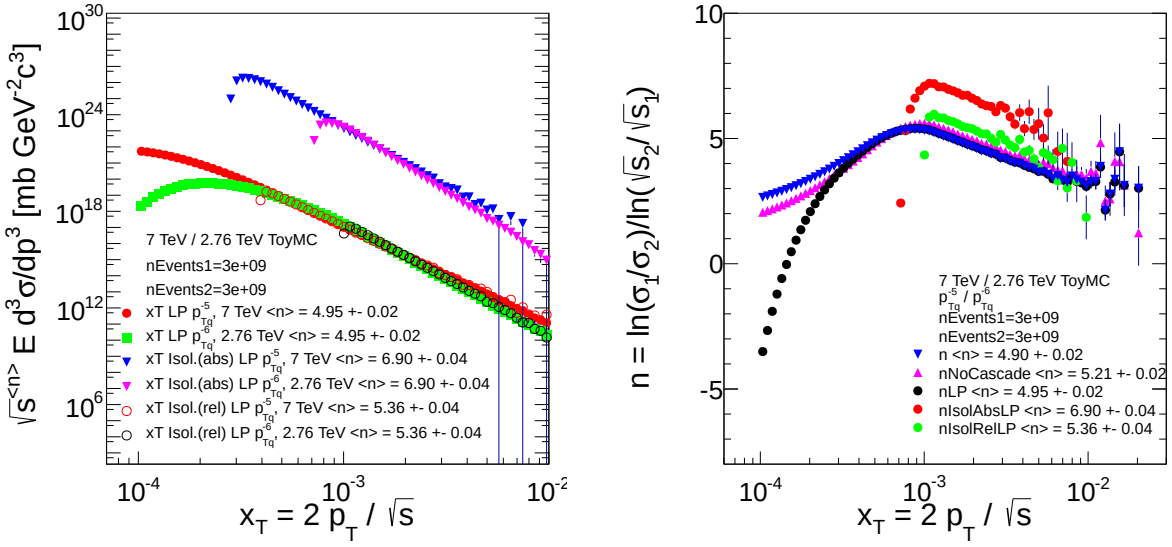

(a) Scaled inv. cross section vs. x_{T}

(b) n

Figure 28: Left: Invariant cross section scaled by $\sqrt{s}^{\langle n \rangle}$. Right: Compilation of n . Toy MC at $\sqrt{s} = 7$ TeV (p_{Tq}^{-5}) and 2.76 TeV (p_{Tq}^{-6}). Trigger type "No cascade" means that only the first hadron p_{T} from the cascade was filled. The units of the cross section should not be taken too literally in toy model case. However, the normalization was done as similarily as possible as to the real data.

The difference $\Delta n = n_{\mathrm{isol.LP}} - n_{\mathrm{LP}}$ for absolute and relative isolation criteria is shown in Fig. 29 for data and PYTHIA on the left panel (repeated from right panel of 24) and for toy Monte Carlo model on the right panel. It can be seen that the increase of $\langle n \rangle$ for absolute isolation is much larger than in the case of relative isolation, when compared to the n of all leading particles.

For the relative isolation cut, the difference Δn in the toy MC case is about 0.6689 ± 0.013 obtained by fitting a constant, quite close with values obtained from data and PYTHIA. Furthermore, it is close to the value 0.662 predicted by (33). However, the Δn with absolute

isolation was larger in the toy MC case, roughly 1.9, whereas in the case of data and PYTHIA the difference was only about 1.2.

The Δn was somewhat sensitive to the powers of the quark momentum spectra, which were chosen as $n_1 = -5$ and $n_2 = -6$. More realistic powers were obtained by fitting the inclusive p_{T} spectra (black points in Fig. 17 (a) and (c)) of real data at high p_{T} with a power-law function. Using values $n_1 = -6.12$ and $n_2 = -5.69$ obtained from the fit, the Δn decreased roughly to 1.5 for absolute isolation and to 0.2 for relative isolation.

The difference between the exponential fragmentation function used in this toy model and more realistic fragmentation function (in [61]) is largest at the extreme low and high z parts of the fragmentation function. It might be that the absolute isolation cut is more sensitive to non-exponential parts of the fragmentation function than the relative cut, since the allowed background activity does not scale with the particle p_{T}. When a more realistic shape for fragmentation function [61]

$$D(z) \propto z^{-0.32}\,(1-z)^{0.72}\,(1+z)^{-10.65} \tag{34}$$

was used in the toy model instead of the exponential function, the Δn were 0.8 for relative cut and 2.6 for absolute cut. This shows that the absolute cut is more sensitive than relative cut to the shape of the fragmentation function. One should, therefore, favour the relative cut in the analysis to minimize the systematic effects.

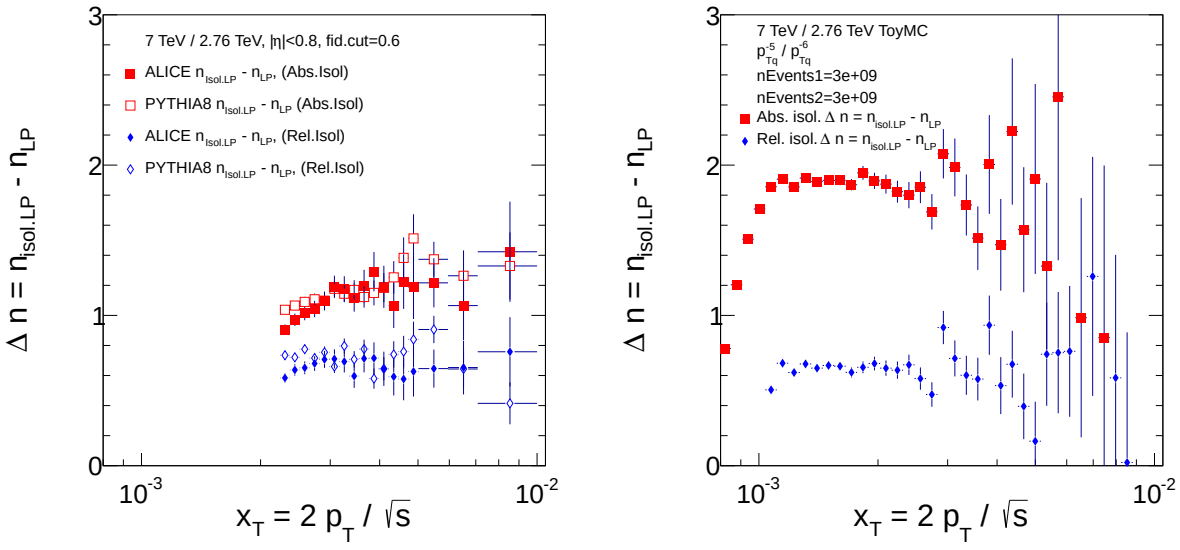

(a) Data and PYTHIA $\Delta n = n_{\text{isol.LP}} - n_{\text{LP}}$

(b) Toy MC $\Delta n = n_{\text{isol.LP}} - n_{\text{LP}}$

Figure 29: The difference between n for isolated LP and LP side by side for ALICE and PYTHIA8 (left) and for toy Monte Carlo model (right) at $\sqrt{s}$ =7 TeV / 2.76 TeV with absolute and relative isolation.

The shape of the hadron spectrum, and therefore the shape of n in Fig. 28 (b), can be calculated also analytically in the "no cascade" case, as in violet triangles in Fig. 28 . "No cascade" means that only the first hadron p_{T} from the cascade was filled. To begin, it can be shown that the final hadron spectrum shape $1/p_{\text{Th}}\,\mathrm{d}N/\mathrm{d}p_{\text{Th}}$ has the same p_{T}^{-n} power-law form as the parton spectrum $1/p_{\text{Tq}}\,\mathrm{d}N/\mathrm{d}p_{\text{Tq}}$. This result is called "the parent-child relationship", presented originally in [62]. If one starts from the number distribution of hadrons with $p_{\text{T}} = p_{\text{Th}} = z \cdot p_{\text{Tq}}$, written as

$$\frac{\mathrm{d}N}{\mathrm{d}p_{\text{Tq}}\mathrm{d}z} = \frac{\mathrm{d}N}{\mathrm{d}p_{\text{Tq}}} \times D(z), \tag{35}$$

one can extract, using $p_{\text{Th}} = z \cdot p_{\text{Tq}}$ and $\mathrm{d}p_{\text{Tq}} = \mathrm{d}p_{\text{Th}}/z$, the hadron spectrum as an integral

$$\frac{\mathrm{d}N}{\mathrm{d}p_{\text{Th}}} = \int_{z,\text{min}}^{z,\text{max}} \frac{1}{z}\frac{\mathrm{d}N}{\mathrm{d}p_{\text{Tq}}} D(z)\mathrm{d}z. \tag{36}$$

The integration limits of z are $2p_{\text{T}}/\sqrt{s}$ for the minimum and 1 for the maximum. If the

parton spectrum had the form

$$\frac{1}{p_{\mathrm{Tq}}}\frac{\mathrm{d}N}{\mathrm{d}p_{\mathrm{Tq}}} = \frac{1}{p_{\mathrm{Tq}}^{n}}, \tag{37}$$

we get the hadron spectrum's p_{T} dependence by substituting (37) into (36)

$$\frac{1}{p_{\mathrm{Tq}}}\frac{\mathrm{d}N}{\mathrm{d}p_{\mathrm{Th}}} = \frac{1}{p_{\mathrm{Th}}^{n}}\int_{x_{\mathrm{T}}}^{1} z^{n-2}D(z)\mathrm{d}z, \tag{38}$$

where the integral is weakly dependent on p_{T}, since the value of x_{T} is small.

To calculate the slope of n, the following form was assumed for invariant cross section using (38) and denoting p_{Th} as p_{T} from now on,

$$\sigma^{\mathrm{inv}}(x_{\mathrm{T}},\sqrt{s}_1) = \frac{\sigma^{\mathrm{inel},\sqrt{s}_1}}{N_{\mathrm{evnt1}}}\frac{1}{p_{\mathrm{T}}}\frac{\mathrm{d}N}{\mathrm{d}p_{\mathrm{T}}} = \frac{\sigma^{\mathrm{inel},\sqrt{s}_1}}{N_{\mathrm{evnt1}}}\underbrace{\left(\frac{\sqrt{s}_1 x_{\mathrm{T}}}{2}\right)^{-n_1}}_{p_{\mathrm{T}}^{-n_1}}\int_{x_{\mathrm{T}}}^{1} z^{n_1-2}D(z)\mathrm{d}z, \tag{39}$$

where n_1 is the power of the invariant quark spectra $\frac{dN}{dp_{\mathrm{Tq}}}$ for given $\sqrt{s}_1$, and N_{evnt1} is the number of events for normalization.

If the integral in the cross section (39) is assumed constant for both cases ($n = 5$ and $n = 6$), it can be substituted into the formula of the effective exponent (7). One then obtains a form

$$n(x_{\mathrm{T}},\sqrt{s}_1,\sqrt{s}_2) = \mathrm{constant} + \underbrace{\frac{n_2 - n_1}{\ln(\sqrt{s}_2/\sqrt{s}_1)}}_{\mathrm{slope}}\ln(x_{\mathrm{T}}). \tag{40}$$

The slope of the function (40) calculated using the toy model parameters is -1.07. When fitting a function of a form $A + B\ln(x_{\mathrm{T}})$, where A and B were constants, to "no cascade" toy MC n curve, the slope B obtained was -1.02 ± 0.5. This agreement is accurate within error bars, which suggests that the behaviour of the model and the results were well understood. This further encouraged to use the toy MC results for conclusions in this study, since the model is completely free from any higher-twist effects.

From the results of the toy MC study in Figures 27 and 29, it seems that the increase of n can largely be explained by the kinematics following the isolation cut. Even though the

only ingredients of this simple model were the power-law parton distribution and exponential fragmentation function, the results were quite similar to the ones seen with real data and PYTHIA in 29.

6 Conclusions

A study of isolated particles and their x_{T} distributions for charged hadrons measured in pp collision at $\sqrt{s} = 7$ TeV and 2.76 TeV by the ALICE collaboration was carried out. The suggestion by Arleo et al. in [3], that triggering on isolated particles would enhance the higher-twist contributions and therefore increase the scaling index n, was the motivation for the study of systematic effects resulting from the isolation cut. Two isolation criteria were studied, both in a cone of radius $R = 0.4$. First was the absolute isolation of 0.5 GeV/c background limit and the second was the relative isolation that allowed 10 % of the trigger p_{T} activity in the background.

Indeed, it was seen that applying the isolation cut increased n in real data measured by the ALICE collaboration, as well as in PYTHIA8, with both isolation criteria. The PYTHIA Physics manual [50] states that higher-twist related formulas have not been fully incorporated in PYTHIA. However, parametrization such as pion form factors are implemented, which may explain part of the results. However, the information about HT processes in PYTHIA was too limited for stronger conclusions.

A simple toy Monte Carlo model was studied to gain further understanding of the Δn result. The ingredients of the toy model study were the power law parton momentum distribution and the exponential fragmentation function (FF). This kind of controlled scenario was necessary to rule out the effects of higher-twist phenomena or any other processes which may be found in real data that would contribute to the increase of the exponent n. Even in this simple case, the rising of n with isolation was observed by roughly the same amount as in the real data and PYTHIA.

With the toy model, the increase of n could largely be explained by a kinematic bias resulting from the isolation itself. As demonstrated by the toy model, the bias is a result from folding of the parton momentum distribution and the FF. This is seen in Fig. 26, which shows the distributions of parent partons that fragmented into leading and isolated leading hadrons with $7 < p_{\mathrm{T}} < 8$ GeV/c. For $\sqrt{s} = 2.76$ TeV the leading parton spectrum was narrower than

for $\sqrt{s} = 7$. The FF was the same, but the steepness of the parton momentum distribution was different, which resulted in different probability to produce an isolated leading particle with different $\sqrt{s}$. These effects were enough to produce Δn of the similar order as in the real data. It was also observed that the Δn was larger with the absolute cut than with the relative cut. In order to minimize the kinematic bias, one would then prefer the relative cut in the analysis.

From the mean perpendicular cone p_{T} sums in, e.g., Fig. 20 (b) and (d), one can see that PYTHIA8 with the default tune underestimated the Underlying Event activity by approximately 20 %, which is in agreement with observations in [16]. The isolated leading hadrons also had smaller UE activity than all the leading hadrons on average, indicating another systematic effect related to isolation cut.

To study the higher-twist phenomena in the real data using an isolation cut, one would need to separate the HT signal from the kinematic bias caused by the isolation criteria. It would require a calculation of the magnitude of the kinematic bias by using more realistic model than the toy model used in this thesis. If this could be done reliably enough, one could subtract the kinematic effect from the n and study the HT signal.

Appendix

A Efficiency curves for 2.76 TeV

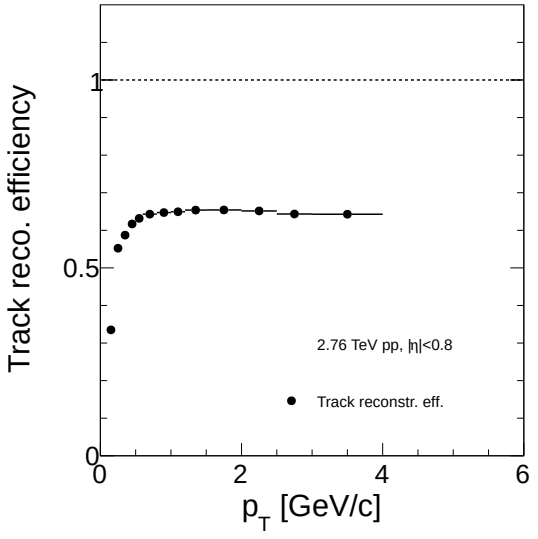

(a) Track reconstruction efficiency

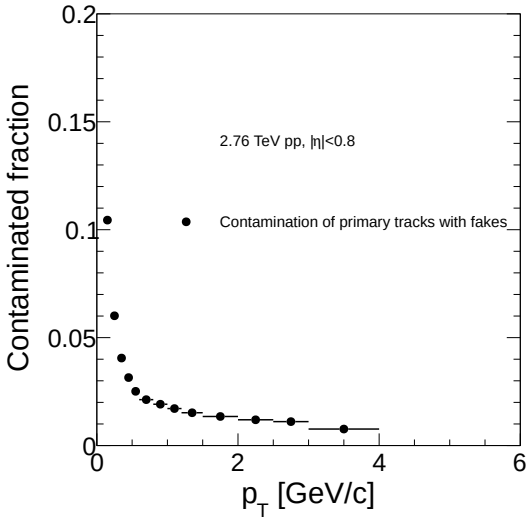

(b) Contamination of the reconstructed primaries with fake tracks

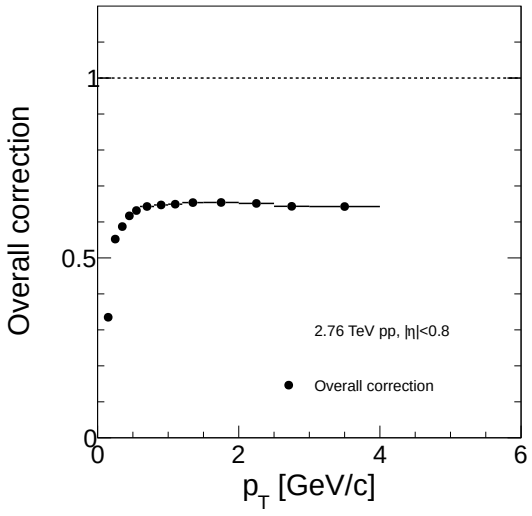

(c) Overall correction

Figure 30: Track reconstruction efficiency (a), contamination (b) and overall correction (c) as a function of p_{T} for $\sqrt{s}$ =2.76 TeV data [52].

B p_{T} distributions in cones

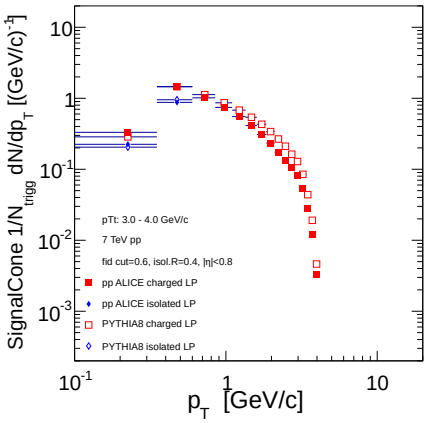

(a) $3 < p_{\mathrm{Tt}} < 4$ GeV/c

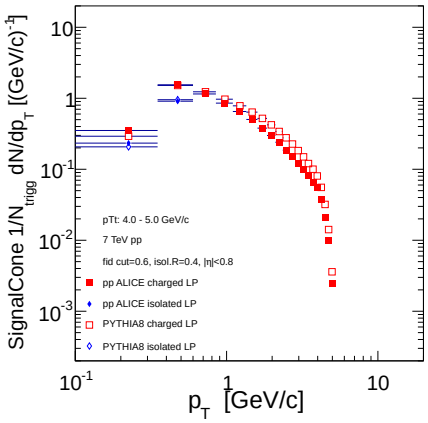

(b) $4 < p_{\mathrm{Tt}} < 5$ GeV/c

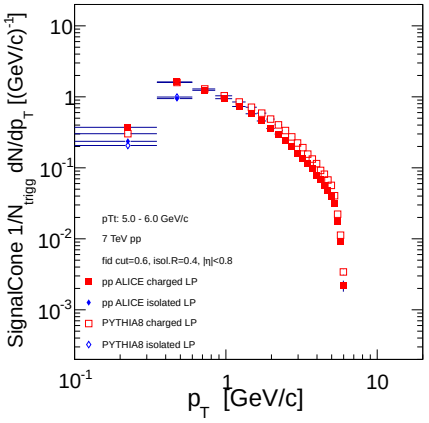

(c) $5 < p_{\mathrm{Tt}} < 6$ GeV/c

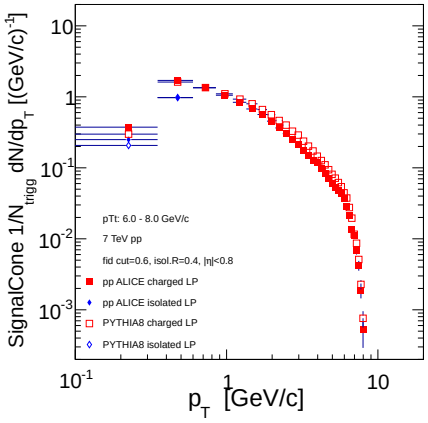

(d) $6 < p_{\mathrm{Tt}} < 8$ GeV/c

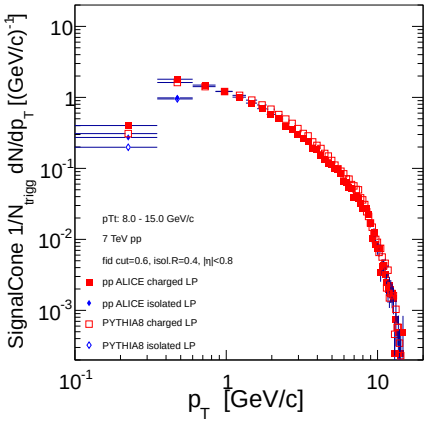

(e) $8 < p_{\mathrm{Tt}} < 15$ GeV/c

Figure 31: p_{T} distribution in signal cone for different trigger p_{T} bins, pp at $\sqrt{s} = 7\,\mathrm{TeV}$. Hollow markers are for PYTHIA and filled markers for ALICE data.

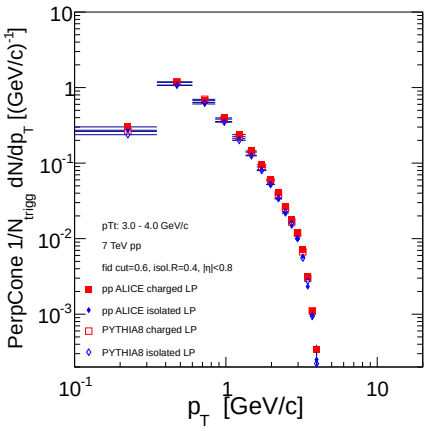

(a) $3 < p_{\mathrm{Tt}} < 4$ GeV/c

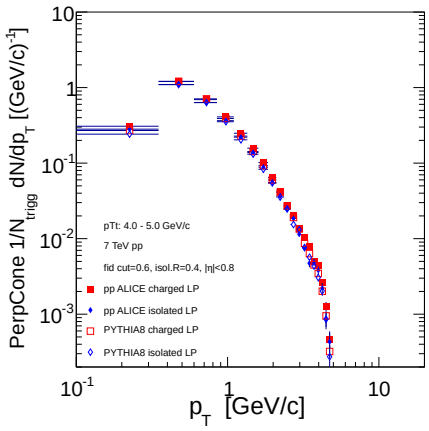

(b) $4 < p_{\mathrm{Tt}} < 5$ GeV/c

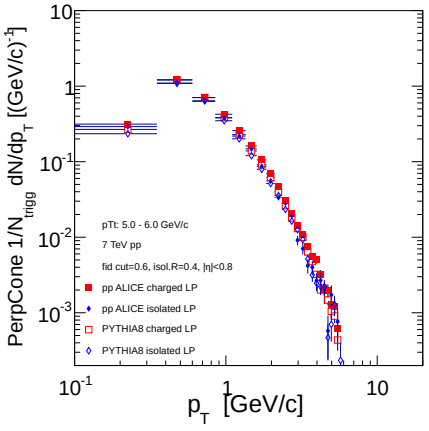

(c) $5 < p_{\mathrm{Tt}} < 6$ GeV/c

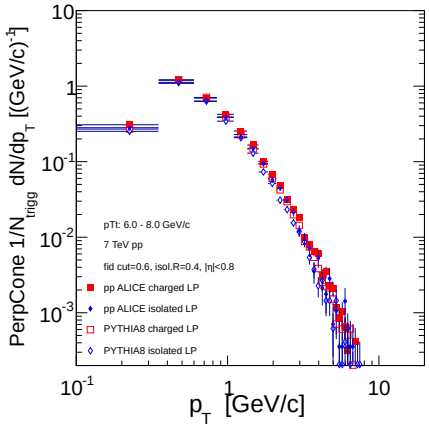

(d) $6 < p_{\mathrm{Tt}} < 8$ GeV/c

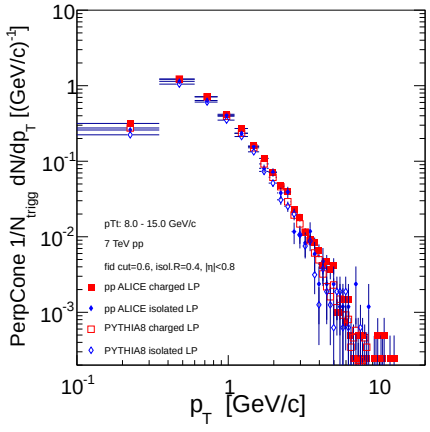

(e) $8 < p_{\mathrm{Tt}} < 15$ GeV/c

Figure 32: p_{T} distribution in perpendicular cone for different trigger p_{T} bins, pp at $\sqrt{s} = 7\,\mathrm{TeV}$. Hollow markers are for PYTHIA and filled markers for ALICE data.

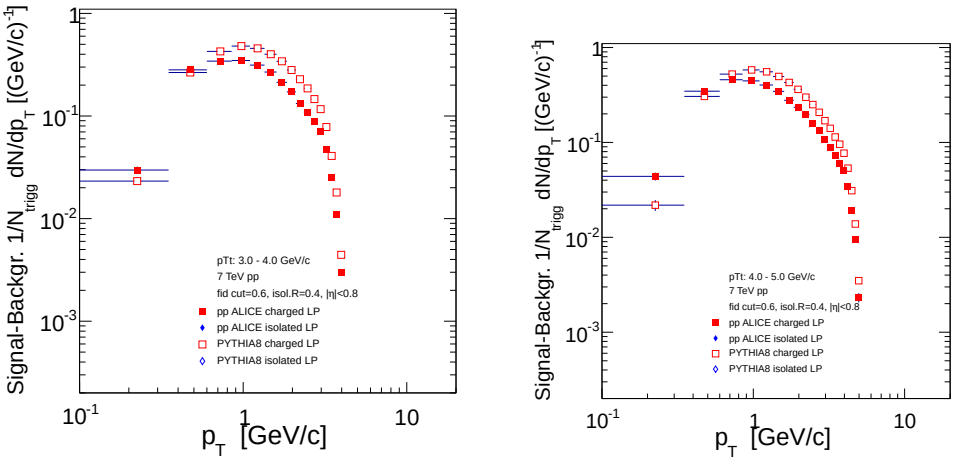

(a) $3 < p_{\mathrm{Tt}} < 4$ GeV/c (b) $4 < p_{\mathrm{Tt}} < 5$ GeV/c

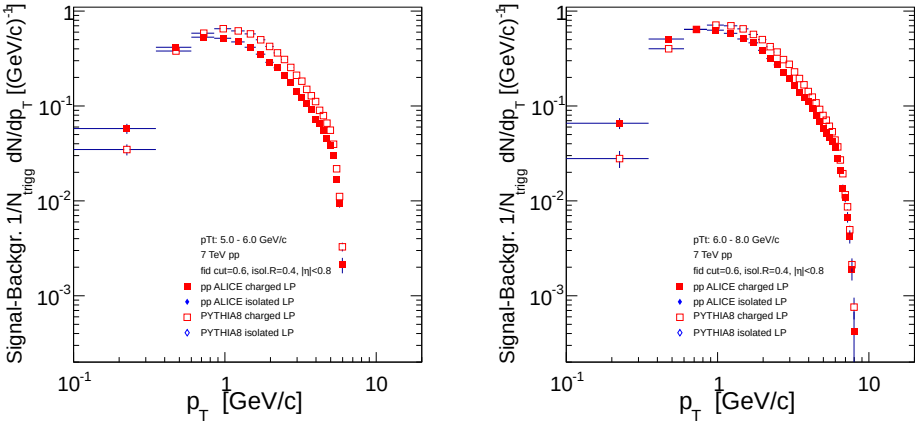

(c) $5 < p_{\mathrm{Tt}} < 6$ GeV/c (d) $6 < p_{\mathrm{Tt}} < 8$ GeV/c

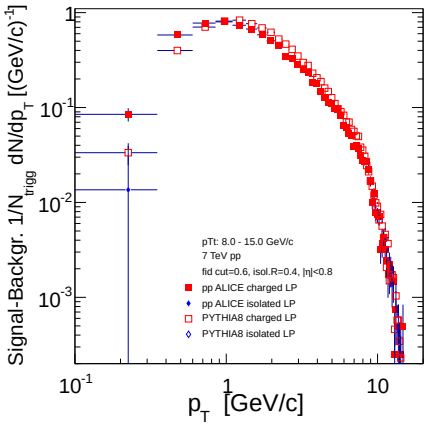

(e) $8 < p_{\mathrm{Tt}} < 15$ GeV/c

Figure 33: p_{T} distribution in signal cone with perpendicular cone distribution subtracted for different trigger p_{T} bins, pp at $\sqrt{s} = 7$ TeV. Hollow markers are for PYTHIA and filled markers for ALICE data.

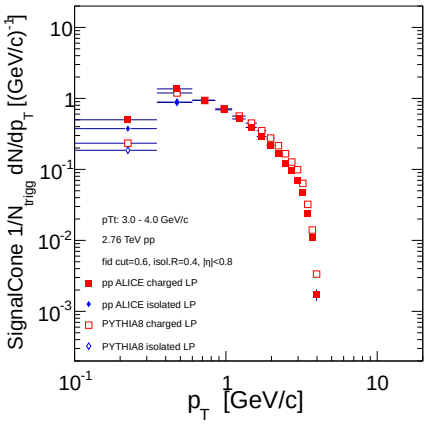

(a) $3 < p_{\mathrm{Tt}} < 4$ GeV/c

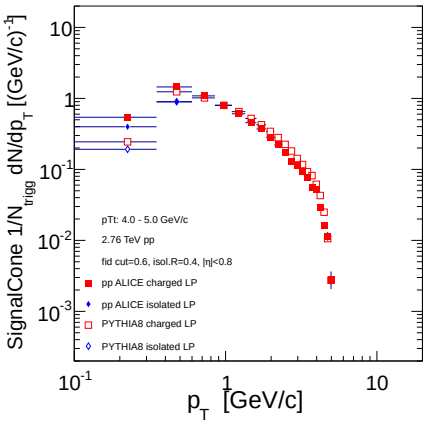

(b) $4 < p_{\mathrm{Tt}} < 5$ GeV/c

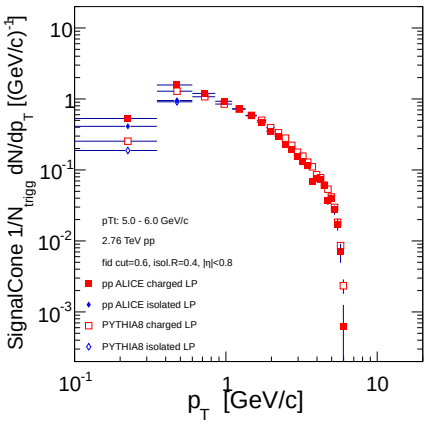

(c) $5 < p_{\mathrm{Tt}} < 6$ GeV/c

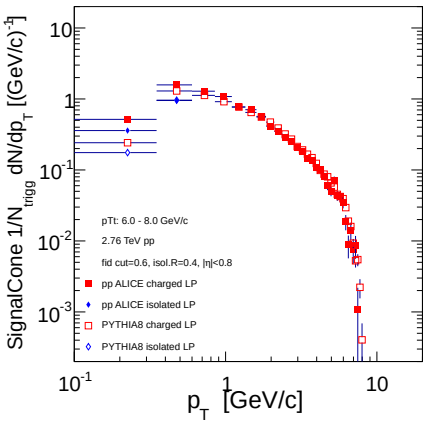

(d) $6 < p_{\mathrm{Tt}} < 8$ GeV/c

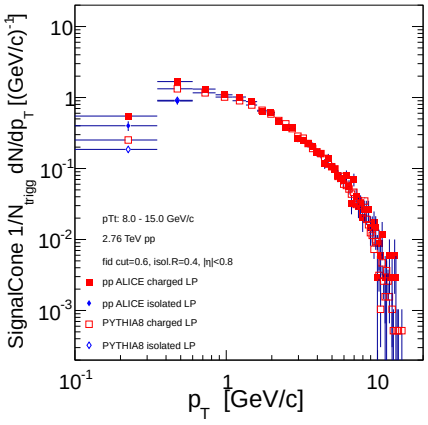

(e) $8 < p_{\mathrm{Tt}} < 15$ GeV/c

Figure 34: p_{T} distribution in signal cone for different trigger p_{T} bins, pp at $\sqrt{s} = 2.76\,\mathrm{TeV}$. Hollow markers are for PYTHIA and filled markers for ALICE data.

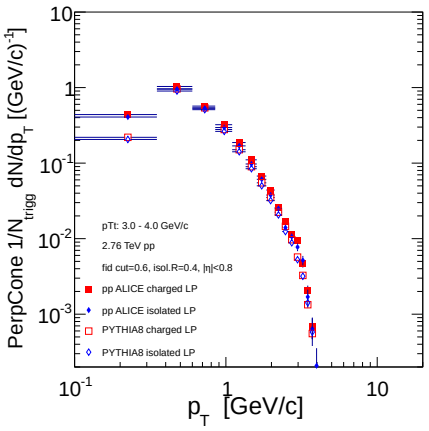

(a) $3 < p_{\mathrm{Tt}} < 4$ GeV/c

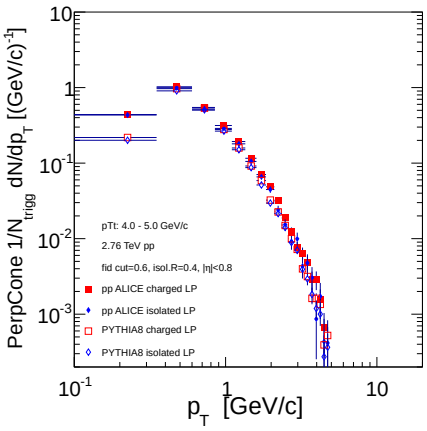

(b) $4 < p_{\mathrm{Tt}} < 5$ GeV/c

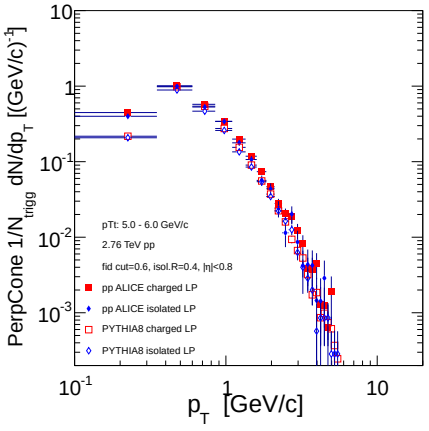

(c) $5 < p_{\mathrm{Tt}} < 6$ GeV/c

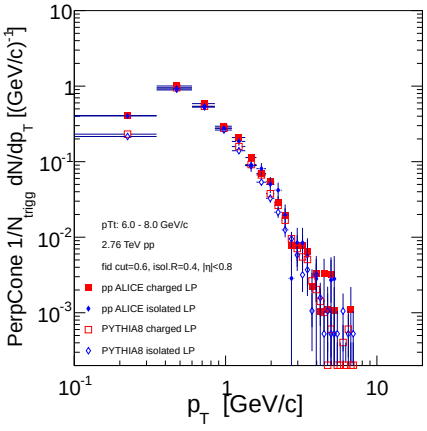

(d) $6 < p_{\mathrm{Tt}} < 8$ GeV/c

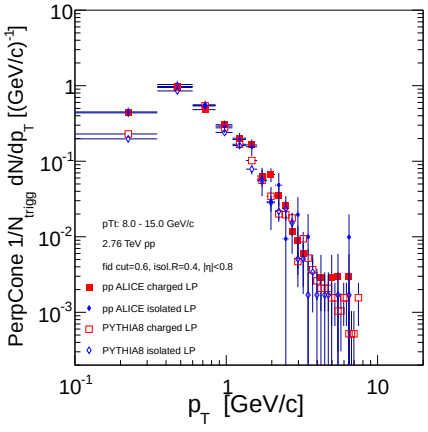

(e) $8 < p_{\mathrm{Tt}} < 15$ GeV/c

Figure 35: p_{T} distribution in perpendicular cone for different trigger p_{T} bins, pp at $\sqrt{s} = 2.76\,\mathrm{TeV}$. Hollow markers are for PYTHIA and filled markers for ALICE data.

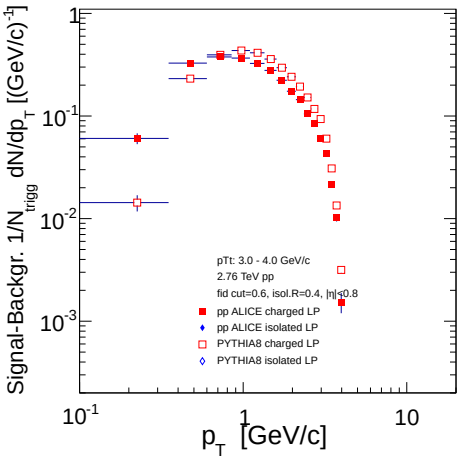

(a) $3 < p_{\mathrm{Tt}} < 4$ GeV/c

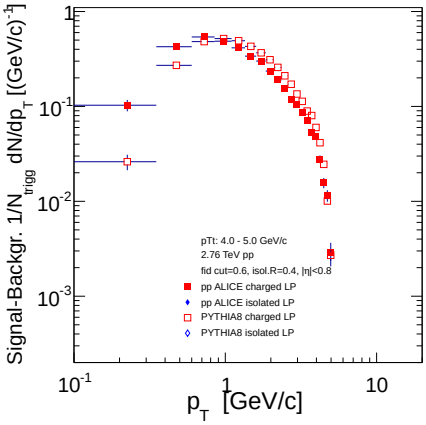

(b) $4 < p_{\mathrm{Tt}} < 5$ GeV/c

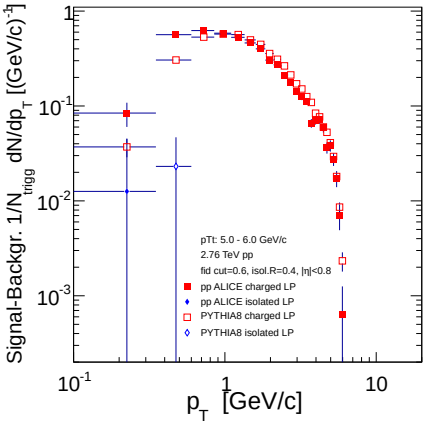

(c) $5 < p_{\mathrm{Tt}} < 6$ GeV/c

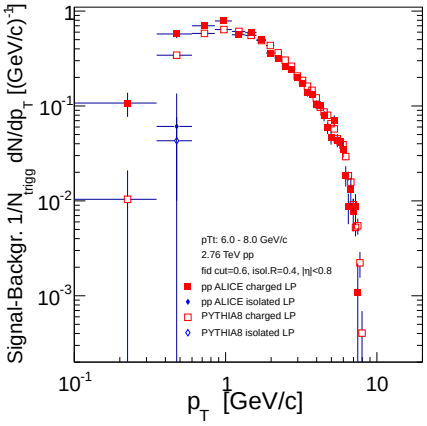

(d) $6 < p_{\mathrm{Tt}} < 8$ GeV/c

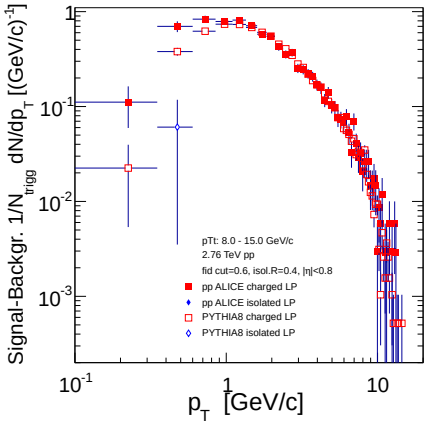

(e) S8 $< p_{\mathrm{Tt}} < 15$ GeV/c

Figure 36: p_{T} distribution in signal cone with perpendicular cone distribution subtracted for different trigger p_{T} bins, pp at $\sqrt{s} = 2.76\,\mathrm{TeV}$. Hollow markers are for PYTHIA and filled markers for ALICE data.

C x_{E} distributions vs. $p_{\mathrm{T,sum}}$

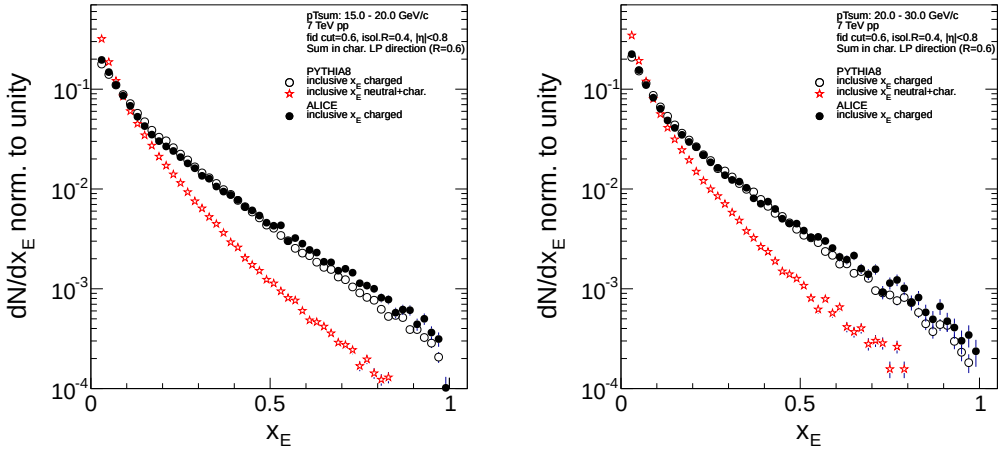

(a) $15 < p_{\mathrm{T,sum}} < 20$ GeV/c

(b) $20 < p_{\mathrm{T,sum}} < 30$ GeV/c

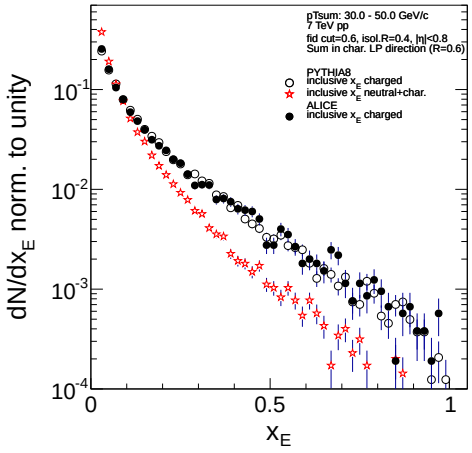

(c) $30 < p_{\mathrm{T,sum}} < 50$ GeV/c

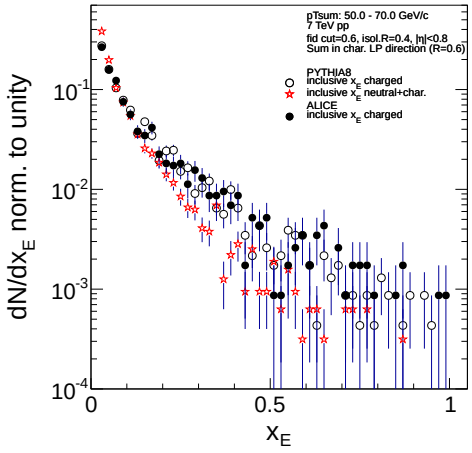

(d) $50 < p_{\mathrm{T,sum}} < 70$ GeV/c

Figure 37: Distributions of x_{E} for different $p_{T,sum}$ bins for inclusive hadrons for pp at $\sqrt{s} =$ 7 TeV. Hollow markers are for PYTHIA and filled markers for ALICE data. The absolute isolation cut with an isolation radius 0.4 was used.

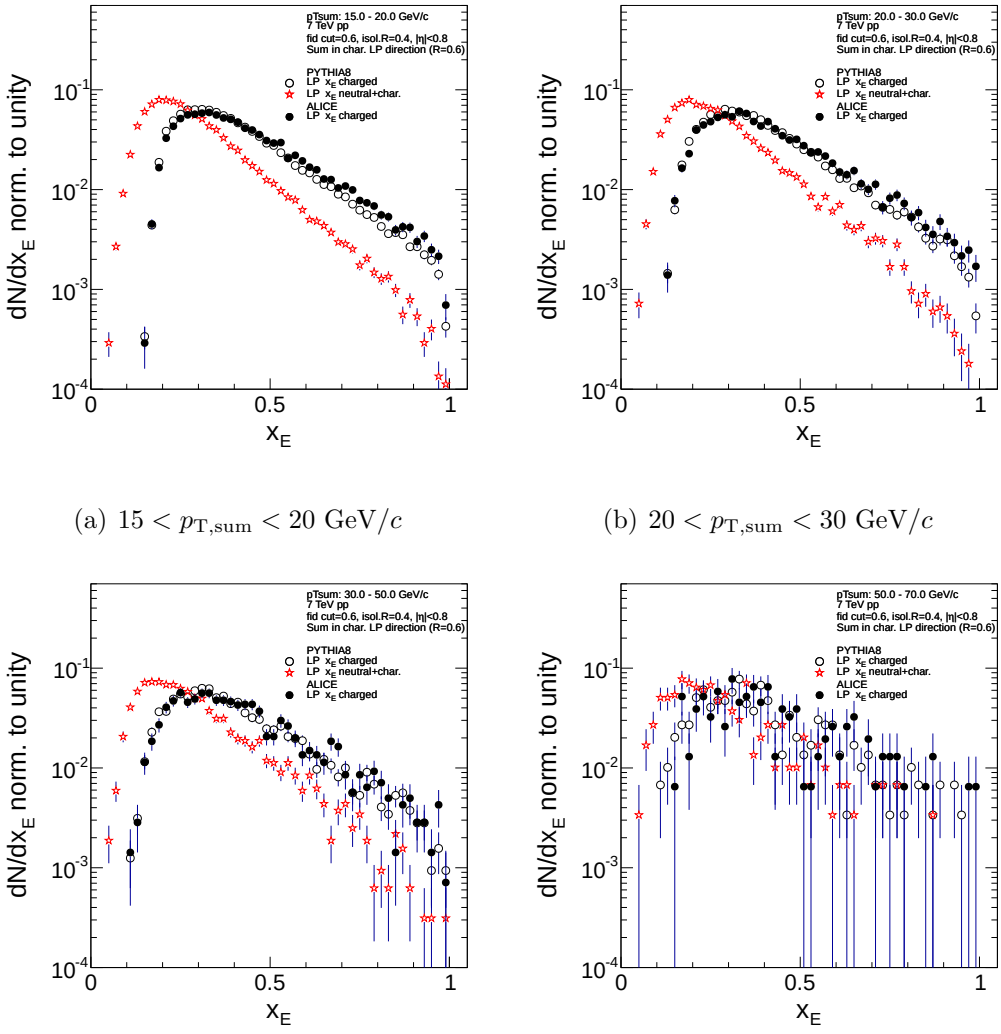

(a) $15 < p_{\mathrm{T,sum}} < 20$ GeV/c

(b) $20 < p_{\mathrm{T,sum}} < 30$ GeV/c

(c) $30 < p_{\mathrm{T,sum}} < 50$ GeV/c

(d) $50 < p_{\mathrm{T,sum}} < 70$ GeV/c

Figure 38: Distributions of x_{E} for different $p_{T,sum}$ bins for leading hadrons for pp at $\sqrt{s} =$ 7 TeV. Hollow markers are for PYTHIA and filled markers for ALICE data. The absolute isolation cut with an isolation radius 0.4 was used.

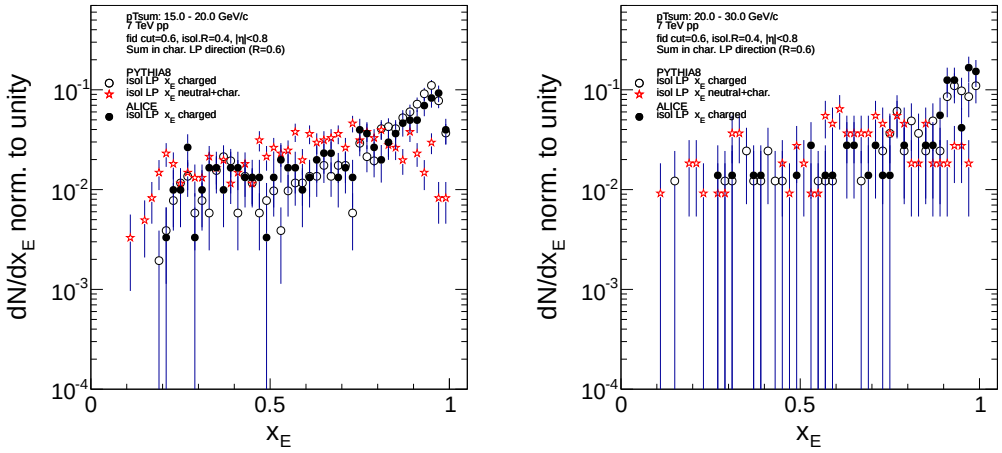

(a) $15 < p_{\mathrm{T,sum}} < 20$ GeV/c

(b) $20 < p_{\mathrm{T,sum}} < 30$ GeV/c

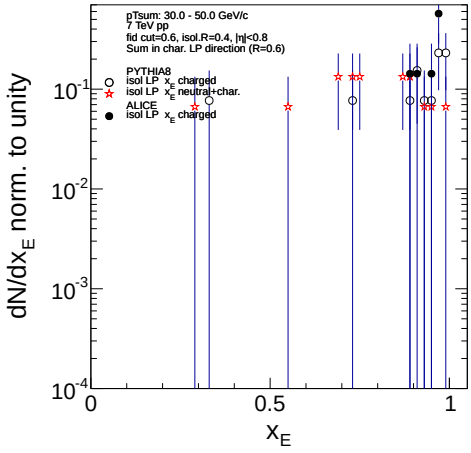

(c) $30 < p_{\mathrm{T,sum}} < 50$ GeV/c

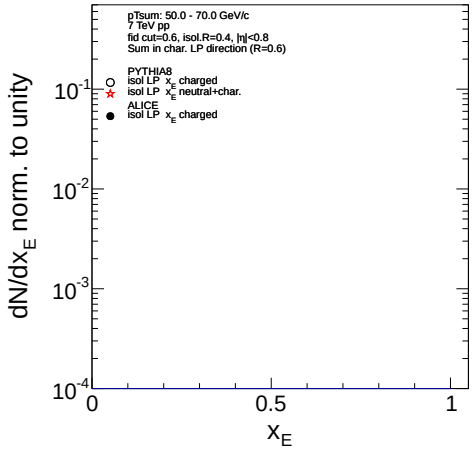

(d) $50 < p_{\mathrm{T,sum}} < 70$ GeV/c

Figure 39: Distributions of x_{E} for different $p_{T,sum}$ bins for isolated leading hadrons for pp at $\sqrt{s} = 7$ TeV. Hollow markers are for PYTHIA and filled markers for ALICE data. The absolute isolation cut with an isolation radius 0.4 was used.

References

[1] The ALICE Collaboration. The ALICE experiment at the CERN LHC. *Journal of Instrumentation*, 3(08):S08002, 2008.

[2] J.F Owens. Large-momentum-transfer production of direct photons, jets, and particles. *Rev. Mod. Phys.*, 59(2):465–503, 1987.

[3] Francois Arleo, Stanley J. Brodsky, Dae Sung Hwang, , and Anne M. Sickles. Higher-twist dynamics in large transverse momentum hadron production. *arXiv:0911.4604v2 [hep-ph]*.

[4] Richard Blankenbecler, Stanley J. Brodsky, and J.F. Gunion. Inclusive Processes at High Transverse Momentum. *Phys.Lett.*, B42:461, 1972.

[5] P.B. Martin and G. Shaw. *Particle Physics*. Manchester Physics Series. John Wiley & Sons, 2008.

[6] Jan Rak. Emerging picture of hard scattering phenomena in p + p collisions at in alice. *Nuclear Physics A*, 855(1):461 – 464, 2011. Proceedings of the 4th International Conference on Hard and Electromagnetic Probes of High-Energy Nuclear Collisions.

[7] M. Breidenbach, J. I. Friedman, H. W. Kendall, E. D. Bloom, D. H. Coward, H. DeStaebler, J. Drees, L. W. Mo, and R. E. Taylor. Observed behavior of highly inelastic electron-proton scattering. *Phys. Rev. Lett.*, 23:935–939, Oct 1969.

[8] J. D. Bjorken. Asymptotic sum rules at infinite momentum. *Phys. Rev.*, 179:1547–1553, Mar 1969.

[9] Richard P. Feynman. Very high-energy collisions of hadrons. *Phys. Rev. Lett.*, 23:1415–1417, Dec 1969.

[10] Perkins D. H. Cocconi G., Koester L. J. Technical report no. ucrl-10022, lawrence radiation laboratory. *Unpublished*, 1961.

[11] Jay Orear. Transverse momentum distribution of protons in $p - p$ elastic scattering. *Phys. Rev. Lett.*, 12:112–113, Jan 1964.

[12] F.W. Busser, L. Camilleri, L. di Lella, G. Gladding, A. Placci, et al. Observation of pi0 mesons with large transverse momentum in high-energy proton proton collisions. *Phys.Lett.*, B46:471–476, 1973.

[13] M. Banner, J.L. Hamel, J.P. Pansart, A.V. Stirling, J. Teiger, et al. Large transverse momentum particle production at 90 degrees in proton-p proton collisions at the ISR. *Phys.Lett.*, B44:537–540, 1973.

[14] B. Alper et al. Production of high transverse momentum particles in p p collisions in the central region at the CERN ISR. *Phys.Lett.*, B44:521–526, 1973.

[15] M.J. Tannenbaum. From the ISR to RHIC: Measurements of hard-scattering and jets using inclusive single particle production and 2-particle correlations. *J.Phys.Conf.Ser.*, 27:1–10, 2005.

[16] The ALICE Collaboration. Underlying Event measurements in pp collisions at $\sqrt{s} =$ 0.9 and 7 TeV with the ALICE experiment at the LHC. *JHEP*, 1207:116, 2012.

[17] CERN-Columbia-Oxford-Rockefeller (CCOR) Collaboration, A L S Angelis, B J Blumenfeld, L Camilleri, T J Chapin, R L Cool, C del Papa, L Di Lella, Z Dimcovski, R J Hollebeek, D Levinthal, L M Lederman, J T Linnemann, L Lyons, N Phinney, B G Pope, S H Pordes, A F Rothenberg, A M Segar, J Singh-Sidhu, A M Smith, M J Tannenbaum, R A Vidal, J Wallace-Hadrill, T O White, and J M Yelton. A study of final states containing high-p_{T} π's at the cern isr. *Physica Scripta*, 19(2):116, 1979.

[18] A. Adare et al. Inclusive cross-section and double helicity asymmetry for pi0 production in p + p collisions at s**(1/2) = 200-GeV: Implications for the polarized gluon distribution in the proton. *Phys.Rev.*, D76:051106, 2007.

[19] M. Gell-Mann. A schematic model of baryons and mesons. *Physics Letters*, 8(3):214 – 215, 1964.

[20] G. Zweig. An SU(3) model for strong interaction symmetry and its breaking. 1964.

[21] Harald Fritsch. The history of QCD. *CERN Cour.*, 52N8:21–24, 2012.

[22] V.E. Barnes, P.L. Connolly, D.J. Crennell, B.B. Culwick, W.C. Delaney, et al. Observation of a Hyperon with Strangeness -3. *Phys.Rev.Lett.*, 12:204–206, 1964.

[23] O. W. Greenberg. Spin and unitary-spin independence in a paraquark model of baryons and mesons. *Phys. Rev. Lett.*, 13:598–602, Nov 1964.

[24] William A. Bardeen, H. Fritzsch, and Murray Gell-Mann. Light cone current algebra, pi0 decay, and e+ e- annihilation. 1972.

[25] V.V. Ezhela, S.B. Lugovsky, and O.V. Zenin. Hadronic part of the muon g-2 estimated on the sigma**2003(tot)(e+ e- to hadrons) evaluated data compilation. 2003.

[26] Claude Amsler et al. Review of Particle Physics. *Phys.Lett.*, B667:1–1340, 2008.

[27] Particle Data Group. Review of particle physics. *Phys. Rev. D*, 86:010001, Jul 2012.

[28] Jefferson Lab A. W. Thomas. The Spin of the Proton. 2008.

[29] A. Grebenyuk, F. Hautmann, H. Jung, P. Katsas, and A. Knutsson. Jet production and the inelastic pp cross section at the LHC. 2012.

[30] T. Sjostrand and Peter Z. Skands. Multiple interactions and the structure of beam remnants. *JHEP*, 0403:053, 2004.

[31] Francois Gelis, Edmond Iancu, Jamal Jalilian-Marian, and Raju Venugopalan. The Color Glass Condensate. *Ann.Rev.Nucl.Part.Sci.*, 60:463–489, 2010.

[32] David J. Gross and Frank Wilczek. Ultraviolet behavior of non-abelian gauge theories. *Phys. Rev. Lett.*, 30:1343–1346, Jun 1973.

[33] H. David Politzer. Reliable perturbative results for strong interactions? *Phys. Rev. Lett.*, 30:1346–1349, Jun 1973.

[34] N.K. Nielsen and Odense Universitet Fysisk Institut. *Asymptotic freedom as a spin effect*. Fysisk Institut, Odense Universitet, 1980.

[35] David J. Gross. Twenty five years of asymptotic freedom. *Nucl.Phys.Proc.Suppl.*, 74:426–446, 1999.

[36] Edward V. Shuryak. Quantum chromodynamics and the theory of superdense matter. *Physics Reports*, 61(2):71 – 158, 1980.

[37] K. Adcox et al. Formation of dense partonic matter in relativistic nucleus-nucleus collisions at RHIC: Experimental evaluation by the PHENIX collaboration. *Nucl.Phys.*, A757:184–283, 2005.

[38] John Adams et al. Experimental and theoretical challenges in the search for the quark gluon plasma: The STAR Collaboration's critical assessment of the evidence from RHIC collisions. *Nucl.Phys.*, A757:102–183, 2005.

[39] Y. Dokshitzer. *Basics of Perturbative QCD*. Basics of. Editions Frontières, 1991.

[40] Stanley J. Brodsky and Anne Sickles. The baryon anomaly: Evidence for color transparency and direct hadron production at rhic. *Physics Letters B*, 668(2):111 – 115, 2008.

[41] S.S. Adler et al. High p_T charged hadron suppression in Au + Au collisions at $\sqrt{s}_{NN} = 200$ GeV. *Phys.Rev.*, C69:034910, 2004.

[42] S. M. Berman, J. D. Bjorken, and J. B. Kogut. Inclusive processes at high transverse momentum. *Phys. Rev.*, D4:3388–3418, 1971.

[43] J.F. Gunion R.Blankenbecler, S.J. Brodsky. Magnitude of large-transverse-momentum cross sections. *Phys. Rev.*, D18:900, 1978.

[44] J. Kogut R.F. Cahalan, K.A. Geer and L. Susskind. Asymptotic freedom and the absence of vector-gluon exchange in wide-angle hadronic collisions. *Phys. Rev.*, D11:1199, 1975.

[45] CMS Collaboration. Charged particle transverse momentum spectra in *pp* collisions at $\sqrt{s} = 0.9$ and 7 TeV. *JHEP*, 1108:086, 2011.

[46] François Arleo, Stanley J. Brodsky, Dae Sung Hwang, and Anne M. Sickles. Direct hadron production in hadronic collisions. *Nuclear Physics B - Proceedings Supplements*, 207–208(0):81 – 84, 2010.

[47] M. Burkardt S. J. Brodsky and I. Schmidt. Quantum chromodynamic constraints on the shape of polarized quark and gluon distributions. *Nucl. Phys. B441*, page 197, 1995.

[48] A. Bazilevsky. Talk at APS meeting. http://www.phenix.bnl.gov/www/talk/newtalk.php?cid=aps10. 2010.

[49] Jan Fiete Grosse-Oetringhaus. Measurement of the Charged-Particle Multiplicity in Proton-Proton Collisions with the ALICE Detector.

[50] Torbjorn Sjostrand, Stephen Mrenna, and Peter Z. Skands. A Brief Introduction to PYTHIA 8.1. *Comput.Phys.Commun.*, 178:852–867, 2008.

[51] I. Hrivnacova, O. Datskova, A. Gheata, A. Morsch, and E. Sicking. The ALICE Geant4 simulation. *J.Phys.Conf.Ser.*, 331:032016, 2011.

[52] Filip Krizek. private communication.

[53] The ALICE Collaboration. The ALICE Offline Bible.

[54] Simon Mathieu White. Determination of the Absolute Luminosity at the LHC.

[55] Oliver Sim Brüning, Paul Collier, P Lebrun, Stephen Myers, Ranko Ostojic, John Poole, and Paul Proudlock. *LHC Design Report*. CERN, Geneva, 2004.

[56] S. van der Meer. Calibration of the Effective Beam Height in the ISR. 1968.

[57] The ALICE Collaboration. Measurement of inelastic, single- and double-diffraction cross sections in proton–proton collisions at the LHC with ALICE. 2012.

[58] Matteo Cacciari, Gavin P. Salam, and Gregory Soyez. The Anti-k(t) jet clustering algorithm. *JHEP*, 0804:063, 2008.

[59] S.S. Adler et al. Jet properties from dihadron correlations in p^+p collisions at $\sqrt{s}$ = 200-GeV. *Phys.Rev.*, D74:072002, 2006.

[60] Esko Pohjoisaho. FYSZ470 Research Report: PYTHIA Study of Isolation Cuts in x_T Distributions, 2012.

[61] S.S. Adler et al. Jet properties from dihadron correlations in p^+p collisions at $\sqrt{s}$ = 200-GeV. *Phys.Rev.*, D74:072002, 2006.

[62] J.D. Bjorken. Can We Measure Parton Parton Cross-Sections? *Phys.Rev.*, D8:4098, 1973.